

A LABORATORY INVESTIGATION OF MUD SEABED THICKNESS CONTRIBUTING
TO WAVE ATTENUATION

By

DAVID J. ROBILLARD

A DISSERTATION PRESENTED TO THE GRADUATE SCHOOL
OF THE UNIVERSITY OF FLORIDA IN PARTIAL FULFILLMENT
OF THE REQUIREMENTS FOR THE DEGREE OF
DOCTOR OF PHILOSOPHY

UNIVERSITY OF FLORIDA

2009

© 2009 David J. Robillard

To my family

ACKNOWLEDGMENTS

I wish to express my sincere appreciation to my advisor, Dr. Ashish Mehta, for his professional guidance during the course of my studies. Many thanks are also due to the members of my committee, Dr. Robert Dean, Dr. Kurtis Gurley and Dr. Peter Adams. The mentorship and classroom instruction from each committee member significantly enhanced my educational experience at the University of Florida.

Special thanks go to Dr. Gregory Stone and particularly Mr. Bill Gibson for support provided with the collection of copious amounts of seabed mud from the Atchafalaya Delta and for sharing quality historical WAVCIS wave data measurements.

Assistance by faculty throughout the University of Florida is gratefully acknowledged. Particularly, Dr. Willie Harris of the Soil and Water Science Department for the unselfish commitment of his time and use of his laboratory facilities, Dr. Hordur Kristinsson of the Food Science and Human Nutrition Department for opening his lab facility and rheometer for use throughout this study, Dr. John Jaeger of the Geological Sciences Department for his generous assistance and use of his laboratory facilities, and Mr. James Joiner of the Coastal Engineering Laboratory for assistance with revitalizing the wave flume.

Lastly I wish to thank my wife, Carol and children, Mary Ann, Sarah, Daniel, Kelly, John and Patrick. Their support and understanding during my studies is recognized with heartfelt love and gratitude.

TABLE OF CONTENTS

	<u>page</u>
ACKNOWLEDGMENTS.....	4
LIST OF TABLES.....	9
LIST OF FIGURES	10
ABSTRACT	16
CHAPTER	
1 INTRODUCTION.....	18
1.1 Problem Statement	18
1.2 Review of Past Studies	20
1.2.1 Field/Experimental Studies.....	20
1.2.2 Analytical/Numerical Studies	21
1.3 Study Objective and Approach	23
1.4 Study Outline.....	24
2 ATCHAFALAYA DELTA SEDIMENT CHARACTERIZATION.....	26
2.1 Delta Morphology	26
2.2 Atchafalaya River Delta	26
2.2.1 Atchafalaya Delta Seabed Study Site.....	28
2.2.2 Sample Collection	29
2.3 AD Mud Sediment Characterization.....	30
2.3.1 Density of Solids	30
2.3.2 Organic Content.....	31
2.3.3 Grain Size Distribution	32
2.3.3.1 Sand fraction	32
2.3.3.2 Silt/Clay fraction	32
2.3.4 Mineral Composition.....	33
2.3.4.1 Silt / Clay fraction composition	34
2.3.4.2 Clay fraction composition	34
2.3.5 Clay Chemistry and Structure.....	36
2.3.6 Order of Aggregation	38
2.4 AD Mud Seabed Characterization	39
2.4.1 Settling and Self-Weight Consolidation Analysis.....	40
2.4.2 Settling Profile	41
2.4.3 Consolidated Bed Solids Volume Fraction Profile	43

3	ATCHAFAKYA DELTA MUD DYNAMIC BEHAVIOR	57
3.1	Constitutive Models	57
3.2	Material Response to Stress	59
3.2.1	Characterization of Seabed Stresses.....	59
3.2.2	Triaxial Testing.....	61
3.2.3	Shear Rheometry	62
3.3	Rheometer.....	62
3.3.1	Temperature Consideration.....	63
3.3.2	Instrument Geometry.....	63
3.4	Rheometer Testing Artifacts	64
3.4.1	Wall Depletion.....	64
3.4.2	Wall Depletion Reduction.....	65
3.4.3	Secondary Flow	66
3.5	Rheometer Test Protocols.....	68
3.5.1	Continuous Flow (Creep) Test.....	68
3.5.2	Oscillatory Flow Test	69
3.6	Characteristics of Seabed Response	71
3.6.1	Yield Stress	71
3.6.2	Shear Thinning and Thixotropy.....	71
3.7	Rheology Test Results	73
3.7.1	Continuous Flow (Creep) Tests	73
3.7.2	Oscillatory Flow Tests	74
3.7.2.1	Thixotropic response	74
3.7.2.2	Bond density.....	75
3.7.2.3	Oscillatory strain rate response tests.....	77
3.8	Summary of AD Mud Response to Oscillatory Flow.....	77
3.8.1	AD Mud Property Response	77
3.8.2	Influence of Stress History.....	80
4	CONSTITUTIVE MODEL	93
4.1	Introduction	93
4.2	Viscoelastic Equations.....	93
4.3	Thixotropy	95
4.4	AD Mud Flow Response Equation	97
4.4.1	Model Approach.....	97
4.4.2	Model Derivation.....	98
4.4.3	Observations	100
4.4.4	Analysis of Results	101
4.5	AD Mud Dynamics	103
4.5.1	Aggregate Orders.....	103
4.5.2	Aggregate Densities	103
4.5.3	Shear Strength.....	106
5	WAVE DISSIPATION AND SEABED TRANSITION	134

5.1	Model Formulation	134
5.1.1	Governing Equations.....	135
5.1.2	Model Derivation-Water Column.....	136
5.1.3	Model Derivation- Seabed	138
5.2	Model Application	139
5.2.1	Seabed Dynamics	139
5.2.2	Wave Energy Dissipation.....	142
6	ASSESSMENT OF TRANSITIONED THICKNESS AND ENERGY DISSIPATION.....	148
6.1	Wave Flume	148
6.1.1	Equipment and Instrumentation.....	148
6.1.2	Wave Attenuation Characteristics	148
6.1.3	Experimental Setup	149
6.1.4	Test Run Protocol.....	150
6.1.5	Test Run Results.....	152
6.2	Discussion of Model Results for Test Run R2.....	154
6.2.1	Bed Velocity Profile.....	154
6.2.2	Bed Shear Stress Profile.....	154
6.2.3	Bed Viscosity Profile	155
6.2.4	Bed Wave Energy Dissipation Profile	155
6.3	Wave Flume Mud Slope Analysis	156
6.4	Model Application to Field Data	158
6.5	Topset Bed Slope Analysis.....	160
7	SUMMARY AND CONCLUSIONS	174
7.1	Summary.....	174
7.2	Observations.....	175
7.3	Recommendations for Future Studies.....	175
APPENDIX		
A	DETERMINATION OF MUD FLOW CURVE PARAMETERS	177
A.1	Wave and Mud Bed Property Ranges.....	177
A.2	Mild Stress History	177
A.2.1	Viscosity at Infinite Rate of Strain, μ'_{INF}	178
A.2.2	Viscosity in Linear Elasticoviscous (LEV) Region, μ'_{LEV}	178
A.2.3	Sine of the Phase Angle in Linear Elasticoviscous (LEV) Region, $\sin\delta_{\text{LEV}}$..	179
A.2.4	Rate of Strain at Transition, $\gamma_{\text{LIQ}}^{\square}$	179
A.3	Severe Stress History	179
A.3.1	Viscosity at Infinite Rate of Strain, μ'_{INF}	180
A.3.2	Viscosity in Linear Elasticoviscous (LEV) Region, μ'_{LEV}	180

A.3.3 Sine of the Phase Angle in Linear Elasticoviscous (LEV) Region, $\sin\delta_{LEV}$	180
A.3.4 Rate of Strain at Transition, $\dot{\gamma}_{LIQ}$	180
LIST OF REFERENCES	192
BIOGRAPHICAL SKETCH	197

LIST OF TABLES

<u>Table</u>		<u>page</u>
2-1	Tests used to characterize AD Mud properties.	47
2-2	Loss on Ignition test results.	47
2-3	Initial solids volume fraction of cylinder sediment, Figure 2-11.	47
3-1	Test protocol for continuous time series runs.....	81
3-2	Bond density estimates for AD Mud aggregates.....	81
3-3	Strain rate sweep test parameters.	82
4-1	AD Mud properties – oscillatory test results of flow curve variables [Forward Shear Rate Sweeps (simulating “pre-storm” condition)].	109
4-2	AD Mud properties – oscillatory test results of flow curve variables [Reverse Shear Rate Sweeps (simulating “post-storm” condition)].	110
4-3	Comparison of results – density of AD Mud aggregates.....	111
4-4	Eq. 4-19 Coefficients for AD Mud.	111
6-1	Wave flume test run parameters.	162
6-2	Comparison of wave energy dissipation rates based on recent stress history.	162
6-3	Comparison of measured and model wave energy flux dissipation results.....	162
6-4	Hurricane Lili wave condition.....	162

LIST OF FIGURES

<u>Figure</u>		<u>page</u>
1-1	Definitional sketch of wave energy flux dissipation and mud seabed transition.....	25
2-1	Atchafalaya and Mississippi River deltas.....	48
2-2	Sediment accumulation rates along the Atchafalaya subaqueous delta as determined by ^{210}Pb analysis.....	48
2-3	Site of seabed sampling coincident with WAVCIS CSI3 monitoring station.....	49
2-4	Clinoform bed profile seaward of CSI3 site.....	49
2-5	Wet sieve and Sedigraph results – AD Mud.	50
2-6	Mississippi River drainage basin indicating dominant mineral group distribution of tested soil samples.....	50
2-7	Sand/silt/clay fractions of the top 20cm of seabed along the outer topset and foreset regions of the Atchafalaya delta clinoform.	51
2-8	XRD result for combined AD Mud silt/clay fraction.	52
2-9	XRD result for isolated AD Mud clay fraction.	52
2-10	Diagrammatic representation of order of aggregate concept used to define the structure of mud.	53
2-11	250 ml graduated cylinders used as settling columns to measure settling and consolidation characteristics of six discrete solids volume concentration samples of AD Mud.	54
2-12	Self-weight settling and consolidation results for AD Mud.	54
2-13	Representation of equivalent solids volume fraction layers of AD Mud thickness superimposed sequentially on cylinder sample images.	55
2-14	AD Mud local solids volume fraction profiles with depth for Days 2, 3, 36 and 56....	55
2-15	Vertical density profiles of mud from Scheldt River, Belgium.	56
3-1	Definition diagram for shear flow.....	83
3-2	Mechanical analog for Voigt model and Maxwell model.	83
3-3	Particle motion related to orientation of external force.	84

3-4	Mohr's circle representation of body stresses.....	84
3-5	Diagram of triaxial test conditions.....	85
3-6	TA Instruments AR 2000ex controlled stress/controlled strain rheometer.....	85
3-7	Cone and plate geometries and vane concentric cylinder geometry.....	85
3-8	Effect of wall depletion on a complex liquid.	86
3-9	Strain responses during creep test.	86
3-10	Intercept with straight line law for defining yield stress.	87
3-11	Material response to stress.....	87
3-12	Creep curve for AD Mud: applied shear stress = 0.5 Pa.	88
3-13	Continuous time series results depicting AD Mud response to Run 1 oscillatory shear stress protocol shown in Table 3-1.....	88
3-14	Continuous time series results depicting AD Mud response to Run 2 oscillatory shear stress protocol shown in Table 3-1.....	89
3-15	Flow response of AD Mud to Run 1F oscillatory strain sweep protocol shown in Table 3-2.....	89
3-16	Flow response of AD Mud to Run 8F oscillatory strain sweep protocol shown in Table 3-2.....	90
3-17	Flow response of AD Mud to Run 15F oscillatory strain sweep protocol shown in Table 3-2.....	90
3-18	Flow response of AD Mud to Run 1B oscillatory strain sweep protocol shown in Table 3-2.....	91
3-19	Flow response of AD Mud to Run 8B oscillatory strain sweep protocol shown in Table 3-2.....	91
3-20	Flow response of AD Mud to Run 15B oscillatory strain sweep protocol shown in Table 3-2.....	92
3-21	General flow response of AD Mud.	92
4-1	Flow curves represented by models.	112
4-2	Hysteresis effect.	112

4-3	Continuous ramp up rate of strain followed by continuous ramp down rate of strain under Run 1F/Run 1B test conditions.....	113
4-4	Continuous ramp up rate of strain followed by continuous ramp down rate of strain under Run 3F/Run 3B test conditions.....	113
4-5	Continuous ramp up rate of strain followed by continuous ramp down rate of strain under Run 5F/Run 5B test conditions.....	114
4-6	Continuous ramp up rate of strain followed by continuous ramp down rate of strain under Run 8F/Run 8B test conditions.....	114
4-7	Continuous ramp up rate of strain followed by continuous ramp down rate of strain under Run 11F/Run 11B test conditions.....	115
4-8	Continuous ramp up rate of strain followed by continuous ramp down rate of strain under Run 13F/Run 13B test conditions.....	115
4-9	Continuous ramp up rate of strain followed by continuous ramp down rate of strain under Run 15F/Run 15B test conditions.....	116
4-10	Generalized flow response of AD Mud in terms of μ^* and phase angle, $\sin \delta$	116
4-11	Generalized logistic function form and complementary logistic function form.	117
4-12	Measured oscillatory strain sweep results compared to flow curve results – Run 1F.	117
4-13	Measured oscillatory strain sweep results compared to flow curve results – Run 3F.	118
4-14	Measured oscillatory strain sweep results compared to flow curve results – Run 5F.	118
4-15	Measured oscillatory strain sweep results compared to flow curve results – Run 8F.	119
4-16	Measured oscillatory strain sweep results compared to flow curve results – Run 11F... .	119
4-17	Measured oscillatory strain sweep results compared to flow curve results – Run 13F... .	120
4-18	Measured oscillatory strain sweep results compared to flow curve results – Run 15F... .	120
4-19	Measured oscillatory strain sweep results compared to flow curve results – Run 1B....	121
4-20	Measured oscillatory strain sweep results compared to flow curve results – Run 3B....	121
4-21	Measured oscillatory strain sweep results compared to flow curve results – Run 5B....	122
4-22	Measured oscillatory strain sweep results compared to flow curve results – Run 8B....	122
4-23	Measured oscillatory strain sweep results compared to flow curve results – Run 11B... .	123

4-24	Measured oscillatory strain sweep results compared to flow curve results – Run 13B...123
4-25	Measured oscillatory strain sweep results compared to flow curve results – Run 15B...124
4-26	Measured shear stress verses rate of strain along with flow curve results – Run 1F.....124
4-27	Measured shear stress verses rate of strain along with flow curve results – Run 3F.....125
4-28	Measured shear stress verses rate of strain along with flow curve results – Run 5F.....125
4-29	Measured shear stress verses rate of strain along with flow curve results – Run 8F.....126
4-30	Measured shear stress verses rate of strain along with flow curve results – Run 11F....126
4-31	Measured shear stress verses rate of strain along with flow curve results – Run 13F....127
4-32	Measured shear stress verses rate of strain along with flow curve results – Run 15F....127
4-33	Measured shear stress verses rate of strain along with flow curve results – Run 1B.128
4-34	Measured shear stress verses rate of strain along with flow curve results – Run 3B.128
4-35	Measured shear stress verses rate of strain along with flow curve results – Run 5B.129
4-36	Measured shear stress verses rate of strain along with flow curve results – Run 8B.129
4-37	Measured shear stress verses rate of strain along with flow curve results – Run 11B. ...130
4-38	Measured shear stress verses rate of strain along with flow curve results – Run 13B. ...130
4-39	Measured shear stress verses rate of strain along with flow curve equations – Run 15B.....131
4-40	Normalized viscosity of AD Mud versus solids volume fraction from Table 4.2 data...131
4-41	AD Mud shear strength verses solids volume fraction starting at low shear stress and ending at high shear stress.....132
4-42	AD Mud shear strength verses angular frequency of oscillatory flow starting at high shear stress and ending at low shear stress.....132
4-43	AD Mud shear strength verses solids volume fraction.....133
4-44	Sketch of AD Mud state influenced by strain rate and solids volume fraction.....133
5-1	Schematic of boundary value problem.146
5-2	Schematic of transitioned layer thickness, h_d147

6-1	Schematic of wave flume wave maker and mud trench.	163
6-2	Photograph of wave flume and instrumentation at the Coastal Engineering Laboratory, University of Florida.	163
6-3	Continuous wave flume time series of water surface elevation.	164
6-4	Surface elevation data from Test Run R2.....	165
6-5	Spectral density function for Test Run R2.	166
6-6	Horizontal velocity profile as a function of bed depth for Test Run R2.	167
6-7	Shear stress profile as a function of bed depth for Test Run R2. Transitioned depth, h_d , determination.	167
6-8	Real viscosity profile as a function of bed depth for Test Run R2.	168
6-9	Total viscosity profile as a function of bed depth for Test Run R2.	168
6-10	Wave energy flux dissipation profile as a function of bed depth for Test Run R2.....	169
6-11	Settled bed elevation in trench measured after two similar test runs.....	169
6-12	Definitional sketch of gravity-driven flow due to oscillatory flow.....	170
6-13	Probability density function of wave condition at WAVCIS CSI3 during Hurricane Lili at 10/3/2002, 1200.....	170
6-14	Horizontal velocity profile as a function of bed depth for Hurricane Lili 10/3/2002, 1200 wave conditions at WAVCIS CSI3.	171
6-15	Shear stress profile as a function of bed depth and transitioned depth, h_d , for Hurricane Lili 10/3/2002, 1200 wave conditions measured at WAVCIS CSI3.....	171
6-16	Real viscosity profile as a function of bed depth for Hurricane Lili 10/3/2002, 1200 wave conditions at WAVCIS CSI3.....	172
6-17	Total viscosity as a function of bed depth for Hurricane Lili 10/3/2002, 1200 wave conditions at WAVCIS CSI3.....	172
6-18	Wave energy dissipation as a function of bed depth for Hurricane Lili 10/3/2002, 1200 wave conditions at WAVCIS CSI3.	173
6-19	Cliniform bed profile seaward of CSI3 site shown in Figure 2.4 with slope of escarpment face defined.....	173
A-1	Real viscosity at infinite rate of strain versus solids volume fraction.	182

A-2	Real viscosity at infinite rate of strain versus angular frequency of oscillatory flow.....	182
A-3	Contour plot of $\ln(\mu'_{\text{INF}})$ as a function of solids volume fraction and angular frequency.	183
A-4	Real viscosity in the linear elasticoviscous region versus solids volume fraction for mild stress history.	184
A-5	Real viscosity in the linear elasticoviscous region versus angular frequency for mild stress history.	184
A-6	Contour plot of $\ln(\mu_{\text{LEV}})$ for mild pre-stress condition as a function of ϕ_{vs} and ω	185
A-7	Sine of phase angle in linear elasticoviscous region versus solids volume fraction for mild stress history.	185
A-8	Sine of phase angle in linear elasticoviscous region versus solids angular frequency for mild stress history.....	186
A-9	Rate of strain at transition versus solids volume fraction for mild stress history.	186
A-10	Rate of strain at transition versus angular frequency for mild stress history.	187
A-11	Real viscosity in the linear elasticoviscous region versus solids volume fraction for AD Mud for severe stress history.....	187
A-12	Real viscosity in the linear elasticoviscous region versus angular frequency for AD Mud for severe stress history.....	188
A-13	Contour plot of $\ln(\mu_{\text{LEV}})$ as a function of solids volume fraction and angular frequency for severe stress history.....	188
A-14	Sine of phase angle in linear elasticoviscous region versus solids volume fraction for severe stress history.	189
A-15	Sine of phase angle in linear elasticoviscous region versus angular frequency for severe stress history.	189
A-16	Rate of strain at transition versus solids volume fraction for severe stress history.	190
A-17	Rate of strain at transition versus angular frequency of oscillatory flow for severe stress history.	190
A-18	Contour plot of $\ln(\gamma_{\text{LIQ}}^{\square})$ as a function of solids volume fraction and angular frequency for severe stress history.....	191

Abstract of Dissertation Presented to the Graduate School
of the University of Florida in Partial Fulfillment of the
Requirements for the Degree of Doctor of Philosophy

**A LABORATORY INVESTIGATION OF MUD SEABED THICKNESS CONTRIBUTING
TO WAVE ATTENUATION**

By

David J. Robillard

August 2009

Chair: Ashish Mehta

Major: Coastal and Oceanographic Engineering

An important mud seabed parameter in hydrodynamic models of wave-mud interaction is the thickness of the oscillating fluid mud layer in which most wave energy is dissipated. Despite its significance, modelers conventionally define this thickness empirically by tuning the model to the value which produces the measured wave attenuation, thus limiting the model's predictive ability.

To address this issue, a laboratory study has been conducted on seabed sediment from the outer topset of the Atchafalaya River Delta in the Gulf of Mexico in order to develop a method to estimate the thickness of the oscillating fluid mud layer. This development relies on a rheological analysis of mud response to oscillatory shear stress representative of surface wave forcing.

Relevant properties of the mud, including its settling and self-weight consolidation characteristics, are determined from laboratory tests. The mud is further tested using a controlled-stress/controlled-strain rheometer and a flow equation is derived based on the measurements. The flow equation is then used to develop a set of model equations for determination of profiles within the mud of the horizontal velocity, the rate of strain, the bed shear stress and the viscous layer thickness, as well as the total wave energy dissipation rate.

The model equations are validated with extensive flume tests involving the damping of monochromatic water waves over carefully prepared depositional mud beds.

At high shear stresses, the viscosity is found to vary by more than two orders of magnitude and the bed is found to behave simultaneously as an elasticoviscous, viscoelastic or elastic material depending on the depth within the bed. To what thickness the bed will be dominantly viscous depends primarily on the density of the bed and to a lesser degree on the wave characteristics. Under depositional conditions, the density of the upper layer of mud is found to be about 1,200 kg/m³. At this density, the mud readily transitions to a viscous state under even weak oscillatory shear stress. However, as the bed density increases with depth, mud shear strength increases nonlinearly and higher shear stresses are required to achieve this transition.

Due to the thixotropic property of this mud, the stress history plays a key role in how the mud responds to shear stress. The thickness of the dominantly viscous mud layer is greater when the preceding shear stress condition on the mud bed is higher than the imposed stress, in contrast with the case when the preceding stress is lower than the imposed stress.

A procedure has been developed to estimate the thickness of the dominantly viscous mud layer given water depth, wave properties and the mud rheological flow curve. Flume data are shown to be in good agreement with the results derived from this procedure, which also appears to show promise in field applications. Further investigations are required to examine effects of normal stress in mud, non-Gaussian wave fields and mud mass transport within the thickness of the viscous layer.

CHAPTER 1 INTRODUCTION

*“Big flocs are made of little flocs,
All contributing to bulk density,
And little flocs are made of lesser flocs,
And so on to particle primacy.”*

1.1 Problem Statement

Fine-grained, saturated, cohesive sediment, often referred to as mud, is a common seabed material found in fluvial-dominated deltas, estuarine environments and in shallow lakes and reservoirs. Sigmoidal-shaped subaqueous deltaic mud deposits (clinoforms) typically mark the entrance to large river systems which serve as conduits to major shipping ports around the world and are also favorable locations for the installation of oil exploration platforms and submarine pipelines. Environmentally, areas in the vicinity of deltaic clinoforms are often sites of important aquatic ecosystems and fragile food chains that support the needs of large human populations. The cohesive and reactive nature of the clay-sized particles that define the mud also serve to bind with contaminants [Lytle and Lytle, 1983].

The cohesive continuum structure of a muddy seabed allows wave momentum to propagate more readily down into the seabed with the result that energy dissipation occurs over a bed layer whose thickness depends on wave and bed properties. The ability to assess the effect waves have on the mud bed necessitates an understanding of the dynamic response of mud under oscillatory wave motions. Figure 1-1 is a definition sketch of the physical problem. As water waves propagate over the seabed in finite water depth, shear stress due to water particle motion is transferred down into the seabed causing oscillatory motion within the bed. The mud rheology, which is influenced by wave amplitude, frequency and water depth, determines the nature of the bed motion, the rate at which energy is dissipated from the wave field and to what depth the bed becomes predominantly viscous. Since mud that is not predominantly viscous

absorbs surface wave energy at a low, often negligible, rate, knowledge of the thickness of the wave-induced, predominantly viscous layer (transitioned layer) is critically important because it is the layer where most of the dissipation of energy associated with the damping of the surface wave takes place.

Analytical and numerical models since the pioneering work of *Gade* [1958] have assumed a thickness of the predominantly viscous layer by empirically tuning the value so that it is consistent with the rate of energy dissipation derived from measured wave damping coupled with one or more rheological models that describe mud response to applied stress. Since the association between mud rheology and the thickness of the predominantly viscous layer is not well known, the choice of the rheological model is often made arbitrarily. In order to reduce this empiricism it is essential that a physical basis be developed that permits the determination of the predominantly viscous layer thickness from a rheological model that is consistent with the response of the actual mud to water waves and their attenuation with distance.

To investigate complex wave-mud interactions requires detailed measurements of the dynamic processes occurring in the seabed as well as at the free surface and in the water column. Data collection in the field, particularly during storm events, is logistically challenging and costly. The ability to measure in-situ the wave induced dynamics within the seabed has not yet been fully demonstrated. As a result, a rheology-based experimental approach under laboratory conditions has been used in this study. This approach enables the processes within the bed and in the water column to be evaluated while minimizing nuisance variables and controlling the independent variables which would not be possible in a field investigation.

1.2 Review of Past Studies

1.2.1 Field/Experimental Studies

Researchers throughout the world have collected field data to study the influence of a muddy seabed on water wave attenuation. One of the first field campaigns in the United States to measure wave attenuation over a muddy seabed was conducted in East Bay, Louisiana in the early 1970's. The energy loss rate measured during this study was reported to be two orders of magnitude greater than that predicted for a sand seabed [*Tubman and Suhayda, 1976*]. In another study conducted off the coast of Surinam, measurements of spectral wave energy reflected a 96% loss of wave energy over a distance of 18 km [*Wells and Kemp, 1986*]. Significantly increased wave damping was shown to take place during the presence of episodically occurring mud banks off the coast of Kerala, India compared to the wave damping observed when the mud banks were absent [*Mathew et al., 1995*].

Catastrophic consequences have been attributed to the transfer of energy from storm waves to the muddy seabed which caused the upper bed layer to transition to a predominantly viscous liquid and subsequent slope failure. In 1969, Hurricane Camille wave conditions produced a submarine mudslide which destroyed Shell Oil Company's 'B' Platform in the vicinity of the Mississippi River Delta in the Gulf of Mexico [*Sterling and Strohbeck, 1973*]. Researchers have attributed the initiation of many such mudslides induced by bed transition to wave forcing influence [*Morgenstern, 1967, Traykovski et al., 2000, Wright et al., 2001*]. Both sinking and floating of submarine pipelines, depending on the buoyancy of the pipeline, have been shown to result due to transition failure of the seabed material caused by wave activity [*Sumer et al., 1999*].

1.2.2 Analytical/Numerical Studies

Several researchers have taken theoretical approaches to quantify the interaction of waves and a muddy seabed. Formulations have been proposed that analytically or numerically model seabed-wave interaction. Each formulation defines specific seabed property assumptions and boundary conditions. Gade [1958] represented the wave-mud system as a two-layer model with the water column represented as an inviscid liquid and the sediment bed represented as a viscous liquid. The model is predicated on shallow water conditions [i.e. $kh < \pi/10$ where $k=2\pi/\lambda$ (m^{-1}) is the wave number, λ is the water wave wavelength, and h is the water depth (m)], and assumes that the viscous boundary layer responsible for wave energy flux dissipation only exists in the sediment bed. This model has been used as a basis for many other models which is a testament to its seminal elegance and effectiveness.

Darlymple and Liu [1978], *Lowes* [1993] and *Ng* [2000] all introduced first-order models derived from Gade's model. Darlymple and Liu represented the wave-mud system as two viscous liquids of different densities and assumed the mud bed was much deeper than the Stokes' boundary layer thickness defined as $\delta = \sqrt{\frac{2v_b}{\omega}}$ where v_b is the kinematic viscosity of the bed sediment (m^2/s) and ω is the water wave angular velocity (rad/s). They also extended Gade's model results to include intermediate water depth ($kh < \pi$) cases. Ng defined the problem in a similar way but with the mud bed of a finite depth much thinner than the overlying water layer and on the order of the Stokes boundary layer thickness. Lowe presented the Full Scale Model (FSM) which resolved the limitations of the mud bed thickness in relation to the boundary layer thickness imposed by the other two described models.

Mallard and Dalrymple [1977], *Dawson* [1980] and *Foda* [1989] all introduced models that defined the mud seabed as an elastic material. These models described bed motion but attenuation of wave amplitude could not be accounted for due to the lack of viscous properties in the seabed.

MacPherson [1980], *Hsiao and Shemdin* [1980] and *Maa and Mehta* [1988] treated the mud seabed as a viscoelastic Voigt material. The model by MacPherson required the mud to have either seemingly unrealistically large viscous or elastic properties shown by Eq. 1-1.

$$\left(\frac{k^2 v_b}{\omega} \right) \gg 1, \text{ or } \left(\frac{k^2 G}{\omega^2 \rho_m} \right) \gg 1 \quad (1-1)$$

with G =elastic shear modulus (Pa), ρ_m =density of mud (kg/m^3).

Yamamoto and Takahashi [1985] considered Coulomb friction of granular material as the primary mechanism of wave energy dissipation within the seabed. This model assumes a two-phase bed with individual grains as the solid phase and pore water as the fluid phase defining the bed.

Jain and Mehta [2009] used a second order analytical approach improving on the work of Lowes [1993] to model wave attenuation by mud and water mass transport. Domains of applicability for viscous, viscoelastic and poroelastic models of mud were proposed and it was reaffirmed that fluid mud should be considered as a viscoelastic or viscous fluid and only non-predominantly elastic mud should be represented as a viscoelastic solid or poroelastic material.

Essential to all wave-mud seabed interaction models is an accurate definition of the rheological properties of the mud which characterize the motion of the seabed in response to external forces. A thorough understanding of the seabed sediment and its properties along with an understanding of the wave properties is crucial for the establishment of the appropriate boundary value problem.

Although all the referenced studies require bed properties such as density, ρ , and kinematic viscosity, v , to be defined as independent variables of the solution, many models do not address the rheological underpinnings for the bottom boundary assumptions regarding the seabed. These variables are often treated as generalized constants of the bed material independent of the imposed stress rather than as state variables. Such treatment appears somewhat presumptuous considering that, by definition the values of these variables are dependent on the motion of the bed material. *Chou et al.* [1993] and *Foda et al.* [1993] recognized the significance of including rheological properties of the mud seabed into a wave- mud seabed interaction model.

1.3 Study Objective and Approach

The specific objective of this study is to develop a method to determine the thickness of predominantly viscous mud seabed that participates in wave field attenuation as a function of wave and mud properties and interaction dynamics. To accomplish this objective, a rheological approach will be used to analyze the stress–rate of strain response of seabed sediment (AD Mud) collected from the outer topset region of the Atchafalaya River Delta (bordering the Gulf of Mexico) to oscillatory wave motion. It is proposed to demonstrate that the flow response of this mud should properly be considered in terms of state variables dependent on the characteristics of the wave forcing. To that end a non-linear flow curve defined completely in terms of variables representing the rheological properties of the mud is introduced and used to characterize the dynamic bottom boundary condition in the mud seabed.

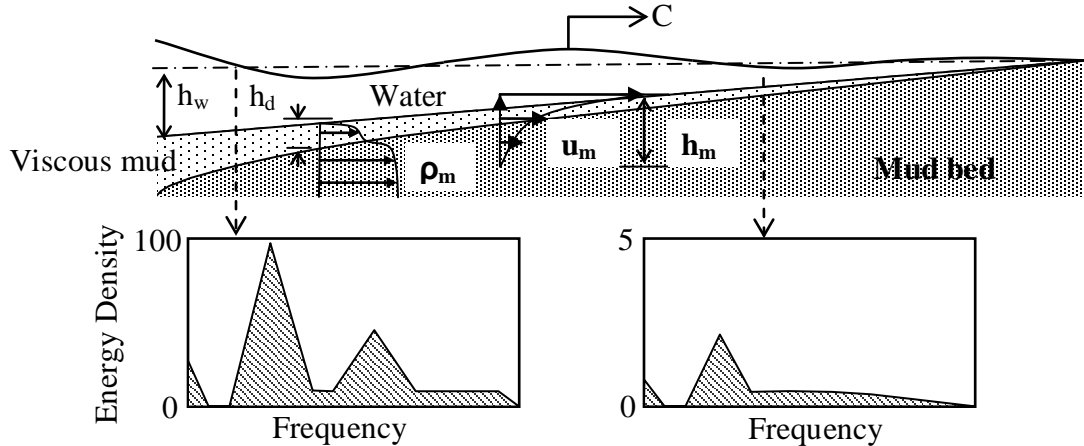
The dynamic bottom boundary condition used to determine the thickness of mud participating in the attenuation of wave energy and the wave energy dissipation rate is intrinsically defined based on rheological properties of the seabed. In this way, generalizations or assumptions about the material and flow properties of the seabed are avoided. However,

before rheological analysis of the mud seabed material can be carried out, it is important to appreciate the origin, composition and characteristics of the mud and the seabed.

1.4 Study Outline

The methodology used to achieve this objective is reflected in the layout of the chapters and described as follows:

A thorough analysis and classification of AD Mud is presented in Chapter 2. This chapter defines the domain of applicability of the study as well as outlines a methodology for the study of mud from other geographic locations. In Chapter 3 the rheology-based approach is discussed and data from oscillatory shear rheometer tests of AD Mud are presented. The results obtained in Chapter 3 are analyzed in Chapter 4 and a flow curve is derived reflecting the AD Mud rheological rate of strain response generated by an externally imposed oscillatory shear stress. Chapter 5 presents the governing partial differential equation and boundary condition assumptions used to define the model relating the wave induced shear stress at the water column/AD Mud bed interface to the resulting rate of strain response within the bed. Analytical solutions, which resolve the transitioned depth, dynamic properties of the bed and the wave energy dissipation rate for a defined initial wave forcing, are presented. In Chapter 6 model results are evaluated against data collected during a series of wave flume runs performed for the purpose of validating the model results. Chapter 7 summarizes the findings of this study and presents observations pertaining to the wave/mud seabed interaction dynamics of AD Mud. Future study recommendations are offered to advance the understanding of this complex problem. Appendix A provides a resource to enable solution of the boundary value problem under a broad range of possible field and laboratory conditions for studying related problems in this region of the Gulf of Mexico.



h_w =water depth

h_d =dominantly viscous mud (fluid mud) thickness

ρ_m =density of mud seabed

u_m =magnitude of horizontal bed velocity

C =wave celerity

h_m =depth of non-zero horizontal oscillatory bed motion

Figure 1-1. Definitional sketch of wave energy flux dissipation and mud seabed transition from a dominantly elastic to a dominantly viscous material state.

CHAPTER 2

ATCHAFALAYA DELTA SEDIMENT CHARACTERIZATION

2.1 Delta Morphology

Rivers are the primary conduit for transport of terrigenous sediment to the coastal oceans [Milliman and Meade, 1983]. This sediment typically accumulates in a deltaic system consisting of a sub-aerial formation and a sub-aqueous clinoform seaward of the river mouth. The morphology of the deltaic system depends significantly on the local fluvial, tidal and wave regimes [Wright and Coleman, 1973]. The subaqueous clinoform extends from the sub-aerial features and is characterized by a relatively flat topset followed seaward by a slightly steeper foreset. The steepness of the exposed shelf slope will determine if a mild sloping bottomset exists at the distal end of the foreset or if the clinoform terminates at the foreset. Sediment discharge from the river system, hydraulic forcing mechanisms and coastal shelf bathymetry determine the development and geometry of the clinoform [Liu *et al.*, 2004]. The sub-aqueous clinoform of the Atchafalaya River deltaic system is the result of the latest Holocene diversion of the Mississippi River.

2.2 Atchafalaya River Delta

Since 1542, the Atchafalaya River in Louisiana has been a distributary of the Mississippi River [Fisk, 1952] (Figure 2-1). Prior to 1839, the discharges were small but a dredging project during that year made the Atchafalaya River a more favorable discharge path for the Mississippi River drainage basin. This basin is the third largest in the world draining an area of 3.3×10^6 km² and carrying a sediment load of approximately 2.1×10^8 tons/a [Meade *et al.*, 1990]. In 1963, a control structure was installed to regulate the Mississippi River discharge into the Atchafalaya River at a combined 30% of flow from the Mississippi and Red Rivers.

The Mississippi River has been the primary basin discharge conduit for the past 600-800 years and its substantial progradation has decreased the hydraulic gradient of the deltaic system resulting in reduced flow efficiency. As evidenced by Figure 2-1, the topset of the Mississippi River subaqueous clinoform has prograded out to the shelf break and, as a result, sediment discharged at this site now is carried down the very steep continental slope and lost to the active littoral zone.

The Atchafalaya River discharge point is 307 km closer than the Mississippi River discharge point and as a result provides a hydraulically more efficient gradient for discharge of the basin [Van Heerden *et al.*, 1988]. Accretion has reduced accommodation space for sediment in the delta plain and topset regions so sediment discharged from the river is transported seaward to the outer topset and foreset of the clinoform making this area of the delta the highest depositional environment (Figure 2-2).

As at most river-ocean deltaic systems, the Atchafalaya River discharge is characterized as hypopycnal and the sorting sequence of suspended sediment extends a long distance from the river mouth. Most of the sand and coarser silt fractions are deposited in crevasse splays along the delta channels, just beyond the mouth of the river on the delta plain and on the proximal delta front forming a mouth bar. These are also the main fractions forming the coarse-grained sub-aerial delta lobes at the mouth of the Atchafalaya River and out into the Atchafalaya Bay. The finer clay fraction, which remains suspended across the delta front, is deposited in the calmer prodelta region where the river processes diminish and the basinal processes dominate. Subaqueous prodelta deposits of mud have built out onto the Atchafalaya inner shelf and are accreting at approximately 3.8 cm/a [Neill and Allison, 2005] (Figure 2-2). Due to the mild slope of the clinoform in this vicinity and prevailing westward flow of alongshore currents, the

coastline of the Chenier Plain area of Louisiana to the west has experienced significant seaward progradation of up to 29 m/a [Kineke *et al.*, 2006].

2.2.1 Atchafalaya Delta Seabed Study Site

The study area selected for collection of seabed samples (CSI3) is located at the outer part of the topset of the Atchafalaya River delta system directly offshore of Marsh Island and leeward of Trinity Shoal along the 5 m isobath at 92°03.68' W, 29°26.47' N (Figure 2-3). Figure 2-4 depicts the bathymetry of CSI3 and the seaward approach obtained from NOAA-GEODAS hydrographic survey data managed at the National Geophysical Data Center (NGDC) [NOAA, June 2008]. In reference to Figure 2-4, CSI3 is situated on the topset approximately 20 km from the start of the foreset which is identified by a distinct change in the bottom slope. The average topset slope in this area of the Atchafalaya Delta is 0.0001. This is a very mild slope indicating a fluvial dominated, high-deposition environment over a wide continental shelf. The foreset slope of the approach to the site is 0.00027, which is almost three times steeper than the average topset slope. The topography of the foreset clinoform is relatively homogeneous and flat and appears to end at the 9 m isobath at this longitude on to the steeper shelf slope. This is consistent with the findings reported by Neill and Allison [2005], based on seismic transects profiling the delta bed strata which indicated that the modern mud delta terminates prior to reaching the 10 m isobath in this vicinity of the delta and at that point seaward, the bed consists of relic mud from earlier Holocene Mississippi deltaic lobe deposits.

The site selected for collection of the mud samples coincides with the Wave Current Information System (WAVCIS) CSI3 monitoring station. WAVCIS is operated and maintained by the Coastal Studies Institute (CSI) at Louisiana State University. The objective of WAVCIS is to provide wave information (sea state) including wave height, period, direction of propagation, water level, surge, near-surface current speed and direction and meteorological

conditions on a real time basis around the entire Louisiana coast [WAVCIS, October, 2007]. Near-continuous data of ocean conditions have been collected by CSI3 since October, 2000. Specifically, meteorological parameters, including wind speed and direction, barometric pressure, air temperature, and water temperature are sampled at 1 Hz for a 10-min interval beginning 10 minutes before the top of every hour. Hydrodynamic parameters, including water depth and current velocity, are sampled at 2 Hz for approximately 17 minute at the beginning of every hour.

The outer topset location of the delta was selected since it is the most active section of the Atchafalaya River delta. As the topset continues to accrete seaward, the foreset will migrate seaward as well and will always be exposed to the most significant shoaling wave energy. Understanding the response of this location to wave activity is critical in order to appreciate how the deltaic system protects the coast and how high energy transient wave conditions influence its morphology.

2.2.2 Sample Collection

On 20 June 2008, approximately 300 gallons of seabed sediment (AD Mud) were collected from offshore of the CSI3 site (Figure 2-3) using a clamshell bottom sampler. The bottom sampler collected bulk samples representative of the top 75 cm of seabed. The samples were observed to be uniform in consistency and color, did not contain any noticeable organic or inorganic debris, and had the consistency of a watery paste and the texture of clay. They were transported to the University of Florida's Coastal and Oceanographic Engineering Laboratory for analysis and maintained in a saturated condition.

The description of the sediment is what would be expected for mud from a highly depositional environment located approximately 60 km from the mouth of the river delivering the sediment. At that location, only the fine grained sediment fraction has the ability to remain

in suspension under the milder current conditions. The relationship between grain size, d (m), and settling velocity, w_s (m/s), is provided by Stokes Law (equation 2-1).

$$w_s = \frac{gd^2(\rho_s - \rho_w)}{18\mu} \quad (2-1)$$

g =gravitational acceleration, 9.81 m/s², ρ_s =density of the sediment (kg/m³), ρ_w =density of seawater (kg/m³), and μ =viscosity of seawater (Pa-s).

2.3 AD Mud Sediment Characterization

An assessment of AD Mud composition and characterization establishes a basis for analysis of how the bed responds to water waves. General sediment characterization will be determined based on the tests listed in Table 2-1.

2.3.1 Density of Solids

AD Mud is a complex mixture of mineral particles and pore water filling the interstitial voids of the solids. For determination of density of solids, aliquots of AD Mud were drawn and dried in an oven under low temperature (50°C) until all moisture was removed from the samples. The resulting solids were then mechanically pulverized into a powder form, weighed and placed into a 250 ml Erlenmeyer flask. Water was added to bring the total volume of the mixture to 250 ml, and the mixture was gently agitated to release any trapped air from the voids of the powdered solids. Density of solids, ρ_s , was determined as follows:

$$m_w = m_{\text{total}} - m_s \quad (2-2)$$

$$V_w = \frac{m_w}{\rho_w} \quad (2-3)$$

$$V_s = V_{\text{total}} (\text{i.e. } 250 \text{ ml}) - V_w \quad (2-4)$$

$$\rho_s = \frac{m_s}{V_s} \quad (2-5)$$

m=mass (kg), V=volume (m^3), with subscripts w=water, s=solids and total = combined mixture of water and solids. The density of solids for the AD Mud sampled was measured as $\rho_s=2,580$ kg/ m^3 . This important value will be used throughout this study.

2.3.2 Organic Content

Loss on Ignition (LOI) tests were performed on approximately 1 g powdered samples dried in an oven under low temperature heat ($50^\circ C$) to remove moisture. The ASTM D7348 LOI procedure was followed to determine the mass loss from solid combustion residues upon heating in air to $550^\circ C$. Mass loss can be due to residual moisture, carbon and/or sulfur compounds. Since moisture content of the tested sample was minimized during pre-test sample preparation, most of the lost mass from this process was attributed to carbon and/or sulfur compounds which can be used as a measure of the organic activity and detritus in the AD Mud at the sample site. The average loss on ignition percentage was 6.7% of the total mass indicating that the mud at this location had low organic content (Table 2-2).

Due to high sediment accumulation rates of approximately 2 cm/a measured at the sampling location (Figure 2-2), it would be a hostile environment for any type of organism dwelling in the seabed so it is understandable that the sampled sediment did not show any visual evidence of bioturbation or the presence of ichnocoenoses. *Neill and Allison* [2005] analyzed core samples in locations throughout the Atchafalaya Delta and described the facies using X-radiograph techniques. They report that the facies for the near-surface part of the core (top 1 m) taken in proximity to the sample site of this study is described as laminated mud with no noticeable burrowing or bioturbation effects. These observations are in agreement with the LOI findings of the present study.

Although possibly not a relevant factor at this site, bioturbation can significantly alter the structure of the seabed and impact the way it responds to water wave activity. For this reason, initial analysis of the seabed should always include consideration for this possible influence.

2.3.3 Grain Size Distribution

2.3.3.1 Sand fraction

Grain size analysis was conducted using a combination of wet sieving and Sedigraph techniques. Approximately 5 g of AD Mud was disaggregated by dilution with a solution of sodium phosphate and deionized water. The treated mud was placed in an ultrasonic bath to further assist in the breakdown of any floc structures and then was wet sieved using deionized water through a 63 μm (4ϕ) sieve to separate out the sand fraction. This sand fraction was dried under low heat (50°C) and the weight of the fraction was recorded. The remaining sample was also dried and weighed to determine the sand fraction as a percent of the total solids.

2.3.3.2 Silt/Clay fraction

In order to obtain the silt and clay fractions of the mud samples, analysis was done using the Micrometrics SediGraph III 5120. The SediGraph uses a paralleled X-ray beam to detect changes in suspended sediment concentration during quiescent settling along the vertical extent of the settling suspension at specific time intervals. The disaggregation process separates the mud into its particle constituents and the sample is prepared at a low enough concentration to minimize the occurrence of hindered settling.

This method relies on knowledge of the particle and liquid densities as well as the dynamic viscosity of the liquid since it is based on Stokes Law (Equation 2-1). These values were taken as follows:

$\rho_s=2,580 \text{ kg/m}^3$ – based on direct density of solids calculation for the AD Mud sample.

$\rho_w=996 \text{ kg/m}^3$ – based on published density data for sodium phosphate and water solution.

$\mu_w=0.000785 \text{ Pa-s}$ - based on published viscosity data for sodium phosphate water solution.

Three samples were prepared and run from different parts of the collected 300 gallons of bulk sample with the aggregated result shown in Figure 2-5.

The wet sieve and SediGraph results describe AD Mud from this area of the topset to be approximately 8% sand, 24% silt and 68% clay. This result agrees reasonably well with an independent analysis of sediment from the same approximate location done by *Neill and Allison*. Their results are shown in Figure 2-7. The most dominant grain size fraction in the AD Mud is clay and this fraction will be the focus of further analysis. Clay minerals are hydrous aluminum silicates broadly categorized as phyllosilicates due to their sheet-like atomic structure. It is this structure that makes X-ray diffraction an effective method for identification of the specific mineral groups present in clay.

2.3.4 Mineral Composition

Mineral composition is one of the primary factors that determine the strength of the bed structure and consequently how it behaves in response to wave forcing. Composition depends on the pedigree of the erodible material existing in the drainage basin as well as any anthropogenic introduction of material into the basin.

The X-ray Diffraction (XRD) method, used for mineral identification, is based on hitting a powdered mount sample of the sediment with an X-ray beam at an angle and measuring the scatter intensity of the beam and scatter angle of the X-ray energy. Each mineral element in the silt and clay fractions has a unique crystalline structure which tends to be ‘platey’ in shape and produces a unique scatter angle which is related to the structure of the mineral through Bragg’s Law (Equation 2-6) [*Lambe and Whitman*, 1969].

$$n\lambda = 2d \sin \theta \quad (2-6)$$

n =integer number representing order of reflection, λ =wavelength of the X-ray, d =spacing between sets of parallel scatter planes defined by the crystalline lattice of the mineral and θ =the angle between the incident beam and scatter plane.

Mineral identification is made by comparing the results against a database of powdered diffraction patterns known as the Powder Diffraction File (PDF) maintained at the International Center for Diffraction Data [ICDD, July 2008].

2.3.4.1 Silt / Clay fraction composition

Figure 2-8 shows the stacked results of five individual sample XRD powder-mount runs conducted at the Soil and Water Science Department Laboratory of the University of Florida for the silt/clay fraction of AD Mud. The results indicate a significant presence of quartz and more subtle returns for illite, feldspar and kaolinite. These results alone do not give a complete assessment of the mineral composition of AD Mud since both silt and clay fractions were tested together with the results biased towards the more symmetrical, larger silt sized mineral particles present in the mount. Quartz prevails as the dominant mineral in this test since it is likely one of the larger sized minerals in the silt/clay fraction and tends to be more spherical in shape.

2.3.4.2 Clay fraction composition

Additional X-ray Diffraction tests on the isolated clay fraction of AD Mud allowed the comparison of results obtained for the bulk silt/clay fraction and discernment of any differences in mineral composition between the silt fraction and the clay fraction. Samples of the AD Mud were wet sieved using a 4 ϕ sieve in order to retain just the silt and clay fractions, deflocculated/dispersed by adding sodium phosphate, homogenized and allowed to settle. The suspension was then sorted by grain size using a basic settling technique which applies the differential settling velocities of particles of varying size calculated by on Stokes Law to sort the

sediment in a quiescent settling column. After an appropriate settling time of the homogenized suspension, the particles still remaining in suspension are drawn off and represent the clay fraction of the sample.

Since many clay minerals have similar lattice structures, results from a single X-ray diffraction test would lead to inconclusive determination of the specific minerals present thus additional X-ray diffraction tests were necessary. The clay fraction sample was titrated onto two porous clay tiles placed under suction to orient the clay particle structures and assist in aligning them parallel to the clay tile surface.

One tile was treated with liquid potassium (K) and the other tile treated with magnesium and glycol (Mg-Gl). This procedure is used to isolate the clay mineral smectite from another clay mineral illite since the d-spacing of the smectite and illite lattices are very similar and difficult to distinguish based on the X-Ray diffraction results of the K-treated sample alone. The differences become apparent through comparison of the K and Mg-Gl treated sample XRD results. Smectite swells when saturated with ethylene glycol (Mg-Gl treatment) causing a shift to a higher d-spacing to occur with X-ray diffraction while illite does not show any shift [Bradley, 1945]. Another procedure to differentiate smectite from illite involves heating the clay to 300° C. This procedure collapses the lattice of smectite which is revealed by a shift to lower d-spacing with X-ray diffraction. As seen in Figure 2-9, comparison of the K-treated samples at 25° C and 300° C reveals the presence of both minerals. The Mg-Gl treated sample also reveals the distinct presence of both smectite and illite. In summary, the clay fraction of AD Mud contained a significant amount of smectite as well as illite, kaolinite and quartz.

Although not indicative of absolute concentrations of the various minerals present in the mud, a comparison of the heights of the peaks at each mineral group d-spacing (Figure 2-9)

indicates relative quantities of each. The results show a significant quantity of quartz in the clay fraction but to a lesser extent than the overwhelming amount indicated in the silt fraction. This result is reasonable as quartz is a very erodible and abundant mineral in this region and the weathering and diagenesis processes break down this mineral across all grain sizes.

A study of the mineral group composition of the Mississippi River drainage basin by *Griffin* [1962] reported that the approximate clay composition of the suspended sediment in the Mississippi River was 60-80% montmorillonite (smectite), 10-20% kaolinite and 20-30% illite. These results coincide with the map of dominant mineral groups of the same drainage basin found by soil sampling and presented in the same report (Figure 2-6).

2.3.5 Clay Chemistry and Structure

In reference to Figure 2-5, AD Mud is 68% clay with an average grain size of 0.6 μm . Due to the crystalline lattice plate structure of clay, the specific surface, defined as surface area per mass, is large and as a result, the relative influence of the clay particles' electric charge to the influence of its mass is large. For comparison, the specific surface of 0.1mm quartz is 0.03 m^2/g and the specific surface of smectite is 1000 m^2/g [*Lambe and Whitman*, 1969]. Since clay minerals have a net negative charge owing to vacancies or unbalanced ionic substitutions in its crystalline structure, it readily hydrates (i.e. bonds with cations present in the water). A double layer of water (electrolyte) forms around the clay particle which in turn results in a significant bound water content of the saturated clay [*Lambe and Whitman*, 1969].

$$\text{water content} = \text{specific area} \left(\frac{\text{m}^2}{\text{g}} \right) * \text{water layer thickness (m)} * \text{water density} \left(\frac{\text{g}}{\text{m}^3} \right) \quad (2-7)$$

For AD Mud, water content can be approximately 50% of the total volume even at efficient self-weight packing as a result of the double water layer. Assuming a two water

molecule thick layer (5 angstroms) of bound water, the water content of the smectite particle is calculated by Equation 2-7.

$$\text{water content} = \left(1000 \text{ m}^2 / \text{g}\right) * \left(5 \times 10^{-10} \text{ m}\right) * \left(1 \times 10^6 \text{ g/m}^3\right) = .50 = 50\%$$

This calculation shows that the upper, self-weight consolidated, AD Mud seabed would most likely never have a solids volume fraction greater than $\phi_{vs} = \frac{(0.50 * \rho_s + 0.50 * \rho_w) - \rho_w}{\rho_s - \rho_w} = 0.50$.

Several aggregate structures can occur as a result of bonding between clay particles. A net negative charge of the clay particle is primarily present along the crystal faces while the edges have a small but positive charge present which tends to facilitate edge-to-face bonding under these conditions [Van Olphen, 1963]. Under weak ionic conditions such as in fresh water, the double water layer is thinner due to a lack of cations and as a result adjacent particles can approach closer in this edge-to-face orientation.

For clay particles in saline water, the abundant sodium provides plentiful cations and a thick double layer develops. This layer maintains greater separation between particles so the aggregation of these particles tends to be through the sharing of the cations of the double layer favoring a more parallel, face-to-face orientation.

The affinity to attract and bond with cations is a function of a mineral's negative charge and is known as the cation exchange capacity (CEC) expressed in terms of milliequivalents per 100 grams of dry clay sample (me/100g). Smectite has a very high CEC=100 me/100g as compared with kaolinite having a CEC=3 me/100g, and as a result smectite has the potential to form stronger, more coherent, bonds than kaolinite. The tendency of sodium saturated smectite to disperse and swell results in the clay having low permeability. Low permeability causes AD Mud

to resist normal pressure gradients which tend to make wave pressure fluctuations of secondary importance to bed dynamics compared to shear stress induced by water particle motion.

2.3.6 Order of Aggregation

The variable nature of aggregate shape and structure forming a mud seabed makes direct geometric interpretation of aggregates based on these properties difficult. *Krone* [1963] introduced an “order of aggregation” concept as a way to characterize the seabed as a cluster of discrete structures. Figure 2-10 represents this concept diagrammatically. The fundamental structural element is the primary particle aggregate ($n=0$), which is of uniform porosity and is formed from the flocculation of ionized clay particles. Based on the stress condition in the vicinity of the particles, these primary particle aggregates may gently collide with other primary particle aggregates to form a weaker and more loosely packed higher order aggregate with its own porosity and strength. Equation 2-8 relates the density of a specific higher order aggregate to the density of the fundamental primary particle aggregate through the void ratio of the primary particle aggregate.

$$\phi_{vf\ n} = \phi_{vf1} [1 + (n-1)e_1] \quad (2-8)$$

With ϕ_{vf_n} = volume fraction of aggregate order ($n-1$) and e_1 = voids ratio of the 0th order aggregate.

$$e_1 = \frac{\phi_{vf2} - \phi_{vf1}}{\phi_{vf1}} \quad (2-9)$$

As aggregates of a given order combine to form a higher order aggregate structure, an assumption is made concerning the self-similarity of these successive higher order aggregates to the next lower order aggregate by Equation 2-10.

$$e_i \phi_{vf\ i} = e_{(i+1)} \phi_{vf(i+1)} \quad (2-10)$$

The order of aggregation concept introduced here will be discussed throughout this study and applied to relate the shear strength of a mud seabed to aggregate structure in Chapter 4.

Due to the randomly oriented ‘card house’ arrangements of aggregates formed during quiescent settling and consolidation of a mud bed, significant void space is created which results in a low degree of bed consolidation. Through external forcing by current or waves as well as gravity forcing due to self-weight, alignment begins to take place among the aggregates and the spacing becomes more uniform as the particles tend to align with each other. This orientation process reduces the viscosity of AD Mud, thus contributing to its thixotropic nature when exposed to a shear force.

2.4 AD Mud Seabed Characterization

External forcing from currents or waves enables fine grained sediment to remain, or become, entrained in the water column. As long as forcing is strong enough, the state of suspension of the particles continues. Once the forcing diminishes or terminates, the particles begin a sequence of settling and become part of the seabed. The sequence of bed formation as it pertains to this study involves depositional settling and self-weight consolidation processes. Beds which have been consolidated by surcharge or overburden will not be addressed. Four different phases of settling and consolidation can be defined, each with its own characteristic behavior and duration which depend on both the material properties of the sediment and the chemical properties of the pore water. The four phases are free settling, flocculation settling, hindered settling, and self-weight consolidation.

An experimental test was conducted to measure the settling and consolidation characteristics of AD Mud. There were two objectives for this test.

-The first objective was to understand the duration of each of the four settling phases based on the initial homogeneously suspended solids volume fraction. This is important to be able to

predict how long it will take for entrained sediment to become consolidated bed material after episodic forcing has subsided.

-The second objective of this test was to determine the solids volume fraction (Equation 2-11) profile with depth into the bed once the sediment has reached the consolidated bed phase. This analysis is important to adequately define the density profile of the bottom boundary and will be applied during analysis of the wave flume tests.

The state of a mud bed forced by currents or waves changes continually so its properties must be known in time and space in order to properly define the boundary conditions. It is best defined by the solids volume fraction profile as this represents density or concentration in a non-dimensional form. Solids volume fraction, ϕ_{vs} , is defined as the ratio of the volume of the solids component of the mud sample to the total volume.

$$\phi_{vs}(t) = \frac{[\rho(t) - \rho_w]}{(\rho_s - \rho_w)} \quad (2-11)$$

ρ =bulk density of the sediment sample, ρ_w =density of seawater, ρ_s =density of solids.

2.4.1 Settling and Self-Weight Consolidation Analysis

Six, 250 ml graduated cylinders were used to simultaneously test six discrete initial solids volume fraction ϕ_{vs} of the AD Mud (Figure 2-11). Durations of each phase of settling/consolidation as well as bed density profiles were recorded. The range of final consolidated bed thicknesses in the six cylinders was inclusive of the thickness of the AD Mud bed to be placed in the wave flume and will be used as a basis to determine the time to consolidation for this bed and the associated ϕ_{vs} profile.

2.4.2 Settling Profile

The suspensions were prepared by diluting an aliquot of AD Mud with native seawater from the collection site in the Gulf of Mexico until the bulk density of the 250 ml sample reached the value required for the designated ϕ_{vs} (Table 2-3). Native water was used to ensure that the chemical and ionic properties of the pore water were maintained given their significant influence on the aggregation properties [Van Olphen, 1977]. The samples of all six cylinders were vigorously agitated to ensure an initial homogeneous suspension in the cylinder. Care was taken not to entrain air into the suspension during the agitation process as this has been shown to significantly influence the settling behavior of the mud by trapping micro air bubbles in the particle matrix of the mud [Brennen, 1995]. Because of the large density difference between the air bubbles ($\rho=1 \text{ kg/m}^3$) and the sediment mixture ($\rho=1,020\text{-}1,400 \text{ kg/m}^3$), any micro-bubbles trapped in the aggregate would reduce its settling velocity and thus retard the settling and consolidation processes [Dingemans, 1998].

Lutocline levels (i.e. levels at which high gradients in concentration were visible) were recorded at discrete time intervals for 60 days. During the settling phases of the test, only one lutocline was discernable at all times in each of the cylinders. The measurement results are shown in Figure 2-12 with the four phases of sediment settling: free settling, flocculation settling, hindered settling and consolidation, identified by distinct changes in the rate of settling. These phases are best observed in the data for cylinders #1-#4. Due to the higher initial ϕ_{vs} in cylinders #5 and #6, the flocculation and hindered settling phases appear to be coincident as the particles collide and form higher order aggregates almost immediately.

During the free settling phase the low settling rate, due to the low order aggregates as a result of the agitation process, is governed by Stokes Law and is independent of the

concentration of the sediment mixture. This is evidenced by the similar initial slopes of the settling curves of the first four cylinder samples. Within minutes for the lower ϕ_{vs} suspensions (cylinders #1, #2) and longer for the higher ϕ_{vs} suspensions (cylinders #3, #4), the flocculation settling phase begins. At this phase, particles have aggregated into higher order, heavier floc structures which settle out of the water column at a faster rate. As the lutocline continues to settle, ϕ_{vs} increases and the aggregates begin to interfere with the escape of water from beneath the settling material. As a result, the suspension settling rate decreases indicating the start of the hindered settling phase. Finally, the suspension begins to form a bed and the consolidation phase begins. The bed becomes relatively stable with further settling taking place at an extremely slow rate as the self-weight of the bed material compresses the bed which causes further re-alignment and orientation of the aggregates and de-watering of the bed through the tortuous interstitial paths.

Based on these results, the time necessary for the AD Mud suspension placed in the wave flume to settle into a consolidated bed was determined as follows: First, the total height from water surface to bottom of flume was selected as 27 cm. The designed final bed thickness was 8 cm, therefore, $h/h_o = 8 \text{ cm} / 27 \text{ cm} = 0.296$. Entering the y-axis of Figure 2-12 at this value and reading down from the dashed consolidation phase trend line shows that approximately 60 h ($1/\text{time}=0.0003 \text{ min}^{-1}$) are required from initial deposition for the suspension to become a consolidated bed. The results happen to coincide with the data for Cylinder #3 simply because the ratio h/h_o for both Cylinder # 3 and the wave flume were the same. Since the time to consolidation depends on the ratio, h/h_o , the time to consolidation must be calculated each time this ratio is changed.

2.4.3 Consolidated Bed Solids Volume Fraction Profile

The second objective of this same experiment was to determine the ϕ_{vs} profile with depth for a consolidated bed up to a terminal thickness of 16 cm as depicted in Cylinder #6. This profile was established by calculating the bulk density of the bed for each of the six cylinder samples. Since these beds form in quiescent conditions under self-weight, the bulk density of the bed in previous cylinders can be superimposed on to the top sections of the subsequent cylinder beds (Figure 2-13) building an incremental bed density profile. The density of the bed in Cylinder #1 can be determined using Equation 2-12. It is important to consider bed density as a function of time since, even after the bed forms and begins to consolidate, secondary consolidation and de-watering of the bed continues to alter the bed density over several months.

$$\rho(t)_{\text{bed A=bed } \#1} = \frac{m_{\text{total } \#1 \text{ (tare)}} - V(t)_{\text{water } \#1 \text{ (measured)}} \rho_{\text{water}}}{V(t)_{\text{bed A (measured)}}} \quad (2-12)$$

The calculated density of the bed in Cylinder #1 represents the density for the top section of equal thickness in beds #2–#6 (Figure 2-13). This incremental stacking can be continued so that a composite density profile can be derived for Cylinder #6 using Equations 2-13 to 2-17.

$$\rho(t)_{\text{bed B}} = \frac{m_{\text{total } \#2 \text{ (tare)}} - V(t)_{\text{water } \#2 \text{ (measured)}} \rho_{\text{water}} - \rho(t)_{\text{bed A}} V(t)_{\text{bed A}}}{V(t)_{\text{bed B (measured)}}} \quad (2-13)$$

$$\rho(t)_{\text{bed C}} = \frac{m_{\text{total } \#3 \text{ (tare)}} - V(t)_{\text{water } \#3 \text{ (measured)}} \rho_{\text{water}} - \rho(t)_{\text{bed A}} V(t)_{\text{bed A}} - \rho(t)_{\text{bed B}} V(t)_{\text{bed B}}}{V(t)_{\text{bed C (measured)}}} \quad (2-14)$$

$$\rho(t)_{\text{bed D}} = \frac{m_{\text{total } \#4 \text{ (tare)}} - V(t)_{\text{water } \#4 \text{ (measured)}} \rho_{\text{water}} - \sum_{n=A}^C \rho(t)_{\text{bed n}} V(t)_{\text{bed n}}}{V(t)_{\text{bed D (measured)}}} \quad (2-15)$$

$$\rho(t)_{\text{bed E}} = \frac{m_{\text{total } \#5 \text{ (tare)}} - V(t)_{\text{water } \#5 \text{ (measured)}} \rho_{\text{water}} - \sum_{n=A}^D \rho(t)_{\text{bed n}} V(t)_{\text{bed n}}}{V(t)_{\text{bed E (measured)}}} \quad (2-16)$$

$$\rho(t)_{\text{bed F}} = \frac{m_{\text{total #6 (tare)}} - V(t)_{\text{water #6 (measured)}} \rho_{\text{water}} - \sum_{n=A}^E \rho(t)_{\text{bed n}} V(t)_{\text{bed n}}}{V(t)_{\text{bed F (measured)}}} \quad (2-17)$$

The result of this analysis for the total bed of Cylinder #6 is shown in Figure 2-14 with the calculated densities displayed in terms of ϕ_{vs} . The depths are defined in reference to the constant water surface elevation of Cylinder #6 at the 250ml mark. Tiers of ϕ_{vs} at intervals throughout the bed for each of the four settling time intervals are evident. This is consistent with the findings in similar previous studies [Been and Sills, 1981].

Observed density profiles for mud from the Scheldt River in Belgium tested in a consolidation column are shown in Figure 2-15 as functions of consolidation time. There are distinct jumps in the density profiles of both AD Mud and the Scheldt River mud which indicates that a strength threshold exists in the aggregate structure of the bed. Very near the surface, there is little overburden pressure so the integrity of a weaker, higher order aggregate is sustained. At a certain depth, the increased overburden pressure causes the aggregate structure to collapse to the next lower order which is reflected in a jump to the ϕ_{vs} of that order of aggregation.

For AD Mud, the first tier occurs at approximately $\phi_{vs}=0.055$ and is consistent over all durations. The depth of this tier was observed visually as a markedly less dense ‘dusting’ at the lutocline interface with a thickness of approximately 2 mm. The ϕ_{vs} of this thin layer was approximated as slightly less than half of the computed ϕ_{vs} of the bed layer immediately below. By day 2 the lutocline had settled to approximately 2.5 cm below the water surface of Cylinder #6. Directly below the ‘dusting’ layer at day 2, $\phi_{vs}=0.118$ and appears to transcend the entire bed almost uniformly. On day 3, the bed shows consolidation from the bottom upward into the bed which indicates draining of pore-water. Of interest to note is that even after 56 days, ϕ_{vs} of the

top tier below the 'dusting' layer had not changed substantially. This implies that $\phi_{vs}=0.13$, shown as the vertical broken line on the right, represents the material strength of 0th order aggregate AD Mud. The meaning of this bed concentration will be analyzed in Chapter 4.

From the ϕ_{vs} profile shown in Figure 2-14, some information can be inferred regarding the state of the bed. Specifically, from the discussion on water content for smectite in Section 2.3, the measured ϕ_{vs} values are much lower than the calculated maximum ϕ_{vs} for a smectite mud, $\phi_{vs(max)}=0.50$, based on the double layer thickness. This implies that the natural AD Mud bed contains free pore water not strongly bonded as the double layer and/or the aggregate structure is not comprised of particles completely oriented in a parallel, efficient form. For a completely saturated smectite mud, $\rho_{max}=1,800 \text{ kg/m}^3$ is the limiting density for $\phi_{vs}=0.50$ assuming a 5 Angstrom thick water layer. This condition would occur at extreme overburden pressures when the structure of the mud has the most efficient orientation of the particles in the lowest order aggregate state. The approximate percentage of pore water that is free in AD Mud of $\phi_{vs}=0.13$ is 74% computed by Equation 2-18.

$$\%_{\text{free porewater}} = 100 * \frac{\phi_{vs \text{ max}} - \phi_{vs \text{ actual}}}{\phi_{vs \text{ max}}} \quad (2-18)$$

With duration of exposure to self-weight overburden, this free water slowly drains from the bed resulting in an increase in effective stress as the bed is supported more by the aggregate structure. Overburden alone can only drain free pore water to a certain extent. Once the effective stress is equal to the hydrostatic pressure, the semi-symmetrical structure of the aggregate supports all the pressure force and there is no pressure gradient to expel additional free pore water. Only when additional overburden or induced bed motion compromise the aggregate

structure and cause excess pore pressure, can additional pore water drain and increase consolidation.

In summary, AD Mud may be characterized as a predominantly smectite based, highly cohesive, clay sediment with low organic content. As a deposited bed material, AD Mud demonstrates a tiered density profile with depth which may be attributed to its flocculated order of aggregation structure. Knowledge of AD Mud properties based on the results from this chapter will be applied next to study the dynamic response of the mud to water wave induced shear stress.

Table 2-1. Tests used to characterize AD Mud properties

Characterization Test	Purpose
-Density of Solids	Enables determination of the solids volume fraction profile of the bed.
- Loss on Ignition	Determines presence of organic and inorganic carbon compounds
- Sieve / Sedigraph Analysis	Characterizes the grain size distribution
- X-Ray Diffraction (XRD)	Identifies the mineral constituents

Table 2-2. Loss on Ignition test results.

Sample #	Tare mass (g)	Gross mass (g)	Sample mass (g)	Combusted sample mass (g)	Loss on Ignition (g)	% loss (%)
1a	12.8014	13.8614	1.0600	0.9884	0.0716	6.754717
1b	13.5443	14.6460	1.1017	1.0278	0.0739	6.707815
1c	11.7787	12.8127	1.0340	0.9650	0.0690	6.673114
2a	12.3682	13.3763	1.0081	0.9401	0.0680	6.745363
2b	12.7867	13.8037	1.0170	0.9481	0.0689	6.774828
2c	12.9803	14.0324	1.0521	0.9824	0.0697	6.624846
3a	11.7777	12.7315	0.9538	0.8893	0.0645	6.762424
3b	12.1895	13.1076	0.9181	0.8568	0.0613	6.676833
3c	13.1403	14.1186	0.9783	0.9128	0.0655	6.695288

Table 2-3. Initial solids volume fraction of cylinder sediment, Figure 2-11.

Cylinder #:	1	2	3	4	5	6
Solids Volume Fraction, ϕ_{vs}	0.018	0.025	0.036	0.060	0.093	0.120



Figure 2-1. Atchafalaya and Mississippi River deltas.

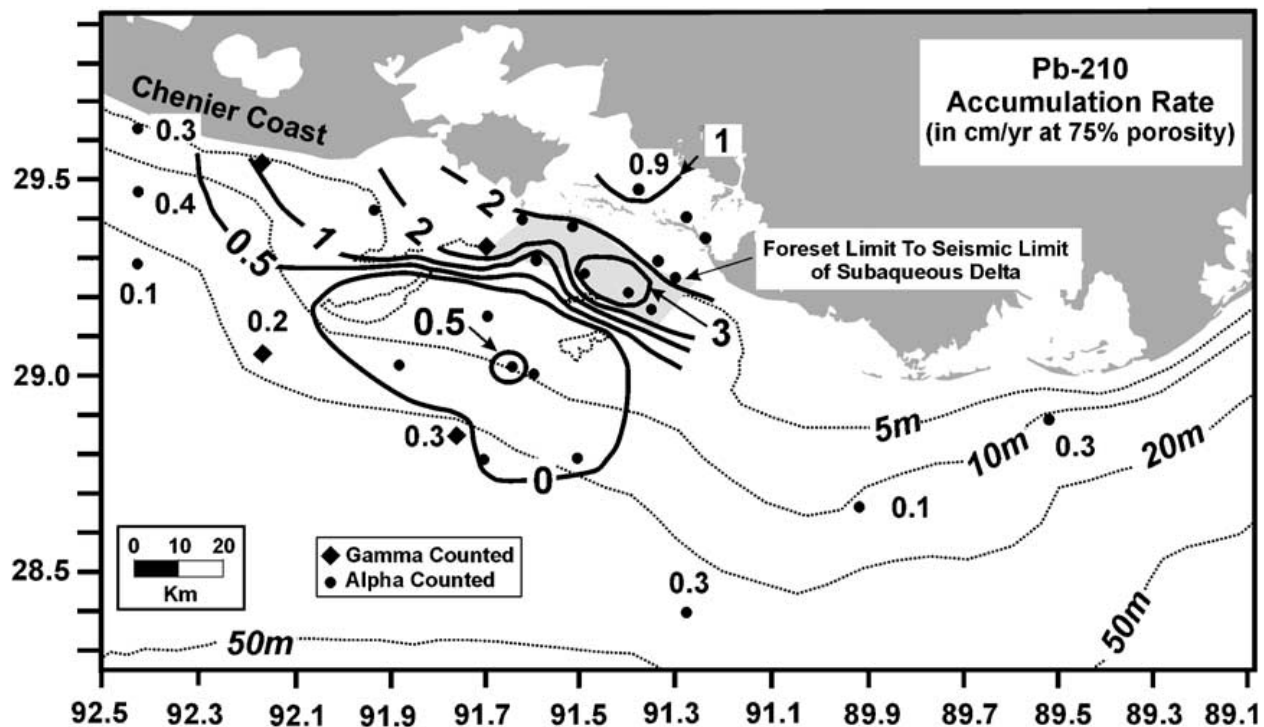


Figure 2-2. Sediment accumulation rates along the Atchafalaya subaqueous delta as determined by ^{210}Pb analysis [Neill and Allison, 2005].



Figure 2-3. Site of seabed sampling coincident with WAVCIS CSI3 monitoring station.

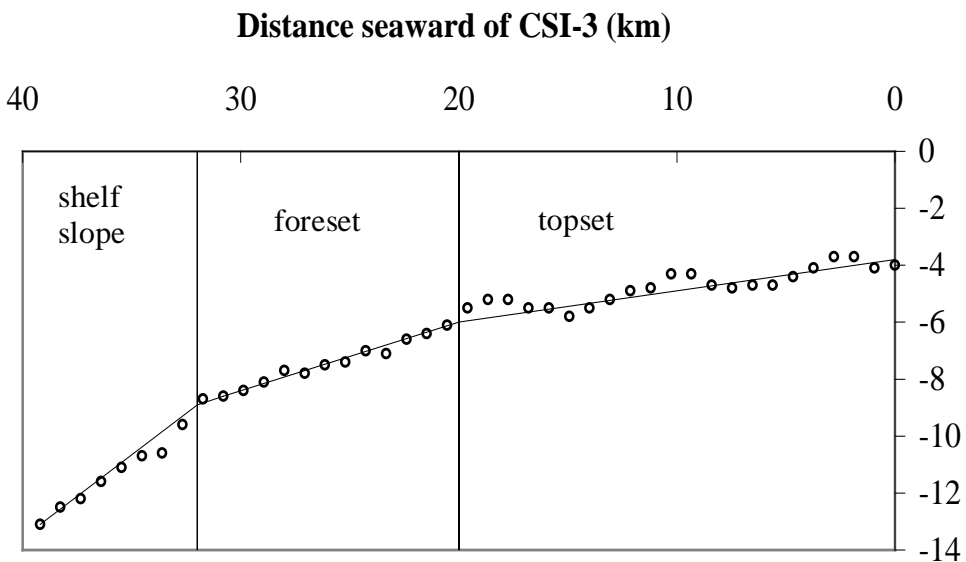


Figure 2-4. Clinoform bed profile seaward of CSI3 site. Depths obtained from NOAA GEODAS database. Solid lines represent slope trends and vertical dashed lines indicate boundaries of topset, foreset and shelf slope sections based on slope transitions. (Data source: <http://www.ngdc.noaa.gov/mgg/geodas/geodas.html>, last accessed June 2008)

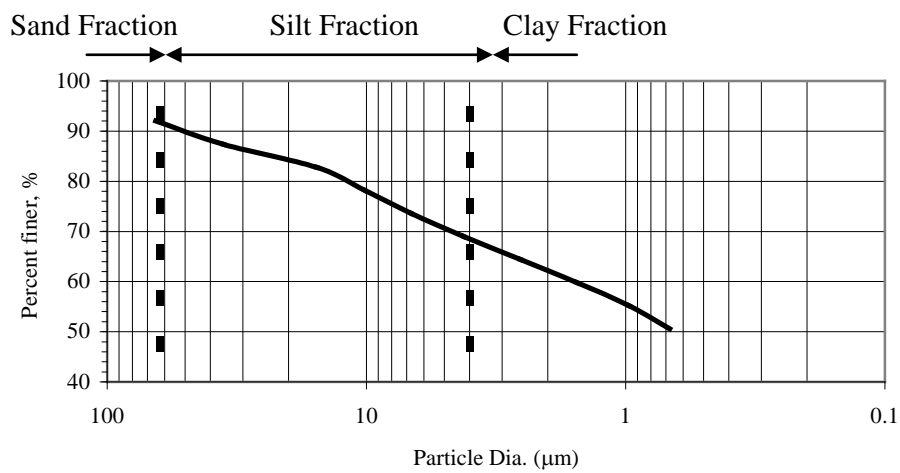


Figure 2-5. Wet sieve and Sedigraph results – AD Mud.

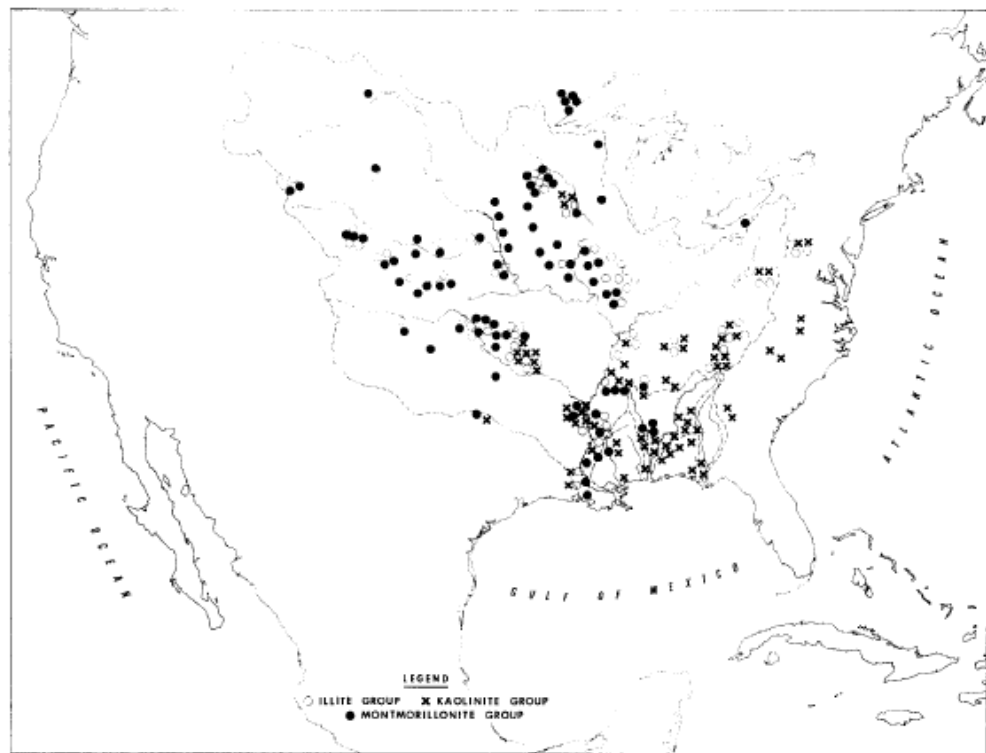


Figure 2-6. Mississippi River drainage basin indicating dominant mineral group distribution of tested soil samples [Griffin, 1962].

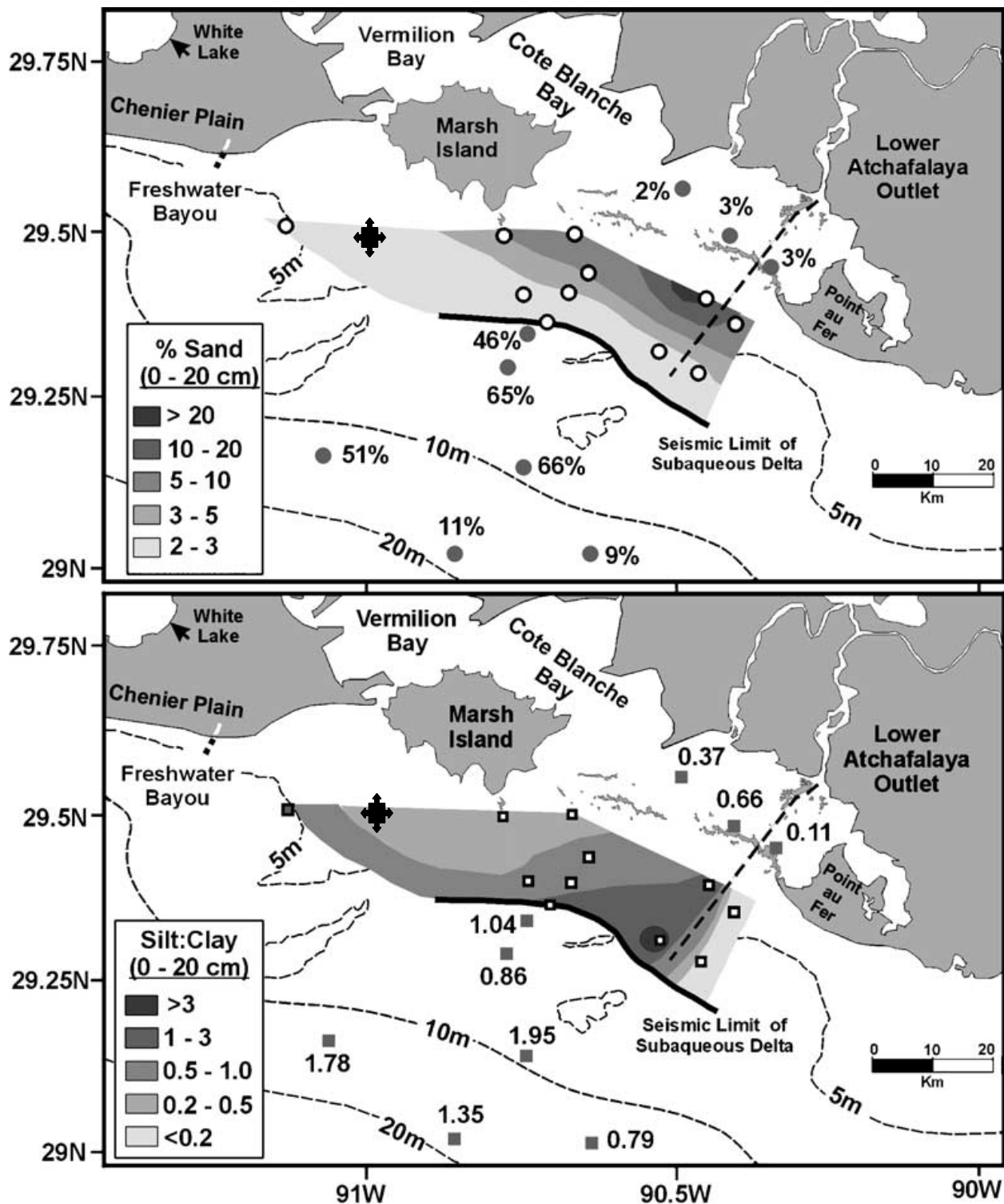


Figure 2-7. Sand/silt/clay fractions of the top 20cm of seabed along the outer topset and foreset regions of the Atchafalaya delta clinoform [Neill and Allison 2005]. The sample collection site for analysis in this study on the outer western edge of the topset is depicted by the quad arrow symbol.

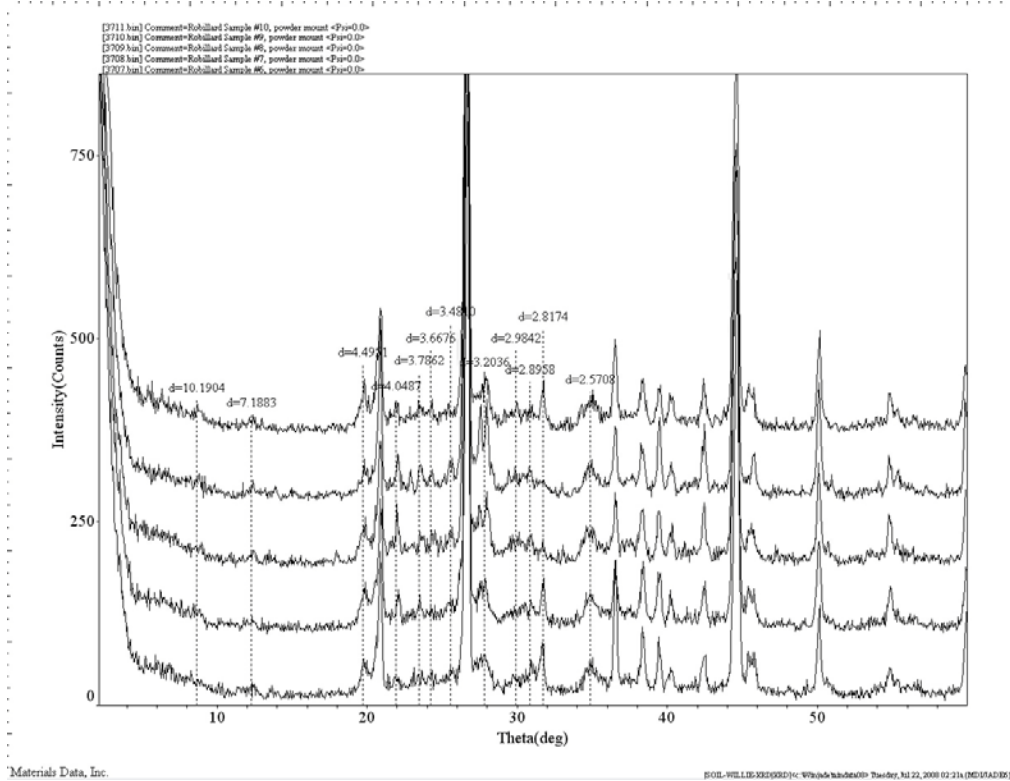


Figure 2-8. XRD result for combined AD Mud silt/clay fraction.

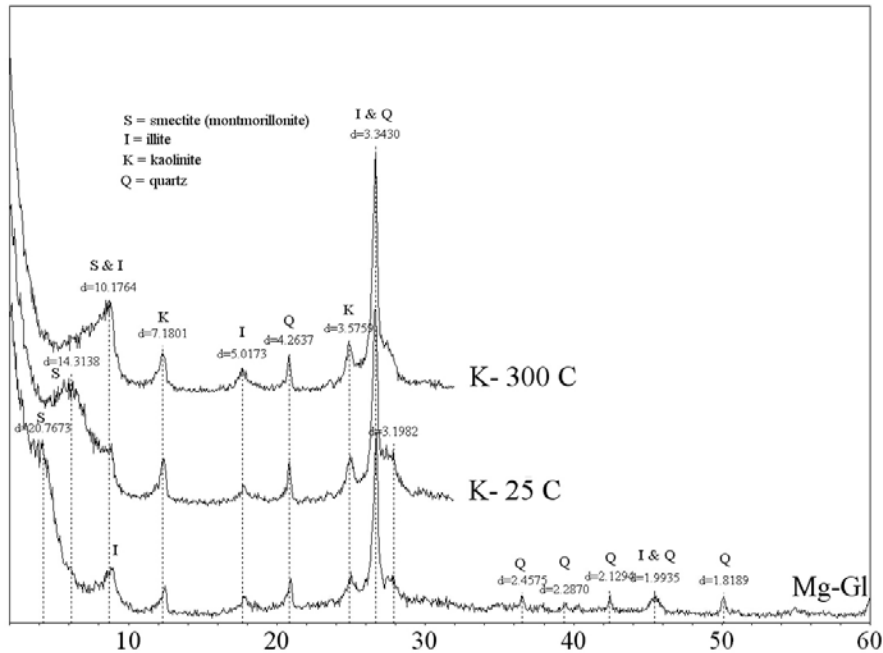


Figure 2-9. XRD result for isolated AD Mud clay fraction.

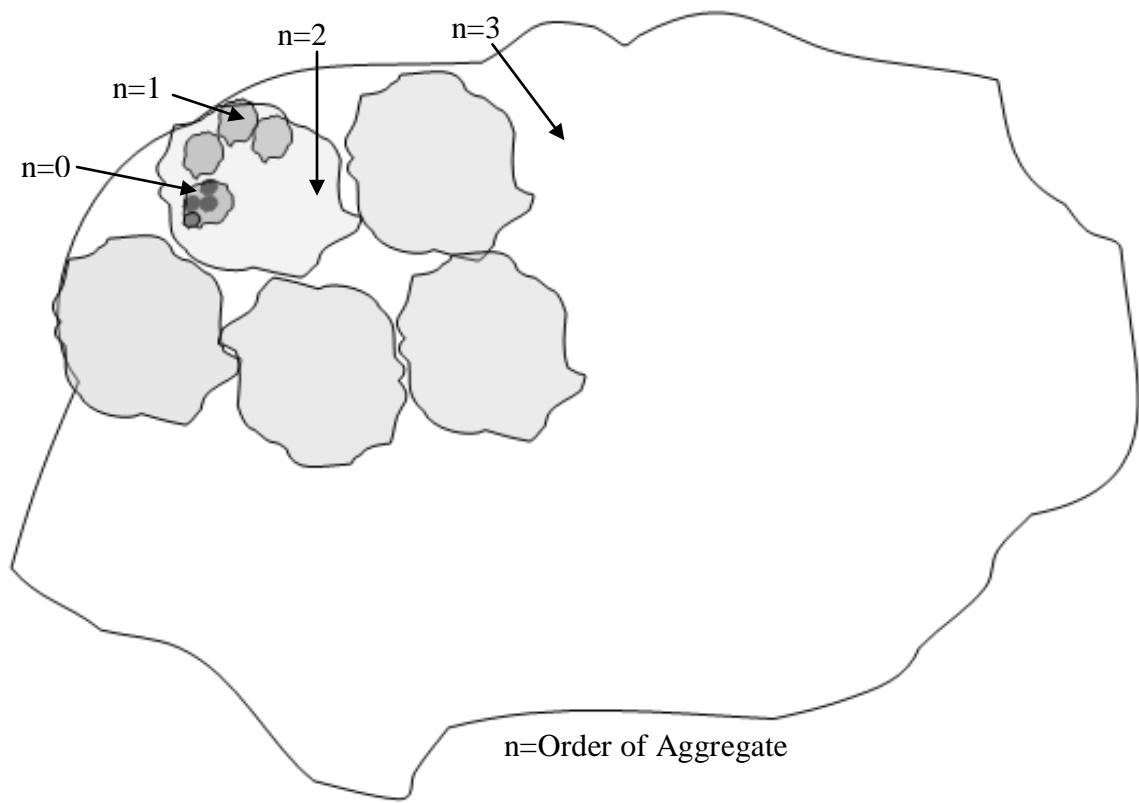


Figure 2-10. Diagrammatic representation of order of aggregate concept used to define the structure of mud (adapted from Krone, 1963).

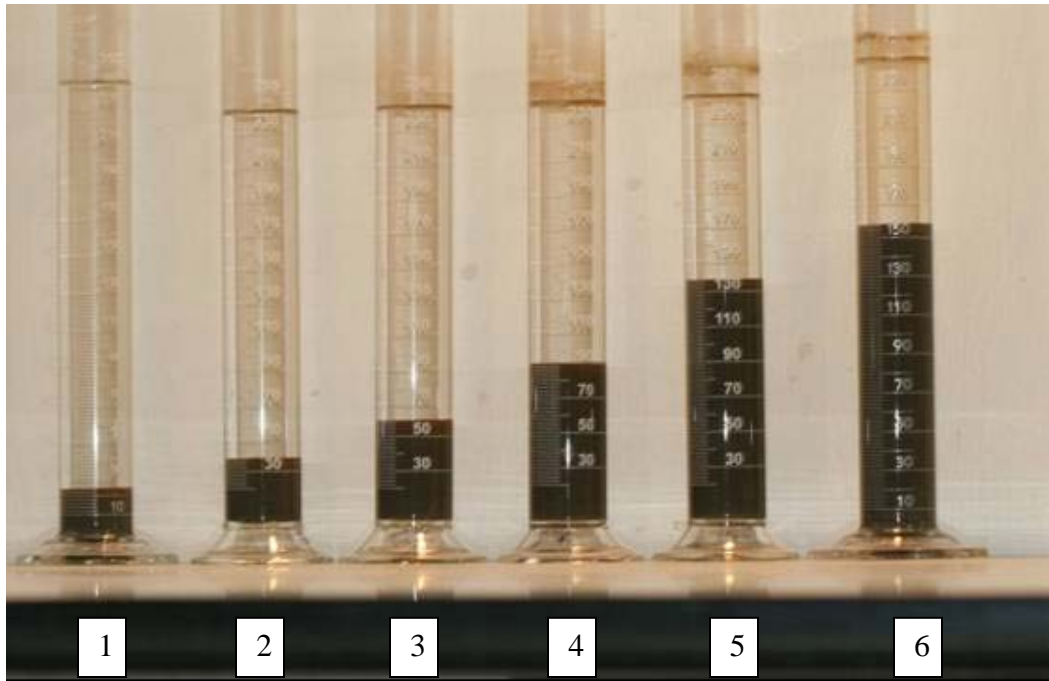


Figure 2-11. 250 ml graduated cylinders used as settling columns to measure settling and consolidation characteristics of six discrete solids volume concentration samples of AD Mud.

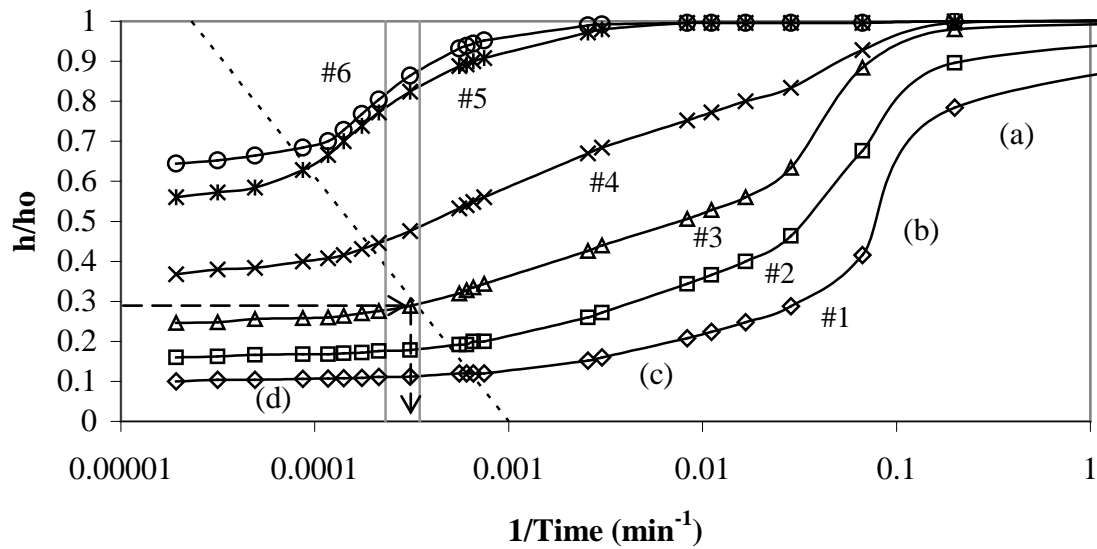


Figure 2-12. Self-weight settling and consolidation results for AD Mud. Dashed line ---: time trend to reach consolidation phase. Gray vertical lines denote 48 hr-72 hr time range. Dashed arrows denote time to consolidation of the wave flume bed described in Section 2.4.2. (a)-(d) indicate free settling, flocculated settling, hindered settling and consolidation phases, respectively. #'s indicate Cylinder # .

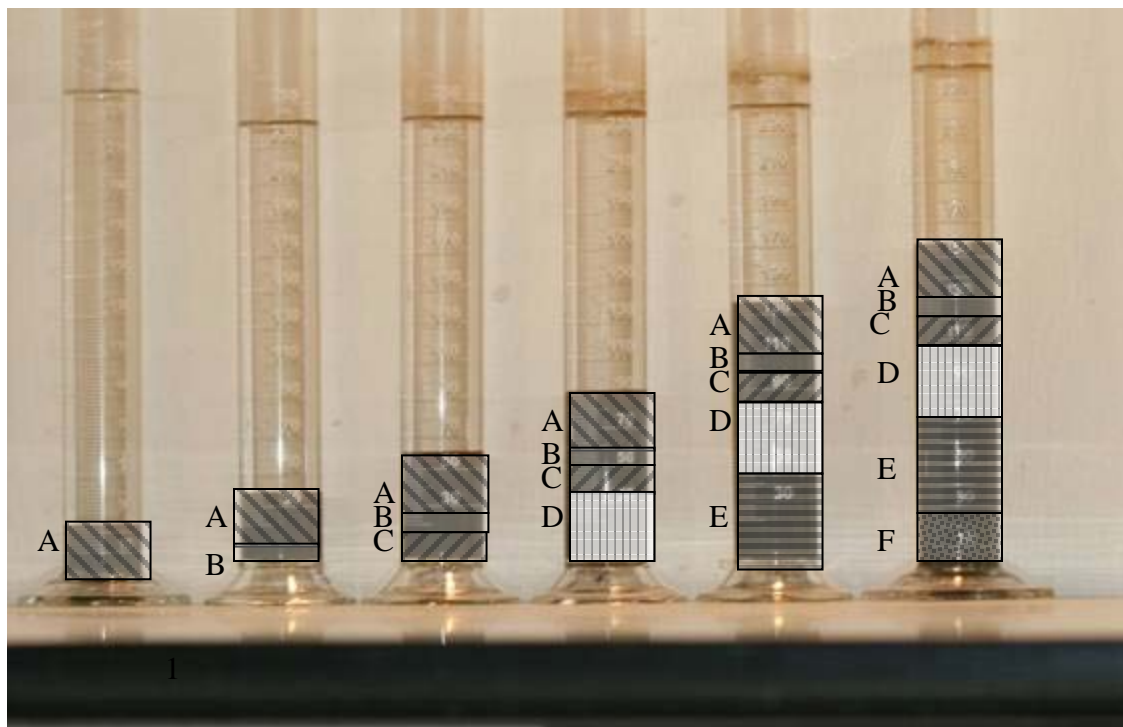


Figure 2-13. Representation of equivalent solids volume fraction layers of AD Mud thickness superimposed sequentially on cylinder sample images.

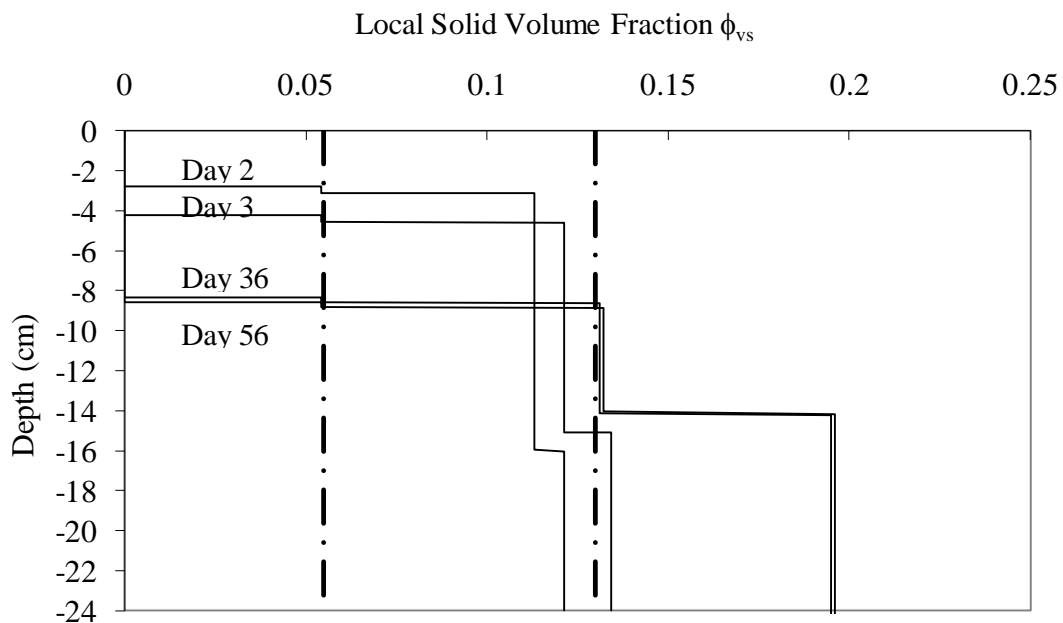


Figure 2-14. AD Mud local solids volume fraction profiles with depth for Days 2, 3, 36 and 56. Depth axis denotes lutocline level in Cylinder #6 wrt 250ml water mark on that cylinder. Vertical broken lines indicate two relatively constant final density gradients evident in the near surface thickness of the bed.

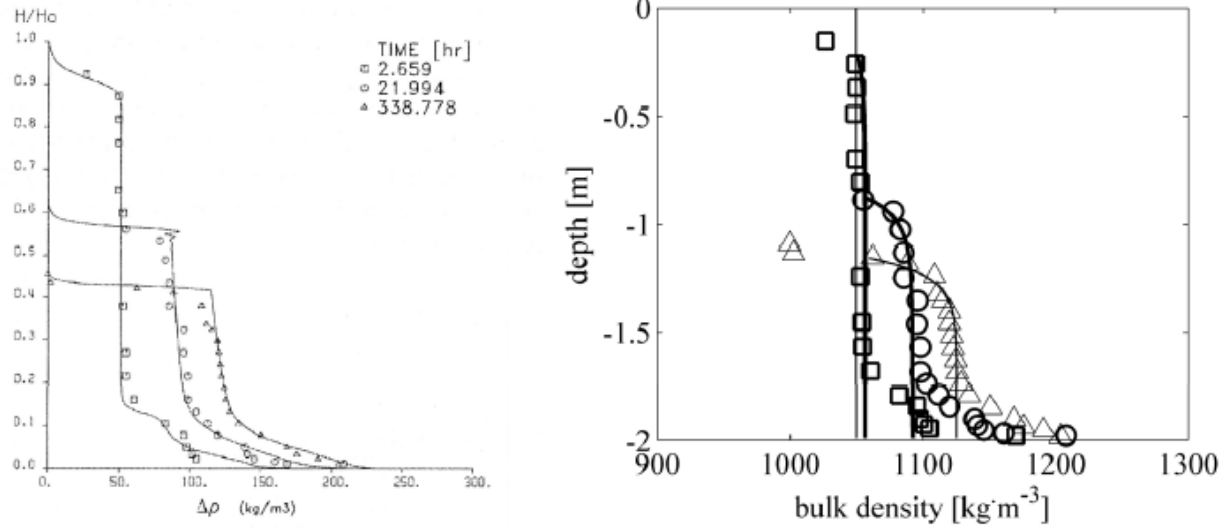


Figure 2-15. Vertical density profiles of mud from Scheldt River, Belgium. Figures present same data in different units. [Toorman and Berlamont, 1991]

CHAPTER 3

ATCHAFAHALAYA DELTA MUD DYNAMIC BEHAVIOR

3.1 Constitutive Models

This chapter describes how AD Mud responds to oscillatory shear stress under laboratory conditions. A rheometric approach is used to simulate the oscillatory shear stress which would occur by wave propagation over a seabed. Since a muddy seabed is composed primarily of a matrix of clay particle aggregates and water filling the interstitial spaces, it can exist in a variety of states from a weakly viscous liquid to a near-solid. For classification purposes soft seabed mud can be referred to as a complex or structured viscoelastic liquid.

According to Hooke's Law, stress, σ , is proportional to the strain, γ , for an elastic solid under simple shear deformation. The proportionality coefficient, E , an intrinsic property of the material, is the elastic (Young's) modulus. It relates uniaxial stress to uniaxial strain for an isotropic material. The shear modulus of elasticity, commonly designated by the symbol G , relates shear stress to shear strain. For a homogeneous isotropic material, G is related to E by Poisson's ratio, v , which relates the change in material length normal to an applied load to the resulting change in length of the material in the two planes perpendicular to the applied load.

$$E = 2G(1+v) \quad (3-1)$$

Figure 3-1 illustrates the definition of σ and γ . Eq. 3-2 describes Hooke's Law under shear stress conditions.

$$\sigma = G\gamma \quad (3-2)$$

Newton [1687] stated "The resistance which arises from the lack of slipperiness originating in a fluid-other things being equal-is proportional to the velocity by which the parts of the fluid are being separated from each other." The proportionality coefficient viscosity, μ , relates the

time rate of change of strain, $\dot{\gamma}$, to the shear stress (Eq. 3-3). Figure 3-1 illustrates the definition of $\dot{\gamma}$.

$$\sigma = \mu \dot{\gamma} \quad (3-3)$$

As a complex liquid, AD mud may exist in a state with significant elastic properties or as a purely viscous liquid. The general constitutive equation for a viscoelastic material defined by Equation 3-4 incorporates both Hooke's Law and Newton's definition.

$$\sigma + \alpha_1 \dot{\sigma} + \alpha_2 \ddot{\sigma} + \dots = \beta_0 \dot{\gamma} + \beta_1 \ddot{\gamma} + \beta_2 \dddot{\gamma} + \dots \quad (3-4)$$

α_i and β_i are intrinsic material properties related to the associated time derivative of the shear stress or strain, respectively. For an elastic solid, the only non-zero material property parameter is β_0 and this is typically designated by G as described by Hooke. For a viscous liquid, the only non-zero material property parameter is β_1 and this is typically designated by μ as described by Newton.

Mechanical analogs have been used to describe viscoelastic behavior in its simplest form by various combinations of a spring and a dashpot. The spring serves to represent the elastic material property and the dashpot to represent the Newtonian (viscous) material property. The two basic linear viscoelastic models are the Voigt model and the Maxwell model. The Voigt model is represented by a parallel orientation of a constant coefficient spring and a constant coefficient dashpot. As a result both elements experience the same deformation (Figure 3-2a). The Maxwell model is represented by a series orientation of the same components and therefore the elements experience the same stress (Figure 3-2b).

The following constitutive equations define the models depicted in Figure 3-2:

$$\sigma = G\gamma + \mu \dot{\gamma} \quad \text{Voigt Model} \quad (3-5)$$

$$\sigma + \left(\frac{\mu}{G} \right) \dot{\sigma} = \mu \dot{\gamma} \quad \text{Maxwell Model} \quad (3-6)$$

More complex models have been defined based on combinations of Voigt and/or Maxwell elements resulting in additional non-zero parameters of the general viscoelastic equation described by Equation 3-4. These models become mathematically challenging to apply and difficult to relate to the natural dynamics of a physical problem. Based on experimental or field data, the multiple parameters of Equation 3-4 can not be resolved without ambiguity. Unless the structure of the material contains multiple, distinct contributors to its rheology, a more complex viscoelastic model is not warranted. As a result, the approach of this study is to assess the validity of the simplest model that accurately represents the rheology of the mud seabed in order to minimize the number of parameters required in Equation 3-4.

3.2 Material Response to Stress

Due to the diverse nature of material's response to stress, an understanding of the specific boundary value problem is necessary to ensure the appropriate rheological properties of the material are measured. This entails understanding the orientation of stresses and defining the constitutive equation which best represents the nature of how the material responds to stress. The orientation of stress will determine the relative motion of the material particles. Under shear stress, adjacent material particles will move over or past each other while under normal stress, adjacent particles will move away or towards each other (Figure 3-3).

3.2.1 Characterization of Seabed Stresses

Shear stress imposed on a compliant muddy seabed by wave induced water motion generates motion in the bed. The upper layer of the bed becomes the active boundary layer where primary wave dissipation takes place. Due to bed motion, the compliant mud seabed has

been shown to dissipate significantly more wave energy than a rigid impermeable seabed [Mathew *et al.*, 1995]. In order for bed motion to occur under gravity, shear stress must exist within the bed. This stress can be generated by forces normal to the bed (pressure) or parallel to the bed (shear) or a combination of the two.

Figure 3-4 depicts the relationship between the normal stresses, σ_x and σ_y , and the shear stresses, τ_{xy} and τ_{yx} . The symbol convention throughout this paper represents shear stress as σ . Only in this section and Section 3.2.2 will the symbols σ and τ be used to represent normal and shear stress, respectively for ease of distinction while discussing both types of stress. Considering the inset figure of the material cube, these stresses can be resolved into only principal normal stresses, σ_1 and σ_2 , by reorienting the cube face. Resolution of these stresses defines the maximum shear stress shown by Equation 3-7 and the angle of the material plane it acts on as a result of forcing.

$$\tau_{\max} = \left(\frac{\sigma_2 - \sigma_1}{2} \right) \quad (3-7)$$

Anywhere in a muddy bed where the maximum shear stress, τ_{\max} , exceeds the bed shear strength, transition of the bed will occur. In this area of the bed, the effective stress, derived from the strength of the aggregate particle matrix component of the mud, becomes zero and the bed exists in a liquid state completely supported by the total pressure of the pore water. The extent of transition into the bed depends on the stress forcing. As long as there is motion in the bed, there will be wave dissipation attributed to that motion. Various testing techniques are available to measure the impact of external forcing on a complex liquid such as marine mud. The two primary types of tests are triaxial tests and shear rheometer tests. The problem of interest dictates which rheological test protocol is appropriate.

In some situations, bed motion can be induced predominantly by axial forcing. This may occur in confined harbors subjected to the pumping motion of standing wave forcing. To replicate this type of forcing in the laboratory, a triaxial test would be the most suitable. For completeness, this test will be briefly introduced though not discussed in detail as it is not the test protocol which represents the problem of this study.

3.2.2 Triaxial Testing

Triaxial tests are performed on a cell of the material sample constructed in a sleeve and confined with a certain lateral pressure (Figure 3-5). The sample is then subjected to an axial deviator stress. This test produces particle motion as depicted in the extensional flow diagram of Figure 3-3. The principle normal pressure forces are measured and defined as σ_1 and σ_3 (Figure 3-5). The deviator stress, defined as the difference between the total axial stress, σ_1 , and the confining normal stress, σ_3 , causes a shear stress to develop and produce motion of the particles of the sample material.

This deviator stress must be non-zero in order for bed motion and transition of the bed to be possible. If an undrained, triaxial test were conducted on a saturated viscoelastic liquid sample with rigid sleeve walls, no bed motion would occur. This is so because rigid walls do not allow a deviator stress to develop so $\sigma_1=\sigma_3$ and the solution appears as a single point on the x-axis of the (well-known) Mohr's circle and therefore no motion occurs. In other words, a fluid at rest cannot support shear stress. The normal stress on any plane through a fluid element at rest is equal to the confining pressure at that point. Any experimental approach designed to measure seabed response to deviator stress forcing must accommodate sample motion laterally in order for a shear stress to develop in the bed.

3.2.3 Shear Rheometry

The most regularly encountered forcing in open water locations such as the topset and foreset regions of the Atchafalaya Delta, is from progressive water waves and tidal/coastal currents. The main source of shear stress is from horizontally dominant orbital motion of the water particles at the bed surface, u , (Eq. 3-8).

$$u = \frac{H}{2} \omega \frac{1}{\sinh kh} \cos(kx - \omega t) \quad (3-8)$$

Where H =water wave height (m), k =wave number, $2\pi/\lambda$ (1/m), h =local water depth (m), and ω = wave angular frequency, $2\pi/T$ (rad/s).

To replicate shear stress conditions resulting from horizontal water particle velocity, u , shear rheometry is appropriate. The viscoelastic properties of a material in response to shear stress and the appropriate constitutive equation are determined through two types of shear rheometer tests.

The continuous flow creep test is the first test type and is conducted under a continuous flow condition with external forcing imposed over a range of time. The test is performed to identify the appropriate constitutive equation to use for representing the behavior of AD Mud. The second test type is conducted under oscillatory flow conditions with shear stress imposed over a range of frequencies. The protocol is meant to simulate the forcing on the mud seabed by waves and determine a flow equation to represent the response of AD Mud over a range of wave forcing. The rheometric experiments were performed using a controlled stress/controlled strain rheometer.

3.3 Rheometer

Controlled-stress /controlled-strain rheometry is an effective approach to measure the deformation of mud in response to oscillatory shear stresses induced by waves. The TA

Instruments AR2000ex (Fig. 3-6) with concentric cylinder geometry can test materials from low density liquids to high density solids. It has a shear stress range from 6×10^{-3} to 1.94×10^4 Pa and a controlled strain range from 2.9×10^{-5} to 2.86×10^2 . The rheometer can also perform dynamic oscillations from 7.5×10^{-7} to 6.28×10^2 rad/s. The air bearing design of the torque motor results in a large torque to inertia ratio. The inertial effects of the mechanical components are calibrated for each dynamic test setting and the data are corrected to compensate for this effect. As a result, highly accurate stress-strain rate resolutions are realized.

3.3.1 Temperature Consideration

For problems involving temperature as a first order variable influencing the material, the AR2000ex Rheometer also has the ability to control temperature of the test material from -40°C to 200°C. Since the bed temperature of the Atchafalaya Delta region only varies by approximately 10°C (17°C-27°C) over the seasonal time scale, 20°C will be used as the representative bed temperature. For studies comparing the performance of marine mud exposed to drastic temperature changes, temperature could be a very significant variable as it has a profound influence on material rheology.

3.3.2 Instrument Geometry

There are a variety of geometries available for use with the AR2000ex Rheometer. Selecting the appropriate geometry for a material and dynamic forcing is critical in order to obtain reliable measurement results. Concentric cylinder geometries are advantageous over other geometries such as cone-and-plate or parallel plate geometries (Figure 3-7) for testing mud since the measurements using a concentric cylinder geometry are not as adversely impacted by particle settling away from the measuring surface so low density mud can be measured. These advantages are especially significant when testing under low stress forcing encountered when evaluating the response of marine mud.

Within the concentric cylinder geometry category there are several options. The most common include conical DIN, double wall and vane geometry. Again the appropriate geometry within this group depends on the application. For a suspension with particles and pore water, the vane geometry is appropriate (Figure 3-7). This is due to its ability to minimize the adverse impact of wall slip or wall depletion.

3.4 Rheometer Testing Artifacts

The main concerns with rheometer testing involving complex liquids are wall depletion and secondary flow. These effects can be minimized by proper design of the test protocol but can not be eliminated and thus will influence the data. Identification of these test artifacts can be made with an understanding of the properties of mud and how the solid and pore water components contribute to the response of the mud.

3.4.1 Wall Depletion

Wall depletion may occur when any multi-phased or complex liquid (e.g. AD mud) is confined by a smooth, solid boundary and in motion. The mud particles can not ‘penetrate’ the solid boundary and as a result become depleted from the boundary leaving a lower viscosity layer of water along the boundary. This phenomenon may misleadingly imply that the no-slip boundary condition is violated. In cases involving highly viscous polymer melts actual separation from the smooth boundary may occur. However, considering the relatively low solids volume fractions in marine mud this effect will be assumed to be secondary.

Wall depletion can be compounded by gravity if the surfaces of the instrument test geometry are horizontal. This is the case with a cone and plate geometry (Figure 3-7). The particles will ‘settle’ by gravity and be drawn away from the top boundary causing an even more drastic depletion. In the extreme case, a water layer forms at this boundary and the effect is present regardless of the shear rate. Studies of flocculated clays using a cone and plate geometry

have resulted in significantly lower measured viscosity results when compared to the same material tested using a concentric cylinder geometry. This difference is attributed to a depleted water-dominant layer [*Boardman and Whitmore, 1963*]. The boundaries of concentric cylinder geometries are oriented vertically so gravity has no influence and only wall depletion must be considered.

Direct measurements from the rheometer must be analyzed for this effect. The most vulnerable tests for wall depletion include low frequency, low strain rate, oscillatory forcing of flocculated mud of high solids volume fraction. For oscillatory testing of marine mud, both of these conditions are encountered under certain wave forcing and density of the material. At higher frequencies and strain rates, centrifugal force tends to counteract wall depletion and holds the particles closer to the wall. Since wall depletion is most significant when the liquid is comprised of large flocs, the effect lessens with increased shear stress as the stronger forcing breaks down the flocs. This effect on rheometric data becomes exaggerated when analyzing material response over a range of low to high shear stresses.

3.4.2 Wall Depletion Reduction

Use of the vane geometry with tests on liquids prone to wall depletion is the best method to minimize this effect (Figure 3-7). This is because the rotating inner boundary is almost entirely replaced with the material itself so the possibility of wall depletion at is removed. Under most test conditions, this geometry is enough to make wall depletion insignificant to the results since the response of this boundary is what is measured during testing. The outer cylinder wall, though a static boundary, still will contribute to potentially significant wall depletion under certain test scenarios. Evidence of wall depletion will manifest itself similar to the results depicted in Figure 3-8. A false yield is seen in the data at a point in the flow curve and a Newtonian plateau appears. It is possible that the material actually undergoes these changes due

to its structural response to forcing. However, when this effect is seen with reference to the testing of marine mud, it is more likely due to an artifact of the measurement technique. Where this complete or partial, double sigmoidal shape occurs as the actual response of a material to stress and not an artifact is when two separate shear-thinning mechanisms are present in the material. An example would be a liquid with a flocculated suspension and shear-thinning pore liquid. Carbon black in molten rubber is an example of a material which demonstrates this response [Barnes, 1995]. AD mud only contains one shear-thinning mechanism which is the suspension of clay aggregates since the pore water is not shear-thinning.

It is of interest to note that the physical process replicated in the rheometer is a simulation of pipe flow. Raw data represent the material response due to the presence of the pipe wall. Since the objective of this study is to simulate shear forces over an infinite mud seabed, this result is considered an undesirable artifact that must be compensated for during post-processing of the data.

3.4.3 Secondary Flow

Another effect that must be considered when testing complex liquids in a rheometer is secondary flow. This is most likely to occur with low solids volume fractions at high shear rates (the opposite conditions conducive to wall depletion). Inertia-driven secondary flow appears in the form of Taylor vortices. These vortices will distort the data and their onset marks the upper limit of reliable data for that sample. There is no direct way to compensate for this effect. The Taylor Number, Ta , for concentric cylinder geometries described in Barnes [2000] relates the importance of rotational force to viscous force (Equation 3-9).

$$Ta = 2 \left(\frac{r_i}{r_o} \right)^2 \frac{(r_o - r_i)^4}{\left(1 - \left(\frac{r_i}{r_o} \right)^2 \right)} \left(\frac{\rho \omega}{\mu} \right)^2 \quad (3-9)$$

Where,
 r_i = radius of inner cylinder (rotating) (m)
 r_o = radius of outer cylinder (stationary) (m)
 ρ = density of sample (kg/m³)
 ω = angular velocity (rad/s)
 μ = dynamic viscosity of sample (Pa-s)

Another non-dimensional group used to represent critical oscillatory flow in a rheometer (with vane concentric cylinder geometry) is presented for consideration. Since it has been

□
demonstrated that the rate of strain, γ , has a significant influence on the viscosity of the liquid, it would seem appropriate that a critical non-dimensional number relating inertial effects to viscosity in a rheometer include this term.

The Ekman Number relates the inertia and viscosity in reciprocal form as,

$$\text{Ekman Number, } Ek = \frac{\mu}{\rho \omega L^2} \quad (3-10)$$

with L serving as a length scale of the process being analyzed. Equation 3-11 is another possible Taylor Number considering the same length scale, L, proposed by *Barnes* [2000].

$$Ta' = \left(\frac{r_i}{r_o} \right) \frac{(r_o - r_i)^2}{\sqrt{1 - \left(\frac{r_i}{r_o} \right)^2}} \frac{|\gamma| \rho}{\mu} \quad (3-11)$$

Qualitatively the upper limit of good data at high rotation rates can be identified directly as the point where the viscosity measurements begin to become sporadic. Pre-test start-up procedures for the AR2000ex Rheometer include performing rotational and/or oscillatory mapping. This mapping aspect of calibration considers any artifact to the data due to small

variations in the torque of the air bearing. Small variations in torque are mapped through the range of conditions anticipated for the specific test to be conducted. As a result, real-time corrections for inertia are already applied and, instead of the critical Taylor Number, Ta' , occurring when $Ta' \ll 1$, it occurs at around the order 1. The range of dynamic testing performed as part of this study remained below this threshold so secondary flow did not influence the measured data.

3.5 Rheometer Test Protocols

3.5.1 Continuous Flow (Creep) Test

A creep test is performed by applying a constant stress for a period of time and monitoring the resulting strain both during loading and after loading is terminated. Analysis of how a material responds under this forcing is important when the natural system involves high stresses and long durations.

Material represented by a Voigt element responds in a different way during a creep test as compared to a Maxwell element. The creep test consists of an initial stage during which the material flow is measured in response to a constant shear stress followed by a stage where the stress is immediately stopped and the material undergoes recovery.

$$\sigma = \begin{cases} \sigma_0, & \text{for } 0 \leq t \leq t_1 \\ 0, & \text{for } t > t_1 \end{cases} \quad (3-12)$$

For the Maxwell model, creep can be described by Equations 3-13 and 3-14.

$$\gamma = \sigma \left(\frac{1}{G} + \frac{t}{\mu} \right) \quad \text{for } (0 \leq t \leq t_1) \quad (3-13)$$

$$\gamma = \sigma \left(\frac{1}{G} + \frac{t_1}{\mu} \right) \quad \text{for } (t > t_1) \quad (3-14)$$

The material responds linearly with an immediate elastic response until the stress is terminated. Due to the Newtonian liquid assumption, deformation continues linearly as long as the stress is imposed. Once the stress is terminated, the material maintains a constant strain characteristic of a liquid (Figure 3-9).

For the Voigt model, creep can be described by Equations 3-15 and 3-16.

$$\gamma = \frac{\sigma}{G} \left[1 - \exp\left(-\frac{G}{\mu} t\right) \right] \quad \text{for } (0 \leq t \leq t_1) \quad (3-15)$$

$$\gamma = \frac{\sigma}{G} \left[\exp\left(-\frac{G}{\mu}(t - t_1)\right) \right] \quad \text{for } (t > t_1) \quad (3-16)$$

With this model, the strain gradually increases and asymptotically approaches a maximum value σ_0/G . Once the stress is terminated, the strain gradually decreases to zero (Figure 3-9).

3.5.2 Oscillatory Flow Test

As progressive waves propagate shoreward, the shear stress on the seabed is periodic with the frequency of the wave so the dynamic forcing to be replicated by rheometer tests must be oscillatory. Oscillatory flow tests can be performed using the AR 2000ex Rheometer by controlling the stress or the strain. A controlled strain protocol was chosen over a controlled stress protocol in order to obtain greater resolution of viscosity data due to the thixotropic properties of AD Mud. Thixotropy will be discussed further in Section 3.6.2. Strain will be set as the independent variable defined as sinusoidal with a frequency, ω .

$$\gamma(t) = |\gamma| e^{-i\omega t} \quad (3-17)$$

The resultant shear stress, $\sigma(t)$, is also sinusoidal but with a phase shift, δ , and will be the dependent variable.

$$\sigma(t) = |\sigma| e^{-i(\omega t + \delta)} \quad (3-18)$$

The phase shift, δ , describes the viscoelastic properties of the AD mud. As a result, the shear modulus, G^* , is a complex variable with the real part, G' , representing the elastic or storage shear modulus and the imaginary part, G'' , representing the viscous or loss shear modulus.

$$G^* = G' - iG'' = |G|[\cos(\delta) - i \sin(\delta)] \quad (3-19)$$

A zero phase shift represents a completely elastic response and a phase shift of $\pi/2$ represents a completely viscous response. A phase shift between these two extremes characterizes viscoelastic response. The complex shear modulus, G^* relates shear stress to strain as, $\sigma = G^* \gamma$, while the complex viscosity, μ^* relates shear stress to rate of strain as, $\sigma = \mu^* \dot{\gamma}$. For oscillatory flow, μ^* is related to G^* by,

$$\dot{\gamma} = -i\omega\gamma \quad (3-20)$$

$$\sigma = G^* \gamma = (G' - iG'')\gamma \quad (3-21)$$

$$\sigma = \left(\frac{iG'}{\omega} + \frac{G''}{\omega} \right) \dot{\gamma} \quad (3-22)$$

For the Voigt model (Equation 3-5),

$$\sigma = \left(\frac{iG}{\omega} + \mu \right) \dot{\gamma} \quad (3-23)$$

Therefore,

$$G^* = G - i\mu\omega \quad (3-24)$$

$$\mu^* = \mu + \frac{iG}{\omega} \quad (3-25)$$

The real viscosity component describes the viscous response of the material and the imaginary component describes the elastic response. Expressed in terms of phase angle, δ , gives,

$$G = G' = \frac{\sigma}{\gamma} \cos \delta = \frac{\sigma \omega}{\gamma} \cos \delta \quad (3-26)$$

$$\mu = \frac{\sigma}{\gamma \omega} \sin \delta = \frac{\sigma}{\gamma} \sin \delta \quad (3-27)$$

3.6 Characteristics of Seabed Response

3.6.1 Yield Stress

As evidenced by Equations 3-5 and 3-6, neither the Voigt model nor Maxwell model recognizes the concept of a yield stress. The flow curve section FG (Figure 3-10) is approximated as an extension of the linear portion of the curve. The value of stress at the x-axis intercept is defined as the yield stress. By definition, the yield stress assumption implies no strain rate exists below this shear stress and any material deformation would be purely elastic.

If the strain rates and shear stress forcing are in proximity to the yield stress and greater, it would be appropriate to use a constitutive equation involving the yield stress. If however, lower strain rates occur, it would be appropriate to forego the yield stress assumption in favor of a non-linear representation of the stress-strain rate relationship which characterizes more completely the range of material motion.

3.6.2 Shear Thinning and Thixotropy

AD Mud does not behave as a Newtonian fluid but rather reveals a non-linear relationship between shear stress and rate of strain. As shear stress increases, viscosity decreases non-linearly. When this viscosity response to increased shear stress occurs instantly, the behavior is termed shear thinning. Though often considered collectively as the thixotropic effect, shear thinning and thixotropy are distinct behaviors of a complex liquid. Figure 3-11 is a generalized flow diagram showing the various material responses to stress and shows the distinction between shear thinning and thixotropic behavior. Shear thinning occurs when the shear stress continues

to increase. This increase breaks down the structure of the liquid until, if the shear stress is strong enough, it completely reduces the mud to a purely viscous liquid.

Thixotropy is a time-dependent behavior of a material and is almost always observed in complex liquids such as AD Mud. It is a more restrictive condition than shear thinning due to the added time dependence of the material property transformation. During rest, AD Mud is completely structured to the fullest extent possible for its solids volume fraction ϕ_{vs} and exhibits the most rigid elastic state possible. When this mud is exposed to a constant or increasing shear stress, the matrix begins to fail and, depending on the shear stress, will transform over a finite time period from a predominantly elasticoviscous state to a more viscoelastic state. Under strong enough shear stress, the mud structure could break down all the way to its primary aggregate state and the mud is then in a purely viscous state with no elasticity. This transition is not only induced by change in the shear stress but also by time of exposure to a constant amplitude shear stress. Thixotropy occurs because a finite length of time is required for the structure of the liquid to reach equilibrium with the imposed shear stress condition. This behavior is reversible and if the shear stress is terminated, the complex liquid would regain more of its elasticity with time and re-strengthen.

It is important to consider however, that the duration for the complex liquid to reach a steady state with the forcing will not be the same for breaking down under increased stress or recovering under reduced stress. Longer time will always be required to re-strengthen a broken down complex liquid since the primary restoring forces are due to Brownian motion. Breakdown of a complex liquid, however, can occur relatively quickly due to the presence of stress imposing a shear motion in the liquid and facilitating the rupturing of the aggregate bonds.

To demonstrate the thixotropic behavior of AD Mud, continuous time series runs under oscillatory flows were conducted on two AD Mud samples of different solids volume fractions (Table 3-1). In these tests the rate of strain was held constant and the shear stress with phase δ was measured by the rheometer. The components of the complex viscosity are thus obtained by Equation 3-28, and the phase angle relationship of the viscosity components are shown by Equation 3-29.

$$\mu^* = \sqrt{(\mu'')^2 - (\mu')^2} = \frac{\sigma}{\gamma} \quad (3-28)$$

$$\mu' = \mu^* \sin \delta \text{ and } \mu'' = \mu^* \cos \delta \quad (3-29)$$

3.7 Rheology Test Results

3.7.1 Continuous Flow (Creep) Tests

Creep tests were performed on AD Mud with solids volume fraction within the range $[0.112 \leq \phi_{vs} \leq 0.144]$. This range was selected to include the zero order aggregate ϕ_{vs} of AD Mud which is the typical concentration of in the near surface active seabed layer. The creep test imposed a constant shear stress of 0.5 Pa from time $t=0$ to time $t=30$ minutes. At time $t=30$ minutes, the shear stress was terminated and the mud allowed to relax for 30 minutes. To ensure accurate measurements of strain response along the creep curve, a precision requirement was programmed in the rheometer test protocol which required that three sequential readings measured at each time step were within 5% tolerance before the data point for that time was recorded.

Over the first 30 minutes, the AD Mud responds to the stress by a gradually decrease in viscosity (Figure 3-12). With time, the response asymptotically approaches a maximum. When

the stress is relaxed at $t=30$ minutes, the mud immediately responds with a drop in strain, with this trend continuing towards zero strain. Comparing the shapes of Figure 3-12 to the curves representing idealized Voigt and Maxwell models (Figure 3-9), it is clear that AD Mud very closely resembles the Voigt model. This demonstrates the significance of the flocculated particles that form an elastic structure in the mud. For this study, the general constitutive equation form representing a Voigt material will be used in analysis.

3.7.2 Oscillatory Flow Tests

3.7.2.1 Thixotropic response

In reference to Table 3.1, the AD Mud sample was exposed to a constant, low rate of strain for forty-two minutes. During phase 1 of both test runs, the viscosity adapted quickly to this low rate of strain as indicated by the near constant μ' and μ'' values (Figures 3-13 and 3-14). Phase 2 of the test imposed a higher constant rate of strain for sixty minutes at a magnitude that caused significant breakdown of the AD mud sample. This breakdown is evident by the switch in the dominant complex viscosity component. Initially the mud was in an elasticoviscous state with the imaginary (elastic) viscosity, μ' dominant over the real (viscous) viscosity, μ'' , but then transformed into a viscoelastic state. The AD Mud during phase 2 equilibrated with the higher shear rate within twenty-five minutes in Run 1 and almost instantly in Run 2. Phase 3 involved relaxing the strain rate down to the rate imposed during phase 1. Since the thixotropic effect is reversible, the mud should revert to the state it existed in just prior to the start of phase 2 at $t=42$ minutes. Though the mud sample recovered quickly to an elasticoviscous state as evidenced by the switch back in the dominant complex shear modulus component, it took several hours to revert completely back to the equilibrium value of phase 1. Based on the trend during this last

phase, it is anticipated that complete recovery of the mud would take hours to complete as shown by the projections of the light dashed lines starting at t=132 minutes.

The implication of thixotropic analysis is that AD Mud responds rapidly to an increased strain rate and *substantially* recovers rapidly with total recovery taking an order of magnitude longer. For time scales longer than minutes, the thixotropic response to increased oscillatory shear stress would be of secondary significance while the response to decreased oscillatory shear stress would have to be considered for several hours after the changed stress.

The test results indicate that AD Mud of higher solids volume fraction (Figure 3-14) tends to respond more rapidly to an increased rate of strain and takes longer to completely recover following a high rate of strain as compared to a lower solids volume fraction condition (Figure 3-13). A possible explanation for this result is that the higher solids volume fraction sample has a higher bond density as evident by viscosity values an order of magnitude greater in Run 2 compared to Run 1. Once the bonds begin to break in the higher solids volume fraction sample under increased rate of strain, a more rapid deterioration of structure occurs. Alternatively, as this sample rebuilds under a reduced rate of strain, the total number of bonds that need to be rebuilt is greater and thus takes longer to complete.

3.7.2.2 Bond density

The number of intermolecular bonds connecting the particles within a floc influence the floc strength and also the duration of its thixotropic response. The strength of these bonds is due to van der Waal's attractive forces between double layer clay aggregates. Assuming flocs are made up of randomly linked particles, *Cross* [1965] derived a relationship between the number of bonds and the rate at which the floc is either broken down or constructed (Equation 3-30).

$$\frac{dN}{dt} = k_2 P - \frac{k_0 N}{[\mu]} \quad (3-30)$$

N is the number of bonds linking adjacent particles, k_0 and k_2 are rate constants for Brownian collisions leading to breakdown and construction of the floc respectively, P is the particle density (number of particles per unit volume) and $[\mu]$ is a non-dimensional viscosity. The floc structure becomes stable with the imposed stress and the thixotropic response ends when the constructive and destructive components become balanced, $\frac{dN}{dt} = 0$ (Equation 3-31).

$$N_e = \frac{k_2 P [\mu]}{k_0} \quad (3-31)$$

Considering this derivation in terms of the order of aggregation concept discussed in Section 2.3.6, as lower order aggregates collide, they bond to form the next higher order aggregate. Due to the three-dimensional nature of an aggregate, this bonding occurs only at a two-dimensional contact surface between the two aggregates.

Assume that the bond density can be related in a self-similar way to the floc volume fraction by Equation 3-32.

$$\rho_{bn} \phi_{vfn} = \rho_{b1} \phi_{vf1} \quad (3-32)$$

A simple model is introduced to relate the bond density, $\rho_{bn}=N_n P_n$ of a particular order aggregate to the density of bonds of the primary particle aggregate, ρ_{b1} (Equation 3-33).

$$\rho_{bn} = \frac{\rho_{b1}}{[1 + (n-1)e_{v1}]} \quad (3-33)$$

This result demonstrates that the bond density, ρ_{bn} , forming the next higher order aggregate is reduced which is conceptually in agreement with the measured results from this study and with the findings of other researchers [Barnes, 1997].

Based on the assumed strength of a typical van der Waals bond to be $1 \frac{\text{kJ}}{\text{mol}}$ [Funk and

Dinger 1993], and the average AD Mud particle size = $0.6\mu\text{m}$ from the grain size analysis presented in Chapter 2, estimated bond density values are given in Table 3-2.

3.7.2.3 Oscillatory strain rate response tests

In order to determine the response of AD Mud to oscillatory forcing, strain sweep tests were conducted using the AR 2000ex Rheometer over the range of solids volume fractions identified as typical for that material in the consolidated state. This type of test is conducted by imposing an oscillatory rate of strain on the sample and recording the response when three consecutive data points converge to within 5% tolerance. The rate of strain is then incrementally increased or decreased through the defined range of shear rates. Table 3-3 describes the strain sweep parameters for the test runs performed. The tests were conducted to ensure the mud was subjected to typical wave frequencies. The selected ϕ_{vs} range was based on the self-weight consolidation analysis as described in Chapter 2.

Figures 3-15 to 3-20 show data for low, middle and high solids volume fractions for each angular frequency. All results show consistent characteristics of the flow curve that describe how AD Mud responds to an oscillatory shear stress.

3.8 Summary of AD Mud Response to Oscillatory Flow

3.8.1 AD Mud Property Response

Three distinct phases of AD mud behavior are evident in oscillatory strain sweep runs. Schematically, the flow response of AD Mud is depicted in Figure 3-21. To represent the dynamics of AD Mud as a complex liquid the data are presented in terms of complex viscosity,

μ^* , and rate of strain, $\dot{\gamma}$, as opposed to complex shear modulus, G^* and strain, γ which would

be more appropriate when analyzing a solid material. It can be recalled from the Voigt Model that,

$$\sigma = \mu^* \gamma = |\mu^*| [\sin(\delta) + i \cos(\delta)] \gamma \quad (3-34)$$

with,

$$\mu^* = \mu' + i\mu'' \quad (3-35)$$

where μ' is the real viscosity and μ'' is the imaginary viscosity representing the elastic component and related to the elastic modulus by Equation 3-36.

$$\mu'' = \frac{G}{\omega} \quad (3-36)$$

At low rates of strain, the AD Mud behaves as a linear elasticoviscous (LEV) liquid with the imaginary viscosity dominant over the real viscosity. During this phase, the viscosity components are independent of the rate of strain. Physically this implies that the AD mud is able to withstand low rates of strain and remains intact but with some energy dissipation due to mud motion. Test runs show that this linear elasticoviscous phase continues down to very low rates of strain. For all practical purposes, at the lower measured limit of this phase, the shear stress for this condition can be considered zero. This does not imply the existence of a yield stress at the limiting rate of strain but rather a practical limit to tangible effects of the forcing on the AD Mud.

As the rate of strain continues to increase, the structure of the mud begins to breakdown and it becomes a transitional viscoelastic liquid, (TVE), with both viscosity components having the same order of magnitude. In this phase, a noticeably steep decrease in μ'' occurs which one may interpret as yield behavior. This would be erroneous since significant wave-mud interaction takes place in the elasticoviscous phase which would be discounted in flow equations

defining a yield stress at the start of this transition phase. The appropriate interpretation of this phase is that it represents rates of strain that can no longer be resisted by the structure of AD mud. This is considered the phase in which transition of the AD Mud occurs.

In reference to Equation 3-34, transition will begin when the phase angle, δ , = $\pi/4$ indicating that both the real and imaginary viscosities are of equal magnitude. At this point the viscosity components cross-over and the real viscosity becomes dominant indicating a predominantly viscous state. The aggregate structure begins to break down and the mud reverts to a more elementary state of aggregation. The rapid decrease in μ'' reflects the cascading effect of structural failure. As initial bonds begin to fail, added stress is imposed on the remaining bonds. This failure continues until a lower order aggregate structure is reached where all remaining bonds are strong enough to withstand the external forcing. As described, lower order aggregates have significantly greater shear strength than higher order aggregates. In the case of the oscillatory strain sweep tests, the rate of strain is increased until complete failure of AD mud structure. This failure marks the purely viscous liquid phase (LV).

The purely viscous liquid phase occurs when the AD Mud reaches its basic aggregate structure. Since there are no further changes to the structure in this phase, the viscous response to further increased rates of strain remains constant. A linear viscous condition exists with the real viscosity independent of rate of strain. These distinct phases, (LEV, TVE, LV), exist regardless of whether the strain rate sweep is from low to high or high to low as evident in Figures 3-15 to 3-20. This consistency supports the results as a flow response inherent to the AD Mud's basic aggregate structure.

From the data shown in Figures 3-15 to 3-20, a flow equation of state for AD Mud over the complete range of strain rates will be derived in the next chapter and will serve as the basis for

developing a model which describes the wave energy dissipation properties of the AD Mud as well as motion and transition within the mud bed in response to oscillatory shear stress.

3.8.2 Influence of Stress History

In general, thixotropy is detected when the shear stress either increases or decreases from the equilibrium condition. An extreme thixotropic condition can be expected to occur from a significant increase in the wave-induced shear stress imposed on the mud bed. During the time period leading up to increased shear stress, the bed can be considered to be exposed to a low shear stress condition from a higher frequency wave (simulated by Phase 1, Table 3-1). Thus the bed would exist in a relatively rigid elasticoviscous state. Within tens of minutes from when the bed is exposed to increased shear stress and a lower frequency wave (simulated by Phase 2, Table 3-1), the bed will break down into a weaker, more viscoelastic state. This state will continue until the lower shear stress, higher wave frequency condition returns (simulated by Phase 3, Table 3-1). At that time, it will take several hours for the bed to regain its complete pre-high stress event equilibrium strength. As a result of thixotropy, the bed will respond different to the same change in shear stress condition depending on whether it was recently exposed to a high shear stress condition or not. All oscillatory tests performed will be treated under two stress history conditions as a way to account for thixotropy.

Table 3-1. Test protocol for continuous time series runs.

Run	Phase 1	Phase 2	Phase 3
1 $\phi_{vs} = 0.125$	$\omega = 7.300 \text{ rad/s}$ $ \dot{\gamma} = 0.1059 \text{ 1/s}$ Duration: 42 min	$\omega = 6.283 \text{ rad/s}$ $ \dot{\gamma} = 6.3854 \text{ 1/s}$ Duration: 60 min	$\omega = 7.300 \text{ rad/s}$ $ \dot{\gamma} = 0.1059 \text{ 1/s}$ Duration: 30 min
2 $\phi_{vs} = 0.214$	$\omega = 7.300 \text{ rad/s}$ $ \dot{\gamma} = 0.0285 \text{ 1/s}$ Duration: 42 min	$\omega = 6.283 \text{ rad/s}$ $ \dot{\gamma} = 1.7329 \text{ 1/s}$ Duration: 60 min	$\omega = 7.300 \text{ rad/s}$ $ \dot{\gamma} = 0.0285 \text{ 1/s}$ Duration: 30 min

Table 3-2. Bond density estimates for AD Mud aggregates. ** Aggregate shear strength estimates obtained from Krone [1963] ‘Gulfport Channel’ mud.

Order of aggregation	Aggregate shear strength, σ_n	Bond density, ρ_{bn}
n	(Pa) **	$\frac{\# \text{ Bonds}}{\mu\text{m}^3}$
0	4.6	2771
1	0.69	416
2	0.47	283
3	0.18	108

Table 3-3. Strain rate sweep test parameters.

Run #	Frequency (rad/s)	Solids Volume Fraction, ϕ_{vs}	Rate of Strain Range (1/s)*
Forward Strain Rate Sweeps (simulating low-stress initial condition):			
1F	5	0.0543	$1 \times 10^{-3} - 1 \times 10^2$
2F	5	0.1120	$1 \times 10^{-3} - 1 \times 10^2$
3F	5	0.1246	$1 \times 10^{-3} - 1 \times 10^2$
4F	5	0.1438	$1 \times 10^{-3} - 1 \times 10^2$
5F	5	0.2141	$1 \times 10^{-3} - 1 \times 10^3$
6F	1.57	0.0543	$1 \times 10^{-3} - 1 \times 10^2$
7F	1.57	0.1120	$1 \times 10^{-3} - 1 \times 10^2$
8F	1.57	0.1246	$1 \times 10^{-3} - 1 \times 10^2$
9F	1.57	0.1438	$1 \times 10^{-3} - 1 \times 10^3$
10F	1.57	0.2141	$1 \times 10^{-3} - 1 \times 10^4$
11F	0.628	0.0543	$1 \times 10^{-3} - 1 \times 10^2$
12F	0.628	0.1120	$1 \times 10^{-3} - 1 \times 10^2$
13F	0.628	0.1246	$1 \times 10^{-3} - 1 \times 10^2$
14F	0.628	0.1438	$1 \times 10^{-3} - 1 \times 10^3$
15F	0.628	0.2141	$1 \times 10^{-3} - 1 \times 10^3$
Reverse Strain Rate Sweeps (simulating high-stress initial condition):			
1B	5	0.0543	$1 \times 10^2 - 1 \times 10^{-3}$
2B	5	0.1120	$1 \times 10^2 - 1 \times 10^{-3}$
3B	5	0.1246	$1 \times 10^2 - 1 \times 10^{-3}$
4B	5	0.1438	$1 \times 10^3 - 1 \times 10^{-3}$
5B	5	0.2141	$1 \times 10^3 - 1 \times 10^{-3}$
6B	1.57	0.0543	$1 \times 10^2 - 1 \times 10^{-3}$
7B	1.57	0.1120	$1 \times 10^3 - 1 \times 10^{-3}$
8B	1.57	0.1246	$1 \times 10^3 - 1 \times 10^{-3}$
9B	1.57	0.1438	$1 \times 10^3 - 1 \times 10^{-3}$
10B	1.57	0.2141	$1 \times 10^4 - 1 \times 10^{-4}$
11B	0.628	0.0543	$1 \times 10^3 - 1 \times 10^{-4}$
12B	0.628	0.1120	$1 \times 10^3 - 1 \times 10^{-4}$
13B	0.628	0.1246	$1 \times 10^3 - 1 \times 10^{-4}$
14B	0.628	0.1438	$1 \times 10^4 - 1 \times 10^{-4}$
15B	0.628	0.2141	$1 \times 10^4 - 1 \times 10^{-4}$

Note * - The shear rate ranges were determined by the limiting capabilities of the AR2000ex Rheometer for test parameters of each run.

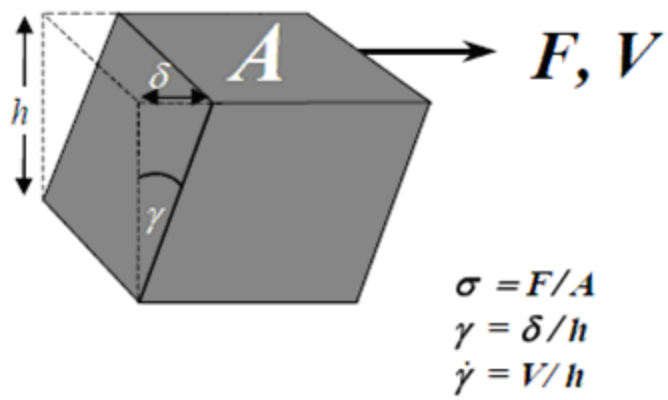


Figure 3-1. Definition diagram for shear flow. [adapted from Barnes, 2000]

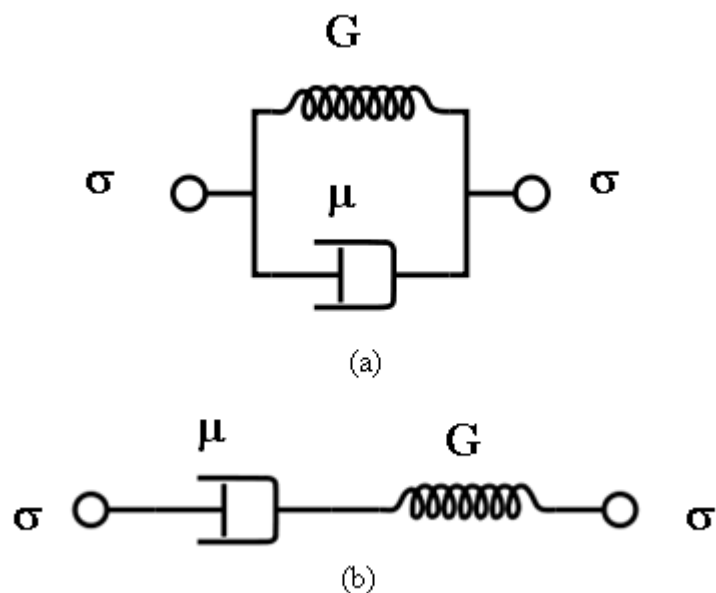


Figure 3-2. Mechanical analog for (a) Voigt model and (b) Maxwell model.

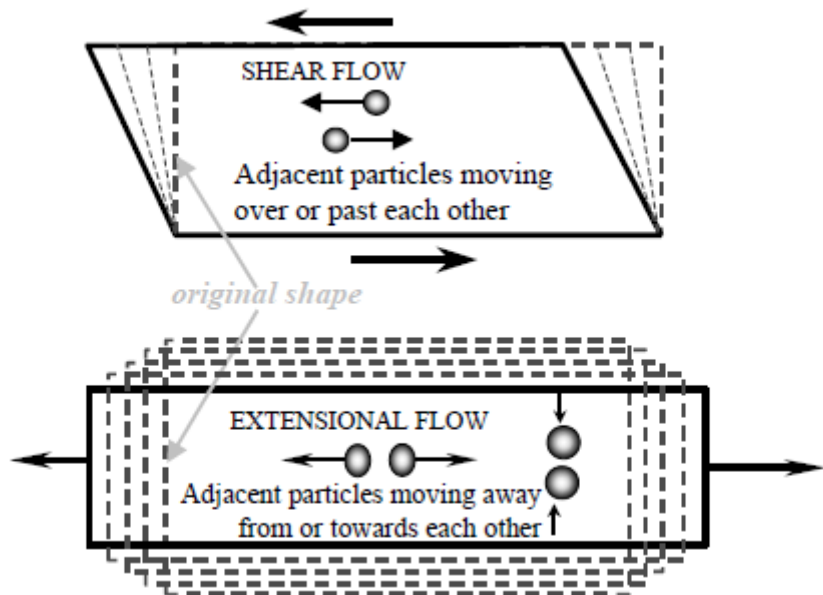


Figure 3-3. Particle motion related to orientation of external force. [Barnes, 2000]

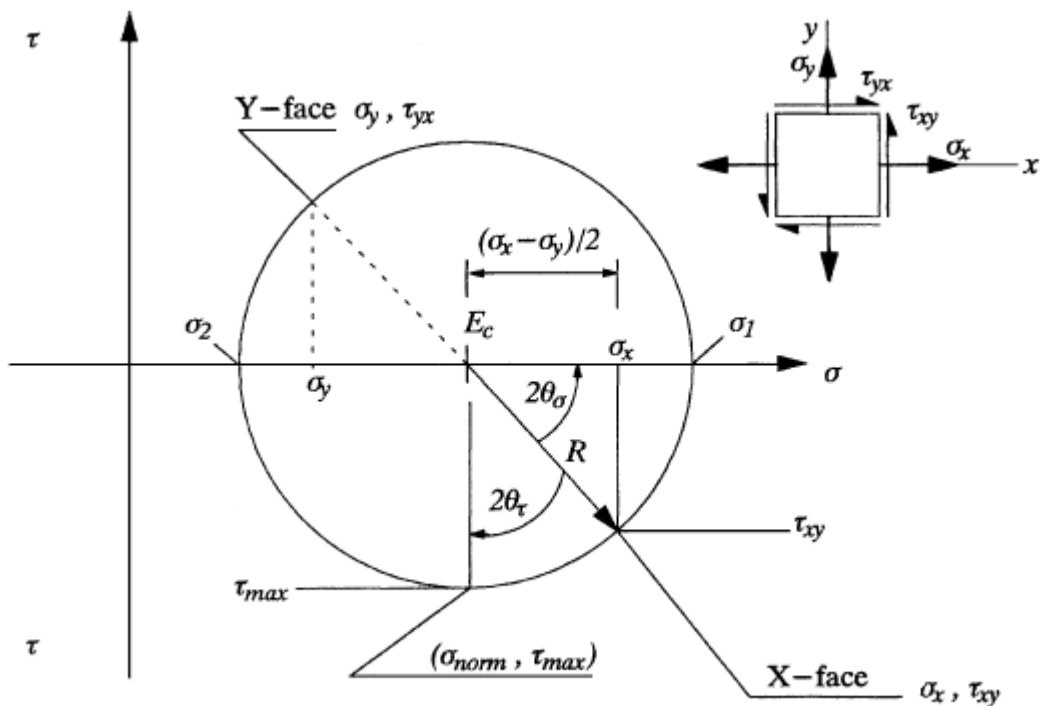


Figure 3-4. Mohr's circle representation of body stresses.

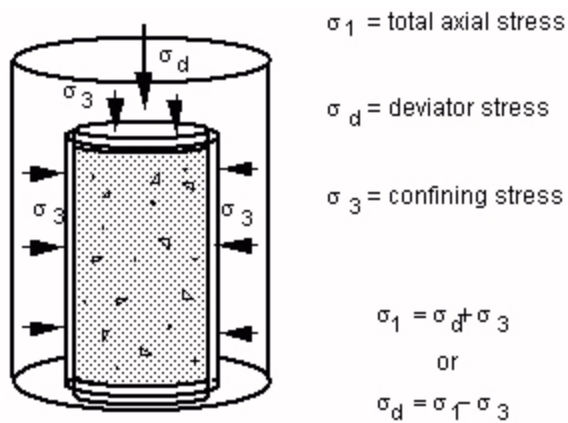


Figure 3-5. Diagram of triaxial test conditions.



Figure 3-6. TA Instruments AR 2000ex controlled stress/controlled strain rheometer.

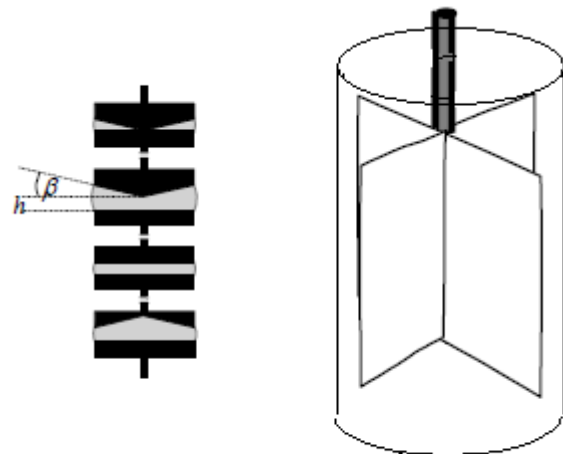


Figure 3-7. Cone and plate geometries and vane concentric cylinder geometry.

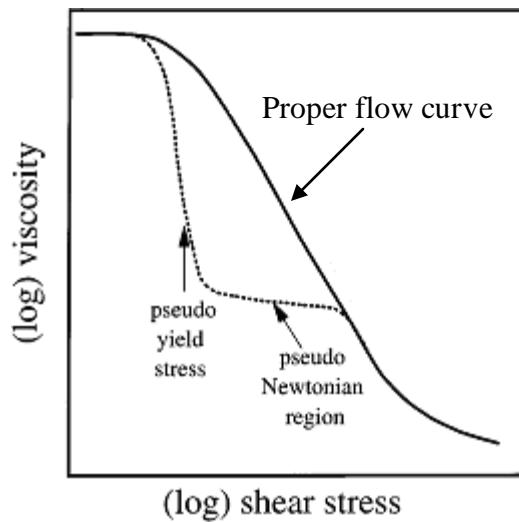


Figure 3-8. Effect of wall depletion on a complex liquid.

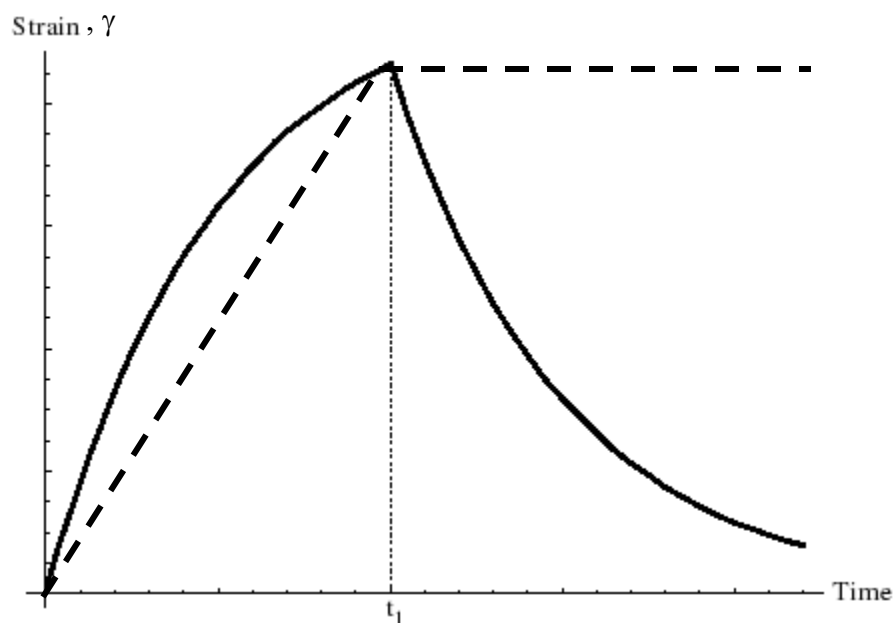
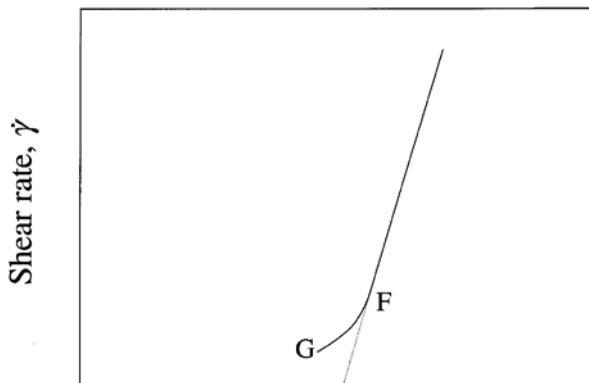


Figure 3-9. Strain responses during creep test. Solid line: Voigt model, Dashed line: Maxwell model.



Shear stress, σ
 Figure 3-10. Intercept with straight line law for defining yield stress. [Bingham, 1922]

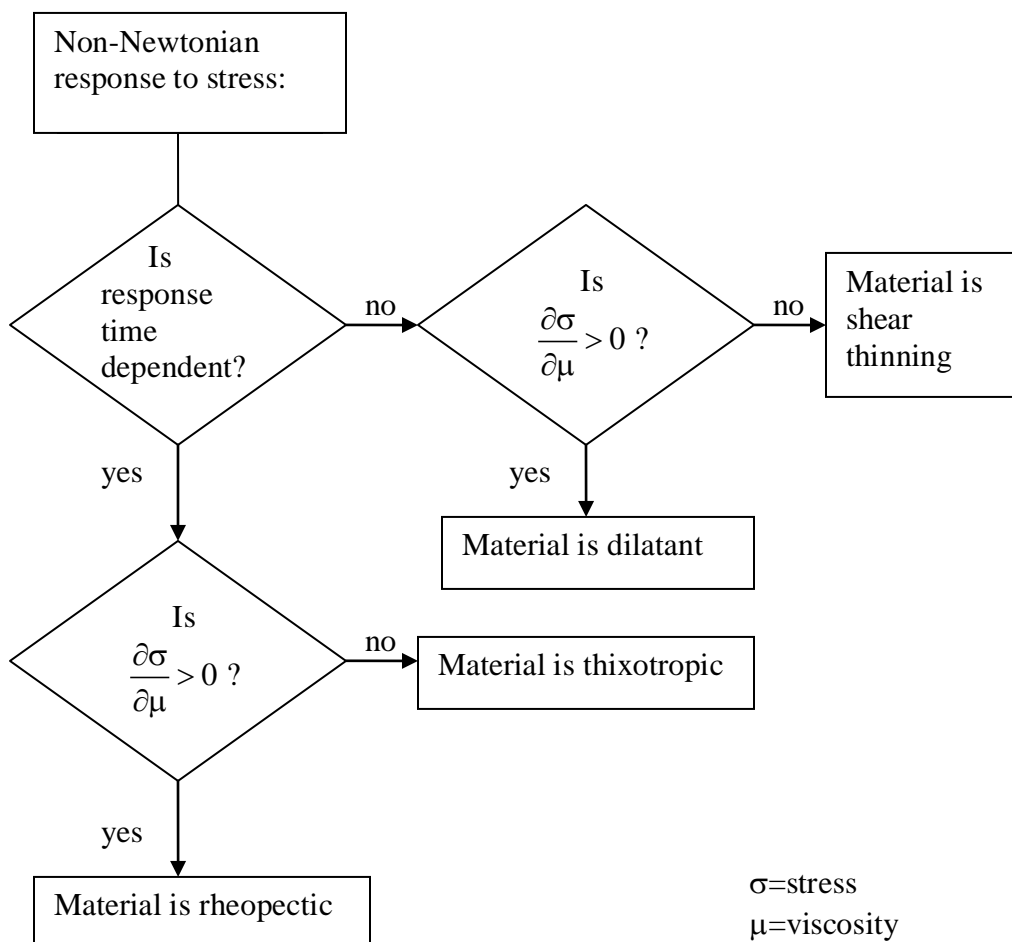


Figure 3-11. Material response to stress.

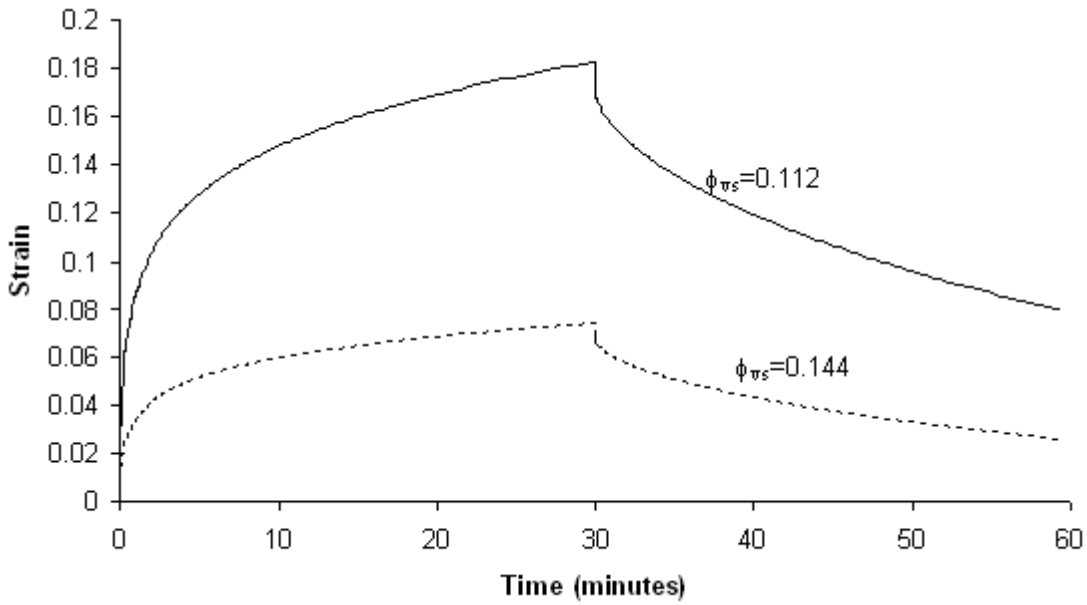


Figure 3-12. Creep curve for AD Mud: applied shear stress = 0.5 Pa.

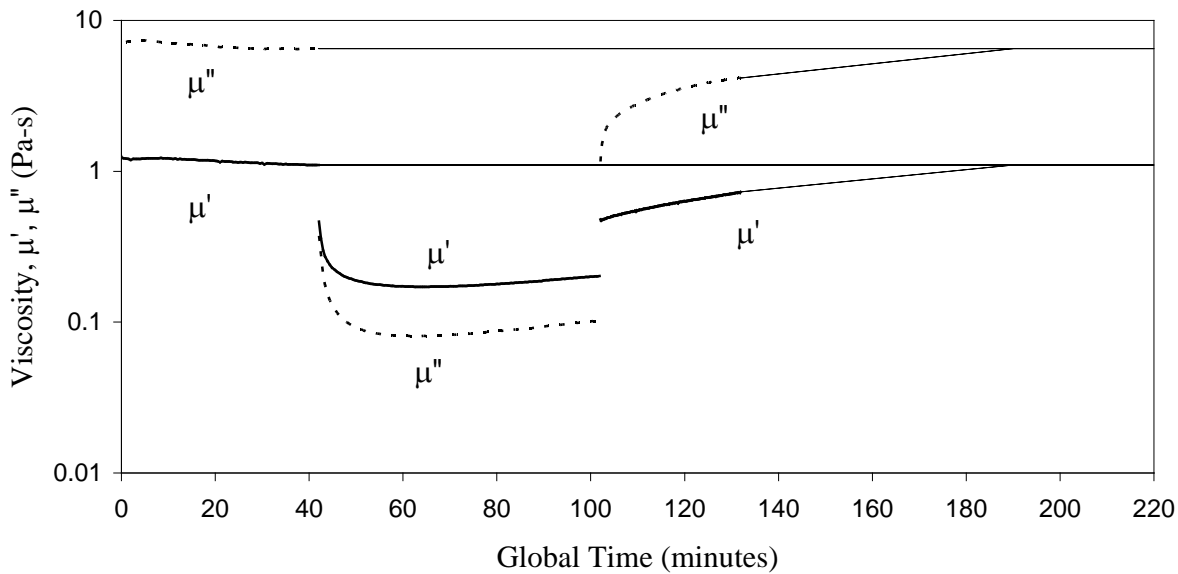


Figure 3-13. Continuous time series results depicting AD Mud response to Run 1 oscillatory shear stress protocol shown in Table 3-1.

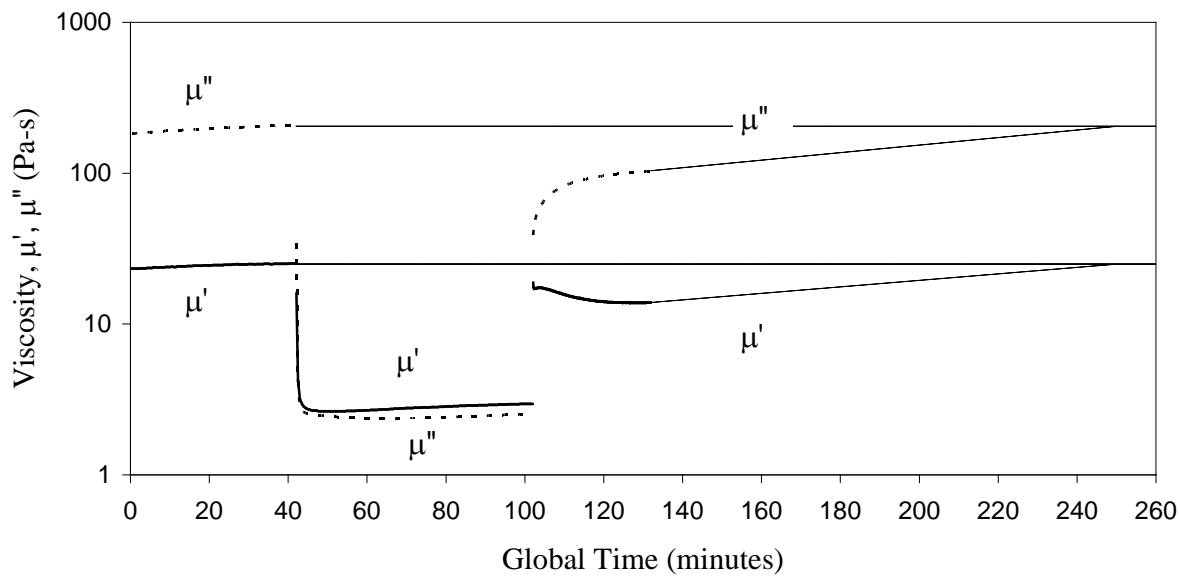


Figure 3-14. Continuous time series results depicting AD Mud response to Run 2 oscillatory shear stress protocol shown in Table 3-1.

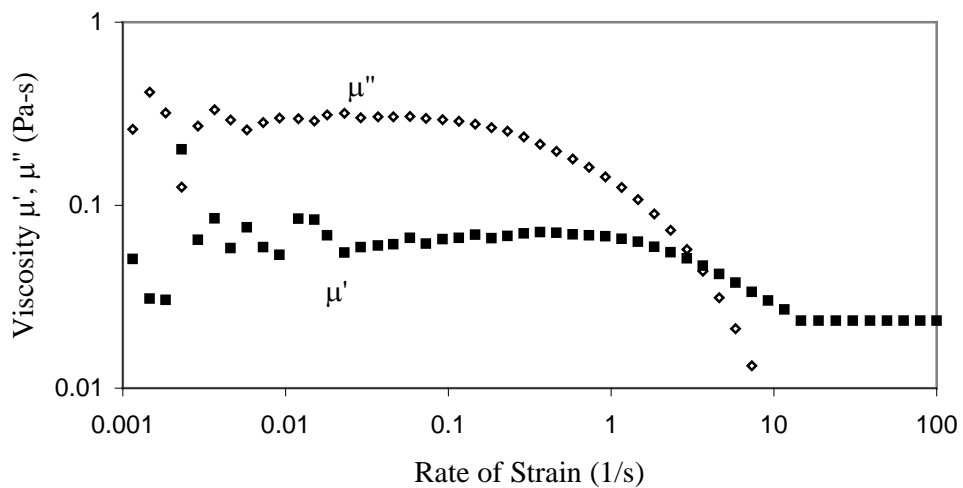


Figure 3-15. Flow response of AD Mud to Run 1F oscillatory strain sweep protocol shown in Table 3-2.

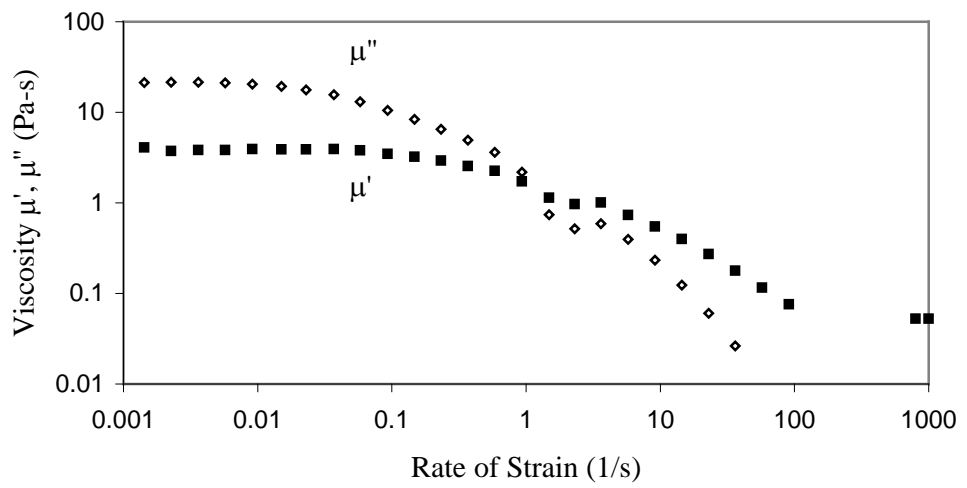


Figure 3-16. Flow response of AD Mud to Run 8F oscillatory strain sweep protocol shown in Table 3-2.

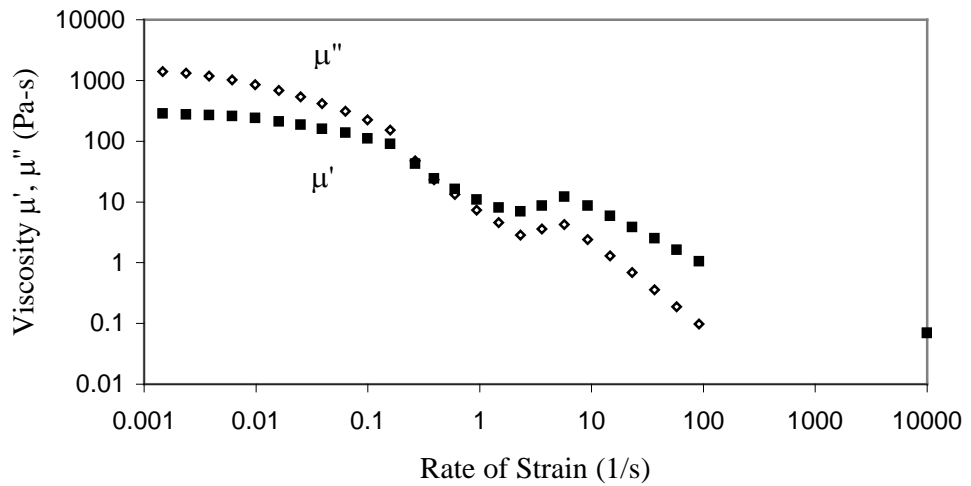


Figure 3-17. Flow response of AD Mud to Run 15F oscillatory strain sweep protocol shown in Table 3-2.

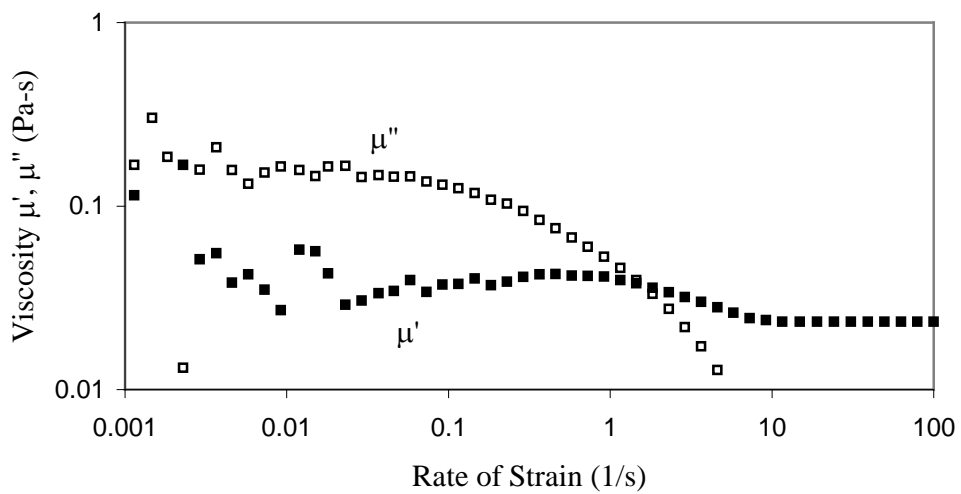


Figure 3-18. Flow response of AD Mud to Run 1B oscillatory strain sweep protocol shown in Table 3-2.

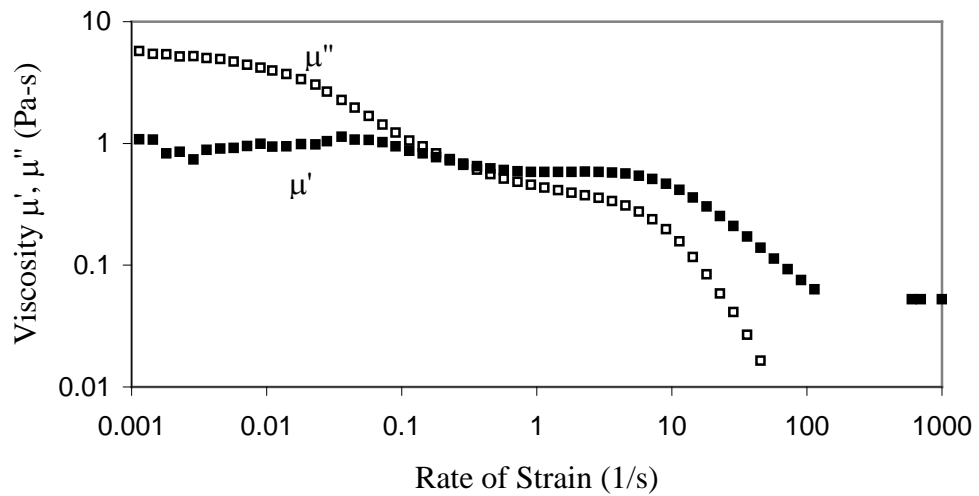


Figure 3-19. Flow response of AD Mud to Run 8B oscillatory strain sweep protocol shown in Table 3-2.

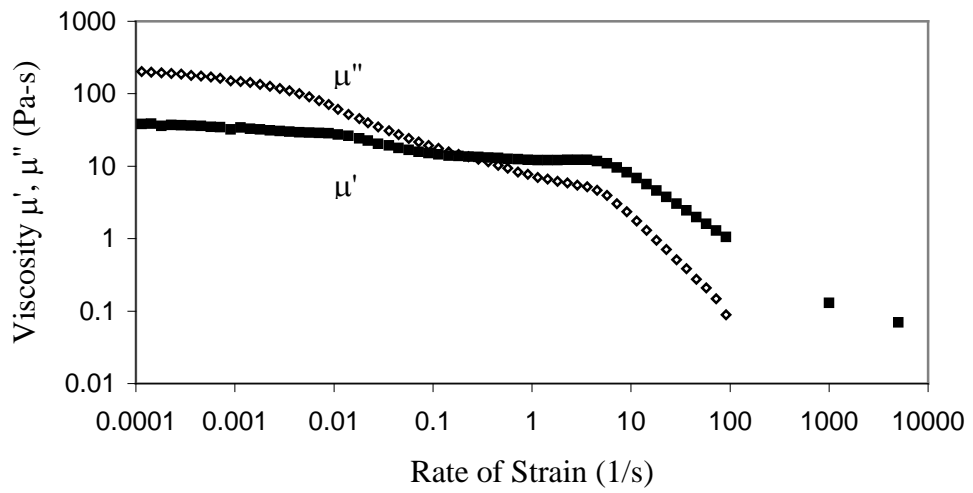


Figure 3-20. Flow response of AD Mud to Run 15B oscillatory strain sweep protocol shown in Table 3-2.

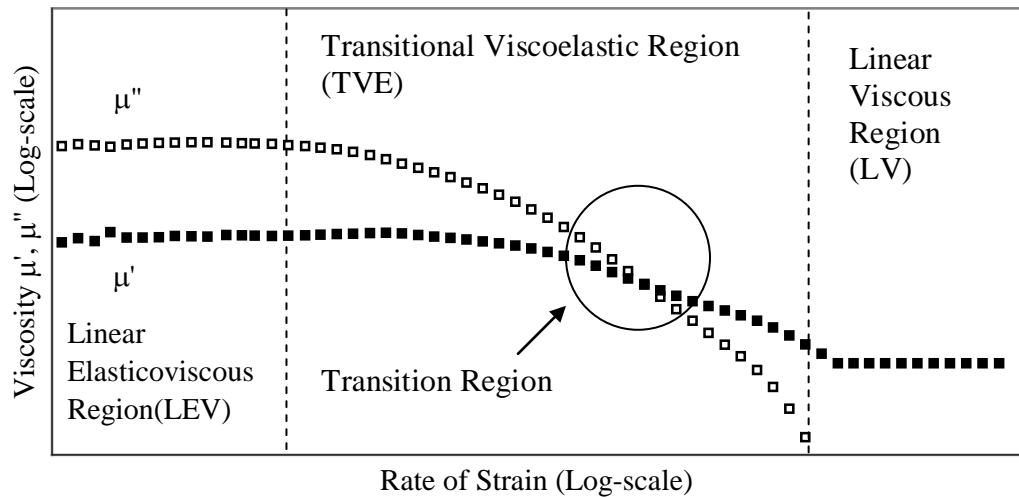


Figure 3-21. General flow response of AD Mud.

CHAPTER 4

CONSTITUTIVE MODEL

4.1 Introduction

From the results presented in Chapter 3, it is evident that the appropriate flow curve equation to relate shear stress and rate of strain for AD Mud must be non-linear due to its thixotropic properties. In this chapter, a non-linear equation of state will be derived to represent the response of the AD Mud bed over the range of strain rates expected as a result of wave forcing in the wave flume as well as in the marine environment.

4.2 Viscoelastic Equations

Some of the more common rheological equations are depicted in Figure 4-1 and will be discussed along with the assumptions underlying their formulations. Typically flow curve equations for non-Newtonian liquids are of two general types.

The first type recognizes the presence of a yield stress. The most common equation of this type is the Bingham model. This model and other popular variants are given in Equation 4-1.

$$\begin{aligned}
 \text{Bingham} \quad & \sigma = \sigma_0 + \mu_p \gamma^{\frac{1}{n}} \\
 \text{Casson} \quad & \sqrt{\sigma} = \sqrt{\sigma_0} + \sqrt{\mu_p} \gamma^{\frac{1}{n}} \\
 \text{Herschel - Bulkley} \quad & \sigma = \sigma_0 + k \gamma^{\frac{1}{n}}
 \end{aligned} \tag{4-1}$$

σ_0 is the yield stress, μ_p represents the plastic viscosity of the liquid and k and n are empirical constants representing the viscous and non-Newtonian properties of the liquid, respectively.

The second type of model does not recognize a yield stress. The equation for this type of model is often defined by a power law relationship between the shear stress and rate of strain (Equation 4-2). This model has been used to represent pseudoplastic material behavior.

$$\sigma = k \gamma^{\frac{1}{n}} \tag{4-2}$$

k and n are the same constant as in Equation 4-1 and represent the consistency of the liquid, (i.e. the more viscous the liquid, the higher the k value), and the degree of non-Newtonian behavior of the liquid, respectively. For $n=1$, the liquid is defined as Newtonian. The degree of departure of n from 1 indicates the magnitude of its non-Newtonian behavior. Since AD Mud is thixotropic, $n<1$. The power law (Equation 4-2) equation is limited because the shear stress-rate of strain relationship of saturated mud can not be adequately described by constant k and n values over the full range of shear stress and rate of strain.

More flexible flow curve models representing pseudoplastic material include those shown by Equation 4-3.

$$\begin{aligned}
 \text{Prandtl} \quad \sigma &= A \sin^{-1} \left(\frac{\gamma}{C} \right) \\
 \text{Cross} \quad \sigma &= \frac{(\mu_0 - \mu_\infty) \gamma}{\left(1 + k \gamma \right)} + \mu_\infty \gamma \\
 \text{Williamson} \quad \sigma &= \frac{A \gamma}{\left(B + \gamma \right)} + \mu_\infty \gamma
 \end{aligned} \tag{4-3}$$

A , B and C are constants for the particular material, μ_0 is the viscosity at zero rate of strain and μ_∞ is the viscosity at infinite rate of strain. With the added versatility of these flow curves, comes added complexity of applying them.

Due to the flow behavior of non-Newtonian liquids, all the above equations are defined empirically through fitting data to the appropriate curve. Many times, the appropriateness of a particular equation depends on the problem. For example, over a very small range of shear stress and rate of strain, almost all complex liquids can be represented by a simple linear Newtonian flow curve or a Bingham flow curve. However, the ranges of shear stress and rate of strain of a

process are often large enough that the liquid response is non-Newtonian and a non-linear flow curve is necessary to span the flow conditions. This is indeed the case for the range of strain rates in the seabed by the shear stress produced from shoaling water waves. Based on wave measurements collected at CSI3 by WAVCIS during Hurricane Lili in 2002, shear stress at the bed surface at this location can be in the range ($0 \leq \sigma \leq 10$ Pa) and strain rates in the top part of the mud bed can be in the range $\left(0 \leq \dot{\gamma} \leq 200 \text{ s}^{-1}\right)$. Any time the shear stress imposed on the bed results in transition of the bed, a non-linear model is necessary.

4.3 Thixotropy

As discussed in Chapter 3, AD Mud is a thixotropic, complex liquid and as such has flow characteristics which vary with time. From the oscillatory time series runs shown in Figures 3-13 and 3-14, the time it takes for the structure of AD Mud to *substantially* respond to a changed shear stress condition is on the order of minutes. In comparison to the time scales of changing sea state this response time is very short and will not be included in the derived flow curve for AD Mud.

However, since thixotropy does occur in AD Mud, consideration will be given for this effect by deriving flow curve equations based on the stress history. AD Mud responds differently to a shear stress depending on whether it was exposed to a mild or severe shear stress prior to imposition of a change in the shear stress. Bottom shear stress depends on the horizontal water velocity shown by Equation 4-4.

$$\sigma_b \propto u^2 \quad (4-4)$$

The terms ‘mild’ and ‘severe’ describing the stress history are quantified from the decision statement given by Equation 4-5.

$$\text{If } \overline{u_{-t}} > u_0 \rightarrow \text{'mild'}, \text{ If } \overline{u_{-t}} < u_0 \rightarrow \text{'severe'} \quad (4-5)$$

$\overline{u_{-t}}$ is the average horizontal water velocity at the bed during the time leading up to the wave condition of interest, and u_0 is the average horizontal water velocity at the bed at the time of the wave condition.

This stress history-dependent behavior is evidenced by the occurrence of a hysteresis loop when shear stress is plotted against increasing rate of strain and then against decreasing rate of strain (Figure 4-2). The decision as to whether the top or bottom flow curve would be appropriate for a given initial condition must be made by considering Equation 4-5. If the shear stress initial condition is more severe than the recent stress history, the top (forward) flow curve would appropriately represent the AD Mud flow response. If the shear stress initial condition of interest is milder than the recent stress history, the bottom (return) flow curve should be used.

The thixotropic properties of AD Mud are shown in Figures 4-3 to 4-9. The plots demonstrate qualitatively that thixotropic influence must be accounted for in the analysis of how this mud responds to shear stress. In reference to Figure 4-2, the area between the two curves is an indication of how much work is done, W , by the oscillatory shear stress per unit volume of material per unit time (Equation 4-6).

$$W \left(\frac{N \cdot m}{m^3 \cdot s} \right) = \int_0^{\infty} \sigma_f d\gamma - \int_0^{\infty} \sigma_r d\gamma \quad (4-6)$$

With σ_f =shear stress of forward flow curve, σ_r =shear stress of return flow curve.

The work expended in the AD Mud may be attributed primarily to breaking down the aggregate bond structures. The area of the hysteresis loop is most prominent with the high ϕ_{vs} samples represented by Run 5F/Run 5B and Run 15F/Run 15B (Figures 4-5 and 4-9) and least prominent with the lowest ϕ_{vs} samples represented by Run 1F/Run 1B and Run 11F/Run 11B

(Figures 4-3 and 4-7). Since the higher ϕ_{vs} samples contain denser structural bonds, the shear strength of these samples is greater and more energy is required to break down the mud. A quantitative discussion of this relationship between ϕ_{vs} and density of bonds was presented in Section 3.7.2.2. The inflection in the curves at a higher rate of strain is due to the influence duration has on the shear stress. At rest, the mud has the maximum bond density (i.e. # of intact bonds per unit contact area of adjacent aggregate particles) for that mud condition. As shear stress is imposed, the number of bonds available to be broken continues to decrease until the mud becomes a viscous liquid with no elastic structure. The rate of reformation of the structure under a relaxed shear stress condition will also increase with time at that condition for the same reason [Wilkinson, 1960]. This description is limited by the fact that the tests used to demonstrate this effect varies both with time and with the rate of strain.

Based on the above analysis, a new flow curve will be proposed in the general form of the Cross model (Equation 4-3), which is determined to most closely represent the characteristics of AD Mud.

4.4 AD Mud Flow Response Equation

The Cross model as well as the other noted flow equations require parameters that are typically obtained by curve fitting. The use of regressive methods to solve the flow equation causes a disconnection between the equation and the results represented by that equation. The AD Mud flow equation (based on the Cross model) will be presented in terms of material properties and thus curve fitting will be avoided.

4.4.1 Model Approach

The generalized flow response of AD Mud to oscillatory shear stress shown in Figure 3-21 can be represented in terms of the complex viscosity, μ^* , and phase angle, δ , due to the

orthogonal relationship between the viscosity components μ' and μ'' (Figure 4-10). The form of both curves is sigmoidal and can be defined based on the generalized logistic function and the complimentary logistic function depicted in Figure 4-11. The general logistic function equation is defined by Equation 4-7 [Gershenfeld, 1999].

$$f(x) = \frac{1}{1+e^{-x}} \quad (4-7)$$

with the complimentary function represented by $1-f(x)$.

This function is defined in terms of the asymptotic values at $x \rightarrow (\pm \infty)$, the coordinate values of the inflection point on the curve and the rate of closure to the asymptotic values. By defining the curve equations for μ^* and $\sin\delta$ as functions of rate of strain based Equation 4-7, the flow equation of AD Mud will be defined over the rates of strain plausible for sea wave conditions. Since the exponential nature of the logistic equation (Figure 4-11) is represented in linear scale, the adopted solution will be non-exponential because of the linear-log scale representation of the AD Mud data. The physical basis of the asymptotic values and the inflection point of the flow curve relate to the state of the AD Mud at those strain rates. As a result, the physics of mud behavior is preserved, which is a distinct advantage of this solution to those presented by Equation 4-3 which rely on curve fitting.

4.4.2 Model Derivation

The flow curve equations relating the complex viscosity, μ^* and the phase angle represented by $\sin\delta$, to rate of strain are given by Equations 4-8 and 4-9.

$$\left| \mu^*(\gamma) \right| = \frac{\mu'_{INF} \gamma + \mu'_{LEV} \gamma_{LIQ}}{\gamma + \gamma_{LIQ} \sin \delta_{LEV}} \quad (4-8)$$

$$\sin \delta(\gamma) = \frac{\gamma + \gamma_{LIQ} \sin \delta_{LEV}}{\gamma + \gamma_{LIQ} \sin \delta_\infty} = \frac{\gamma + \gamma_{LIQ} \sin \delta_{LEV}}{\gamma + \gamma_{LIQ}} \quad (4-9)$$

μ'_{∞} is the asymptotic viscosity at infinite rate of strain in the linear viscous (LV) region, μ'_{LEV} is the asymptotic real viscosity in the low rate of strain linear elasticoviscous (LEV) region, γ_{LIQ} is the rate of strain value at the inflection point of the complex viscosity curve and, δ_{LEV} is the asymptotic value of the phase angle in the low rate of strain LEV region.

The quantity γ_{LIQ} is a significant physical property of the AD Mud since it defines the rate of strain at which transition occurs. This important rate of strain value for the AD Mud defines the section of the curve where the mud transitions from a predominantly elastic liquid to a predominantly viscous liquid. At this point μ' and μ'' are equal, which implies that the structure of the liquid intact at lower rates of strain is failing and the mud structure continues to be compromised with the duration of exposure (thixotropic) to rates of strain at or above the transition rate of strain, γ_{LIQ} .

The orthogonal relationship of the viscosity components, μ' and μ'' allows them to be defined from the flow curve equations shown by Equations 4-10 and 4-11.

$$\mu'(\gamma) = |\mu^*| \sin \delta = \frac{\mu'_{\infty} \gamma + \mu'_{LEV} \gamma_{LIQ}}{\gamma + \gamma_{LIQ} \sin \delta_{\infty}} = \frac{\mu'_{\infty} \gamma + \mu'_{LEV} \gamma_{LIQ}}{\gamma + \gamma_{LIQ}} \quad (4-10)$$

$$\mu''(\gamma) = |\mu^*| \cos \delta = \sqrt{|\mu^*|^2 - \mu'^2} \quad (4-11)$$

Figures 4-12 to 4-25 demonstrate the effectiveness of Equations 4-10 and 4-11 to describe the relationship between the real and imaginary complex viscosity components and rate of strain for

AD Mud under a broad range of strain rates. With the viscosities defined, the flow equation relating shear stress to rate of strain follows from the definition given in Equation 3-34.

$$\sigma(\gamma) = |\mu^*| \gamma = \frac{\mu'_{\text{INF}} \gamma^2 + \mu'_{\text{LEV}} \gamma_{\text{LIQ}} \gamma}{\gamma + \gamma_{\text{LIQ}} \sin \delta_{\text{LEV}}} \quad (4-12)$$

Figures 4-26-4-39 demonstrate the effectiveness of Equation 4-12 to describe the relationship between shear stress and rate of strain for AD Mud under a broad range of stresses.

Table 4-1 and Table 4-2 define the AD Mud properties used in the flow curve equations for forward and reverse sweep tests, respectively.

4.4.3 Observations

A noticeable anomaly between the data and the flow curve equation occurred over the middle strain rates for most of the reverse sweep test runs and for the large solids volume fractions forward sweep test runs (Figures 4-14, 4-18, 4-20 to 4-25). This is a demonstration of wall depletion, which is most prevalent in the reverse sweep cases because the mud structure is initially in a broken down condition due to the initial high rates of strain. As a result, a depleted low viscosity layer forms against the outer wall of the rheometer cylinder and is not restored until the sample is under very low rates of strain at the end of the runs. High solids volume fraction samples are most influenced due to the greater concentration of structural bonds depleted along the outer wall. This condition could lead to erroneous conclusions if the data were accepted as a property of the material rather than an artifact of the experiment. For a review of the wall depletion effect, the reader is referred to Section 3.4.1.

Another noticeable attribute of these results is that the elastic (storage) viscosity component, μ'' , almost always recovers as the rate of strain decreases to a low level. However, the real (loss) viscosity component, μ' , often does not revert to the results predicted by the

equation. This result is consistent with the thixotropic properties of AD Mud. As demonstrated in Figures 4-3 to 4-9, the hysteresis effect persists through very low rates of strain and the loop does not close until the rate of strain is near zero.

At high rates of strain, the data show an abrupt transition to a viscous liquid as reflected by the linear steady state trend of μ' , once μ'' becomes trivial at high rates of strain. This anomaly is also likely to be an artifact of the rheometer. As the phase angle approaches $\pi/2$, the value of a purely viscous material, the rheometer is unable to measure the angle precisely under high oscillatory rates of strain because the mechanical components of the rheometer contribute inertia to the measurements. The AR 2000ex Rheometer enables the user to map the inertial effects of the motor and this mapping then compensates the measurements to filter out as much external inertia as possible. However, at high rates of shear, especially in oscillatory flow tests, the instrument is limited in its ability to compensate for inertia. As shown with the flow equation results (Equation 4-12) in Figures 4-26 to 4-39, this instrument artifact does not significantly influence the results but is recognized and discussed because of its presence.

4.4.4 Analysis of Results

Figures 4-26 to 4-39 show three identifiable phases of the shear stress condition expected to occur in the seabed. The first phase shows a Newtonian response of AD Mud at low rates of strain. The real and imaginary viscosity components in this range of shear stress are independent of the rate of strain. This response reflects a shear stress condition that is too weak to compromise the structural integrity of the mud and as a result, the response is predominantly elastic with a small phase angle indicating the presence of viscous liquid properties.

These first phase results also support the appropriateness of a non-yield stress model to describe AD Mud. Within the capabilities of the AR 2000ex Rheometer to measure small rates

of strain responses to shear stress, the linear relationship persists. This suggests that if a yield stress did exist, it would be trivial. This phase is likely to represent the near-bed surface response of AD Mud to mild wave forcing or the response of a deeper seabed under stronger wave forcing.

As the shear stress is increased, reflecting either a more severe wave condition and/or a shallower seabed, the rate of strain increases significantly over a short span of increasing shear stress. This is depicted by the plateau region where the shear stress is high enough to break the mud structure. As a result, the complex viscosity decreases rapidly in part due to the fall of the elastic (structural) viscosity component and in part due to thixotropy. The inflection point in the flow curve is commonly referred to as the gelation point or transition point and it marks the location when the bed transitions from predominantly elastic to predominantly viscous ($\mu' = \mu''$) response. This is an important value since it is one of the points which define the flow curve, and is the point in time when the bed begins to behave as a predominantly viscous suspension which can be transported by external forcing.

The final phase occurs under high shear stresses and is marked by the return to Newtonian response. This phase reflects the breakdown of the bed into its elemental aggregate structure and the mud behaves as a viscous liquid. The viscosity asymptotically approaches the value μ_{INF} and is independent of the shear stress.

Similar to the discussion on the low shear stress phase, the results inferred over this phase are valid only for the range of shear stress measured. The range of shear stresses in the rheometer tests were selected to ensure coverage of bed shear stresses expected to occur at the outer topset of the Atchafalaya River Delta.

4.5 AD Mud Dynamics

The objective of this section is to explain the significance of some of the measured properties of AD Mud presented in Chapter 2 and Chapter 3.

4.5.1 Aggregate Orders

Threshold solids volume fraction values of the mud are depicted in Figure 2-14 as vertical broken lines. These ϕ_{vs} thresholds in the upper portion of the mud occurring at $\phi_{vs}=0.055$ and $\phi_{vs}=0.13$ may be attributed to the aggregate structure of mud. Krone [1963] studied an array of estuarine sediments under laboratory conditions and demonstrated that several viscosity values can be measured from the same sediment suspension. Each viscosity was shown to relate to a specific ϕ_{vs} of that suspension.

As particles settle under quiescent or low shear stress conditions, the particles are attracted to one another through the polarity of the charge on their surface by van der Waal's forces. In addition to electrochemical cohesion, biopolymeric binding due to organic mucous surrounding the particle also may contribute significantly to aggregation [Wolanski, 2007]. Based on the low organic content of AD Mud, biopolymeric binding is not likely a significant contributor, and cohesion can be mainly attributed to the electrochemical effect.

4.5.2 Aggregate Densities

The governing relationship used by Krone was derived by A. Einstein and is shown as Equation 4-13.

$$\log\left(\frac{\mu_s}{\mu_w}\right) = 1 + 2.5\phi_{vf} \quad (4-13)$$

μ_s is the viscosity of a dilute suspension of inert, rigid spheres, μ_w is the viscosity of the liquid, and ϕ_{vf} is the fraction of the suspension volume occupied by the spheres (flocs). The factor 2.5

depends on the shape of the suspended particles and will be greater than 2.5 for shapes other than spheres [Krone, 1963]. The methodology of Krone will be employed to estimate the density of the 0th and 1st order aggregates of AD Mud.

Since ϕ_{vs} is a more easily measurable property of mud than ϕ_{vf} , the approach taken is to relate the density of an order of aggregate (floc), ρ_f , to ϕ_{vs} , using Equation 4-13. The relationship between viscosity and ϕ_{vs} was obtained from the analysis of AD Mud summarized in Table 4-2. It is important to note that the viscosity measured by Krone was obtained under continuous flow condition while the data for this study were obtained under oscillatory flow condition. Table 4-2 data were used instead of Table 4.1 in order to be consistent with the data by Krone who used a rotating cylinder viscometer and analyzed the data obtained only during the decreasing rpm condition.

Figure 4-40 presents the data for AD Mud in linear-log scale with the viscosity normalized by the viscosity of the pore water, $\mu_w = 1.2 \times 10^{-3}$ Pa·s. The normalized viscosities were computed using μ_{LEV} and μ_{INF} to represent the viscosity of the 1st order and 0th order aggregates of AD Mud, respectively. Krone termed these viscosities as those measured under low rpm and under high rpm, respectively. The results in Figure 4.40 demonstrate a linear-log relationship between the normalized viscosity and low solids volume fractions. The slope, k' , defines the relation between these two variables as shown in Equation 4-14.

$$\frac{\partial \left[\log \left(\frac{\mu}{\mu_w} \right) \right]}{\partial \phi_{vs}} = k' \quad (4-14)$$

The derivative of Equation 4-13 results in Equation 4-15.

$$\frac{\partial \left[\log \left(\frac{\mu}{\mu_w} \right) \right]}{\partial \phi_{vf}} = 2.5 \quad (4-15)$$

Equation 4-16 represents the relationship between ϕ_{vs} and ϕ_{vf} in terms of densities.

$$\frac{\phi_{vs}}{\phi_{vf}} = \frac{\rho_f - \rho_w}{\rho_s - \rho_w} \quad (4-16)$$

Floc density as a function of k' is presented by Equation 4-17.

$$\rho_f = \frac{2.5(\rho_s - \rho_w)}{k'} + \rho_w \quad (4-17)$$

One of the sediments evaluated by Krone was from the Gulfport Channel in Mississippi.

Due to its proximity to the Mississippi River, this sediment can be considered representative of the fine grained fraction of the discharge from the Mississippi River drainage basin. As mentioned previously, in 1963 a portion of the Mississippi River discharge was diverted to the Atchafalaya River. It is reasonable to consider that the sediment from the Gulfport Channel is similar in composition to the AD Mud. Table 4.3 compares the results obtained independently from this study and the study by *Krone* [1963] for the 0th and 1st order aggregates. Due to the high ϕ_{vs} samples tested during this study, aggregate orders higher than 1st order were not detected. The results of the two studies compare well.

The deviation from the linear trend at high ϕ_{vs} coincides with ϕ_{vs} of the 0th order aggregate (Figure 4-40). Solids volume fractions above the 0th order reflect aggregate structures that are denser. This slope change shown in Figure 4-40 by both data sets supports the importance of the 0th order aggregates since these aggregates are derived from the primary mineral particles.

This analysis offers an explanation of the results obtained in the settling column tests presented in Chapter 2. The 0th and 1st order aggregate densities in Table 4-3 compare well with

the respective threshold values in Figure 2-14. It shows that the 1st order aggregates have lower solids volume fraction and are weaker than the 0th order aggregates. Under quiescent settling, the higher order aggregates collapse under self-weight to 0th order except for a thin layer at the bed surface which does not experience overburden. Since the 0th order aggregates are stronger, they can withstand overburden down to a limiting depth. Below this depth, increased overburden causes re-orientation of the 0th order aggregate structure to form a more efficient arrangement which results in further de-watering of the bed.

Table 4-3 shows a slight disparity in the values of shear strengths of the aggregate orders between the two studies. This may be due to the different approaches used to define the shear strength of the aggregates and the ability to accurately measure the shear strength with the instrumentation available to Krone who assumed the Bingham model. With the improved accuracy and precision of the present instrument, more refined measurements are obtained. Determination of the shear strength is essential because it defines the threshold at which the bed changes from an elastic material to viscous liquid. This transition point will be discussed in Section 4.5.3.

4.5.3 Shear Strength

Based on Equation 4-12, the shear strength σ_{LIQ} is given by Equation 4-18.

$$\sigma_{LIQ} = \frac{(\mu'_{INF} + \mu'_{LEV})}{1 + \sin \delta_{LEV}} \gamma_{LIQ} \quad (4-18)$$

Figures 4-41 and 4-42 show the weak dependence of σ_{LIQ} on the angular frequency, ω , and on the stress history of the bed material. The test range of ω [0.628-5.0 rad/s] represents the typical range of water waves. Over this range, σ_{LIQ} will be considered independent of ω . This

consideration is validated by Figure 4-44, which shows the angular frequency run data falling within a narrow range as a function of ϕ_{vs} .

Figure 4-43 shows that σ_{LIQ} has two linear relationships with ϕ_{vs} in log-log coordinates over the range of ϕ_{vs} measured. Independent of shear stress history, one relationship exists over the range $[0.054 \leq \phi_{vs} \leq 0.132]$, and the other over the range $[0.132 < \phi_{vs} \leq 0.214]$. The general relationship of each linear section is defined by Equation 4-19.

$$\sigma_{LIQ} = A\phi_{vs}^n \quad (4-19)$$

The relevance of the solids volume fraction at the point of slope change, $\phi_{vs}=0.132$, is that it is the solids volume fraction of the 0th order aggregates. AD Mud samples show a noticeable increase in strength at concentrations greater than this value. Table 4-4 provides the coefficient values for the two linear sections shown in Figure 4-43.

The coefficient, A, may be considered a measure of the energy required to break down a unit volume of aggregate and has the units of Pa (Krone, 1963). ‘A’ depends on the bonds which connect adjacent primary particle aggregates and by the structure of the aggregate at the failure point. At low order of aggregation, ϕ_{vs} is high, which results in crowded adjacent particles making contact along a large area. This connection results in a greater σ_{LIQ} compared to a higher order of aggregation where ϕ_{vs} and the contact area are smaller.

The variable ‘n’ may be considered a measure of the unit strength of the bonds forming the aggregate. A large n value would imply high unit strength of bond. This high strength contributes to the non-linear increase in σ_{LIQ} when ϕ_{vs} is greater than that of the 0th order aggregate. At the transition point, complete rupture of connection occurs between adjacent

particles. This process takes time (thixotropy) and once it begins, the bonds in proximity to the failure point experience increased shear stress causing a rapid fall in the aggregate order.

The parameters μ'_{INF} , μ'_{LEV} , $\sin \delta_{\text{LEV}}$ and γ_{LIQ} show non-linear relationships as functions of ϕ_{vs} and ω . Appendix A presents these relationships as well as contour plots of μ'_{INF} , μ'_{LEV} and γ_{LIQ} which depend on ϕ_{vs} and ω . The δ values are relatively constant for each pre-stress history case and can be approximated by $\sin \delta_{\text{LEV}} = 0.18$ for mild pre-stress history and $\sin \delta_{\text{LEV}} = 0.30$ for severe pre-stress history. From the information provided in Appendix A, it is possible to derive the flow curve equations, Equations 4-8 to 4-12, for AD Mud within the solids volume fraction range of [0.054-0.214].

Equation 4-12 is the basis for development of a model to predict the attenuation ability of AD Mud and prediction of whether the oscillatory forcing is strong enough to liquefy the upper portion of the seabed (and if so to what depth transition would occur and to what depth bed motion could be predicted). This model derivation will be presented in Chapter 5.

Figure 4-44 presents a sketch summarizing the findings with respect to the effects of γ , and ϕ_{vs} on the state of mud. When an AD Mud bed is exposed to strong shear force it is likely to experience all of the states simultaneously depending on depth within the bed.

Table 4-1. AD Mud properties – oscillatory test results of flow curve variables [Forward Shear Rate Sweeps (simulating “pre-storm” condition)].

Angular Frequency ω (rad/s)	Run #	Solids Volume Fraction , ϕ_{vs}				
		0.0543 1F	0.112 2F	0.125 3F	0.144 4F	0.214 5F
5	$\mu'_{inf} = (Pa \cdot s)$	0.234	0.065	0.080	0.10	0.18
	$\mu'_{lev} = (Pa \cdot s)$	0.075	0.943	1.44	3.0	30
	$\sin \delta_{lev} =$	0.16	0.1489	0.134	0.135	0.132
	$\gamma_{liq}^{\square} = (s^{-1})$	2.25	2.25	2.2	2.2	2.5
1.57	Run #	6F	7F	8F	9F	10F
	$\mu'_{inf} = (Pa \cdot s)$	0.017	0.045	0.0525	0.0675	0.11
	$\mu'_{lev} = (Pa \cdot s)$	0.21	2.8	3.9	8.8	115
	$\sin \delta_{lev} =$	0.2	0.18	0.18	0.175	0.17
	$\gamma_{liq}^{\square} = (s^{-1})$	0.9	1	1	1	0.95
0.628	Run #	11F	12F	13F	14F	15F
	$\mu'_{inf} = (Pa \cdot s)$	0.010	0.03	0.035	0.044	0.07
	$\mu'_{lev} = (Pa \cdot s)$	0.56	8.6	11.55	25	285
	$\sin \delta_{lev} =$	0.26	0.2	0.195	0.195	0.2
	$\gamma_{liq}^{\square} = (s^{-1})$	0.4	0.3	0.35	0.3	0.35

Table 4-2. AD Mud properties – oscillatory test results of flow curve variables [Reverse Shear Rate Sweeps (simulating “post-storm” condition)].

Angular Frequency ω (rad/s)	Run #	Solids Volume Fraction , ϕ_{vs}				
		0.0543 1B	0.112 2B	0.125 3B	0.144 4B	0.214 5B
5	$\mu'_{inf} = (Pa \cdot s)$	0.0234	0.065	0.080	0.102	0.18
	$\mu'_{lev} = (Pa \cdot s)$	0.055	0.6	0.9	1.8	10
	$\sin \delta_{lev} =$	0.30	0.32	0.30	0.28	0.30
	$\gamma_{liq}^{\square} = (s^{-1})$	1.65	3.0	3.2	3.6	7.0
1.57	Run #	6B	7B	8B	9B	10B
	$\mu'_{inf} = (Pa \cdot s)$	0.017	0.045	0.0525	0.0675	0.11
	$\mu'_{lev} = (Pa \cdot s)$	0.16	1.8	2.5	4.7	25
	$\sin \delta_{lev} =$	0.26	0.35	0.38	0.38	0.25
0.628	$\gamma_{liq}^{\square} = (s^{-1})$	1.0	1.8	1.9	2.1	4.0
	Run #	11B	12B	13B	14B	15B
	$\mu'_{inf} = (Pa \cdot s)$	0.010	0.03	0.035	0.044	0.07
	$\mu'_{lev} = (Pa \cdot s)$	0.56	4.0	4.9	8.5	40
	$\sin \delta_{lev} =$	0.26	0.4	0.38	0.35	0.25
	$\gamma_{liq}^{\square} = (s^{-1})$	0.45	1.1	1.1	1.4	2.6

Table 4-3. Comparison of results – density of AD Mud aggregates (Gulfport Channel data obtained from *Krone*, [1963]) (* Shear strength measured under continuous flow conditions, ** shear strength measured under oscillatory flow conditions).

Sediment Sample	Order of Aggregation	Slope k'	ϕ_{vs}	ρ_f (kg/m ³)	Shear Strength (Pa)
Gulfport Channel (1963)	0	18.18	0.121	1,205	4.6*
	1	39.57	0.058	1,106	0.7*
Atchafalaya River Delta – outer topset (2008)	0	17.54	0.136	1,228	4.93 **
	1	39.10	0.056	1,103	0.18 **

Table 4-4. Eq. 4-19 Coefficients for AD Mud.

ϕ_{vs} Range	A ($\frac{N \cdot m}{m^3}$)	n
[0.054-0.132]	9,094	3.77
[0.132-0.214]	687,038	5.92

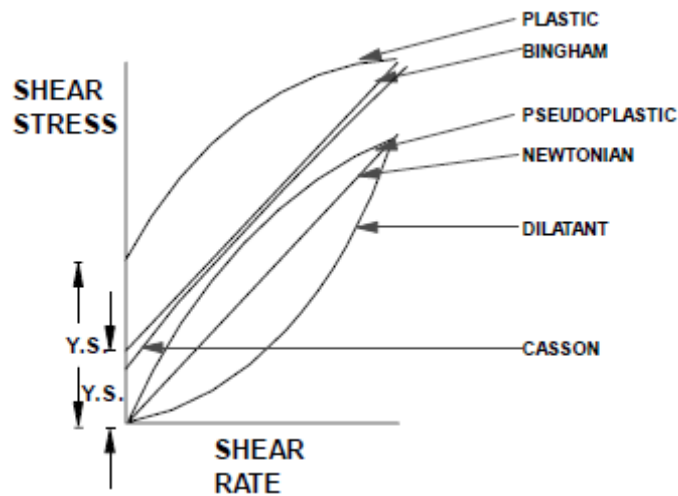


Figure 4-1. Flow curves represented by models.

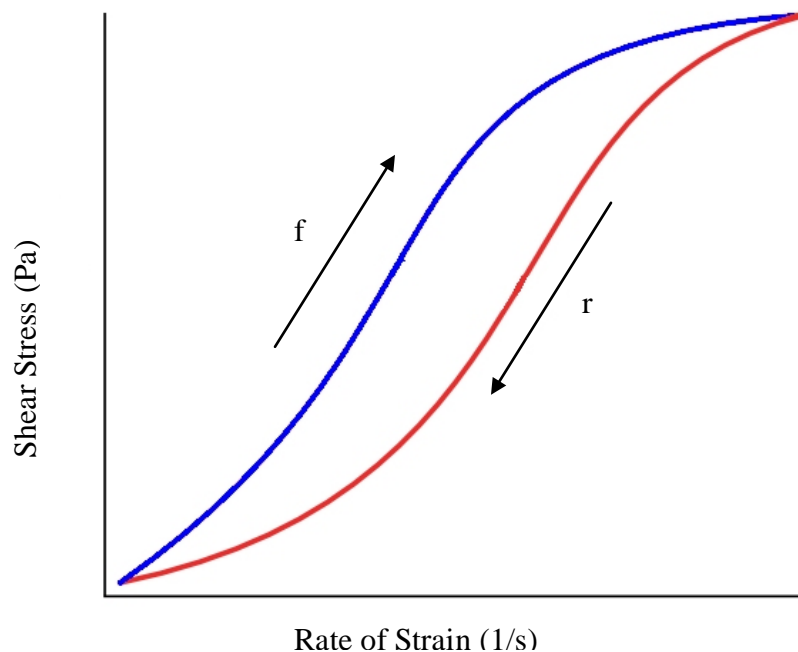


Figure 4-2. Hysteresis effect. f – forward flow curve, r – return flow curve.

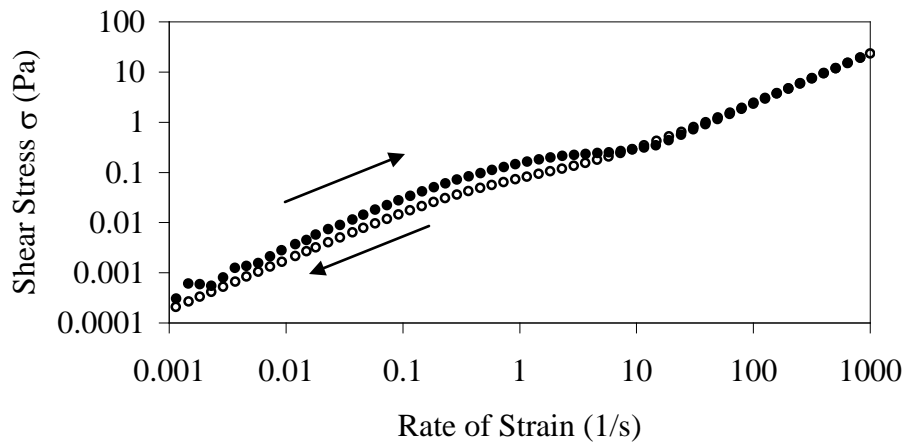


Figure 4-3. Continuous ramp up rate of strain followed by continuous ramp down rate of strain under Run 1F/Run 1B test conditions. Arrows indicate curve associated with ramp condition.

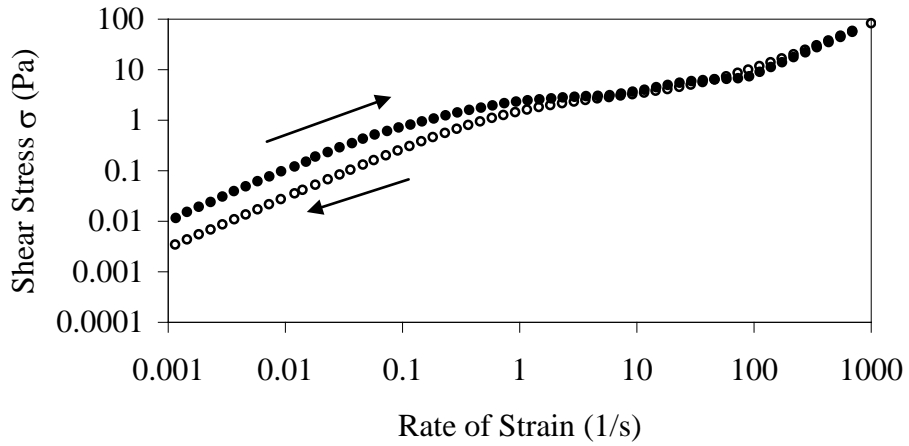


Figure 4-4. Continuous ramp up rate of strain followed by continuous ramp down rate of strain under Run 3F/Run 3B test conditions. Arrows indicate curve associated with ramp condition.

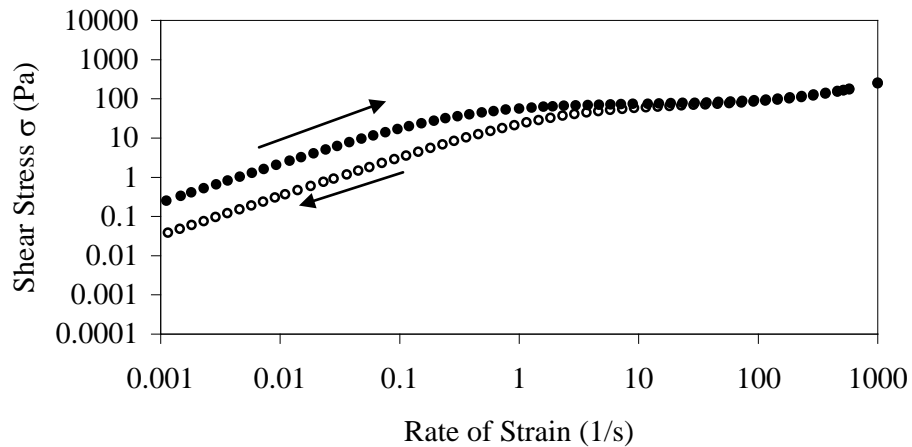


Figure 4-5. Continuous ramp up rate of strain followed by continuous ramp down rate of strain under Run 5F/Run 5B test conditions. Arrows indicate curve associated with ramp condition.

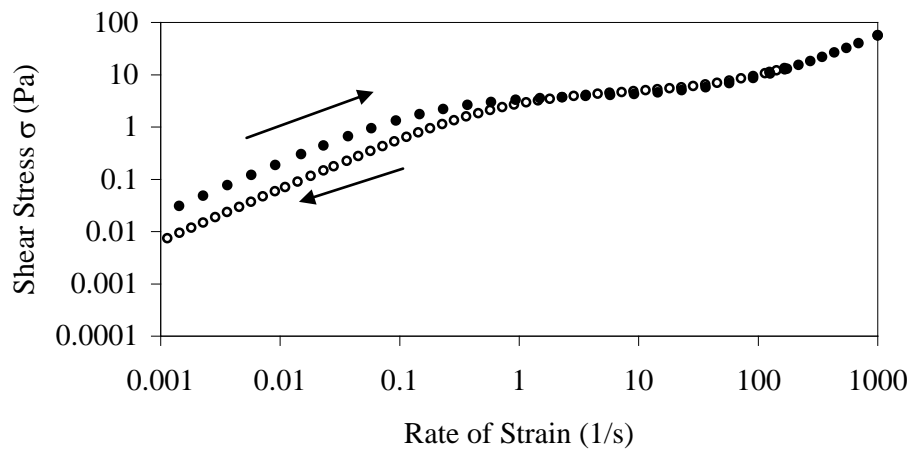


Figure 4-6. Continuous ramp up rate of strain followed by continuous ramp down rate of strain under Run 8F/Run 8B test conditions. Arrows indicate curve associated with ramp condition.

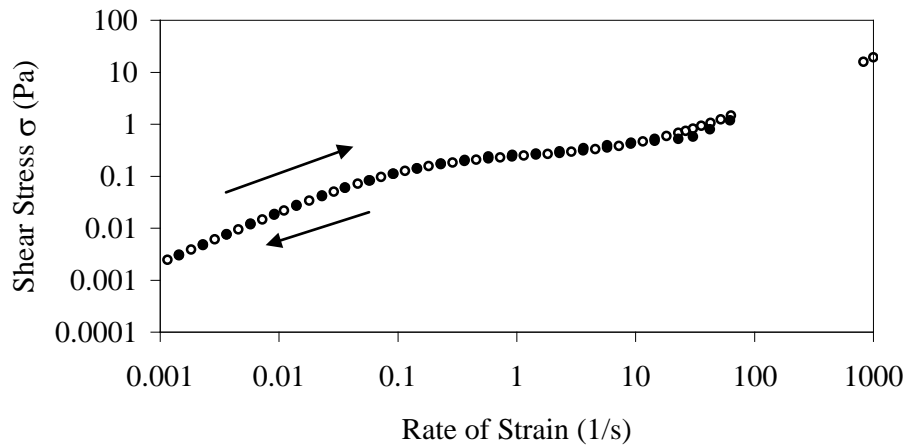


Figure 4-7. Continuous ramp up rate of strain followed by continuous ramp down rate of strain under Run 11F/Run 11B test conditions. Arrows indicate curve associated with ramp condition.

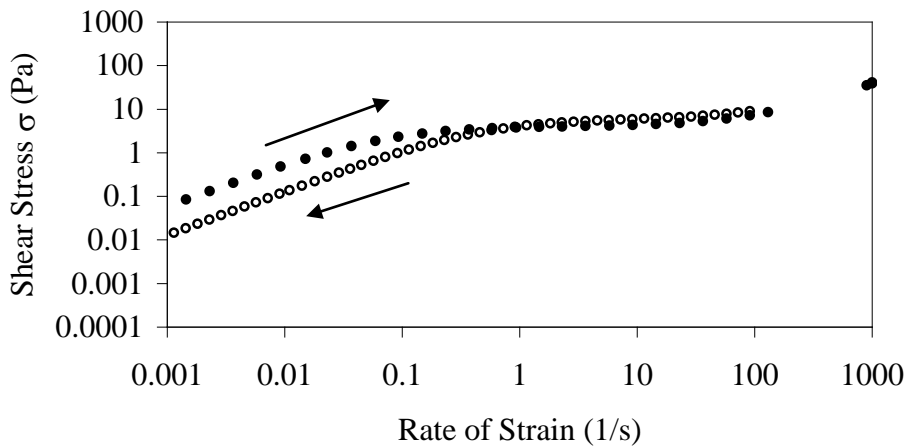


Figure 4-8. Continuous ramp up rate of strain followed by continuous ramp down rate of strain under Run 13F/Run 13B test conditions. Arrows indicate curve associated with ramp condition.

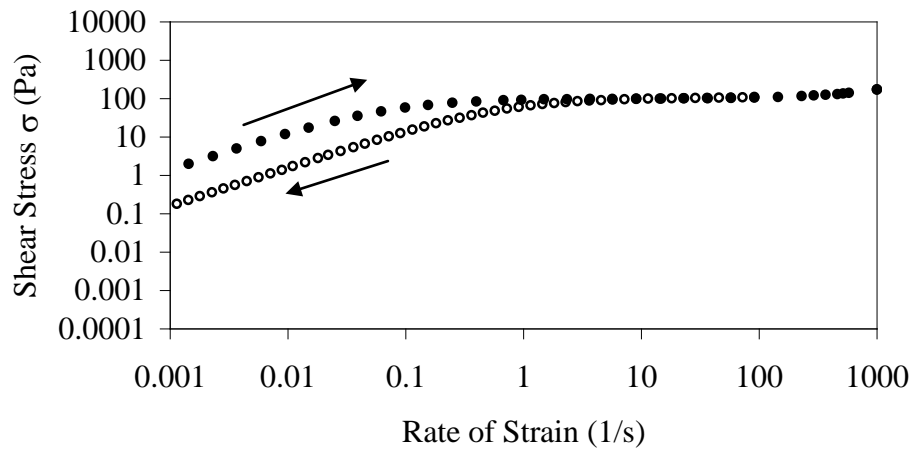


Figure 4-9. Continuous ramp up rate of strain followed by continuous ramp down rate of strain under Run 15F/Run 15B test conditions. Arrows indicate curve associated with ramp condition.

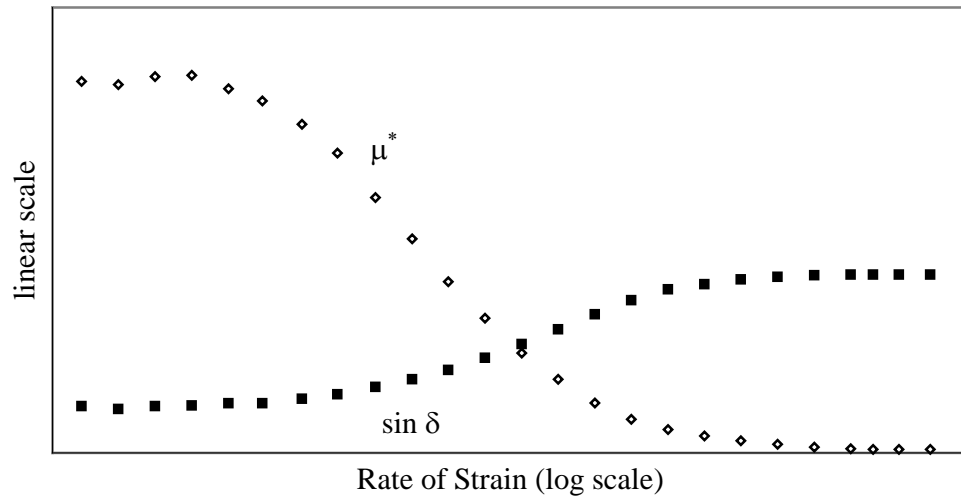


Figure 4-10. Generalized flow response of AD Mud in terms of μ^* and phase angle, $\sin \delta$.

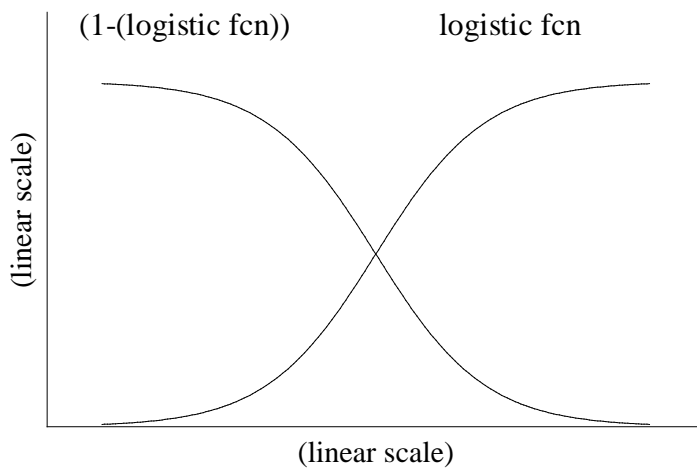


Figure 4-11. Generalized logistic function form and complementary logistic function form.

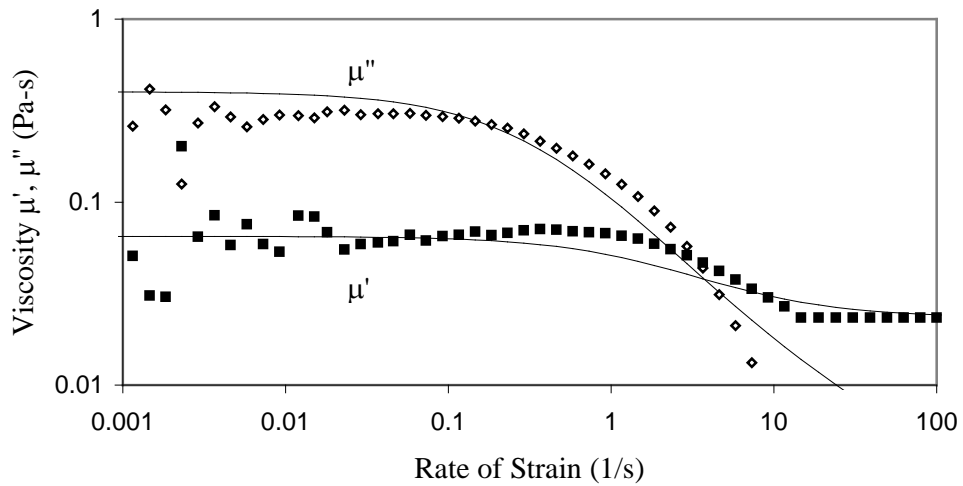


Figure 4-12. Measured oscillatory strain sweep results compared to flow curve results – Run 1F.

Figure 4-13. Measured oscillatory strain sweep results compared to flow curve results – Run 3F.

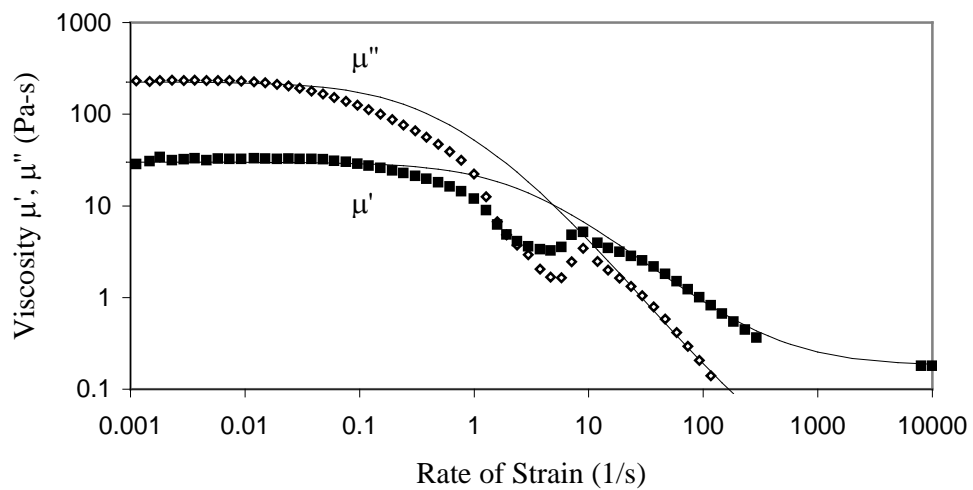


Figure 4-14. Measured oscillatory strain sweep results compared to flow curve results – Run 5F.

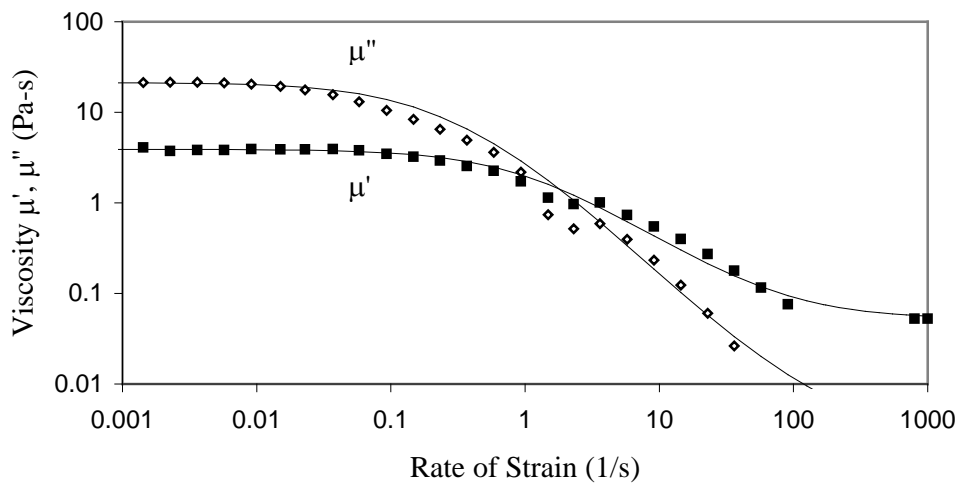


Figure 4-15. Measured oscillatory strain sweep results compared to flow curve results – Run 8F.

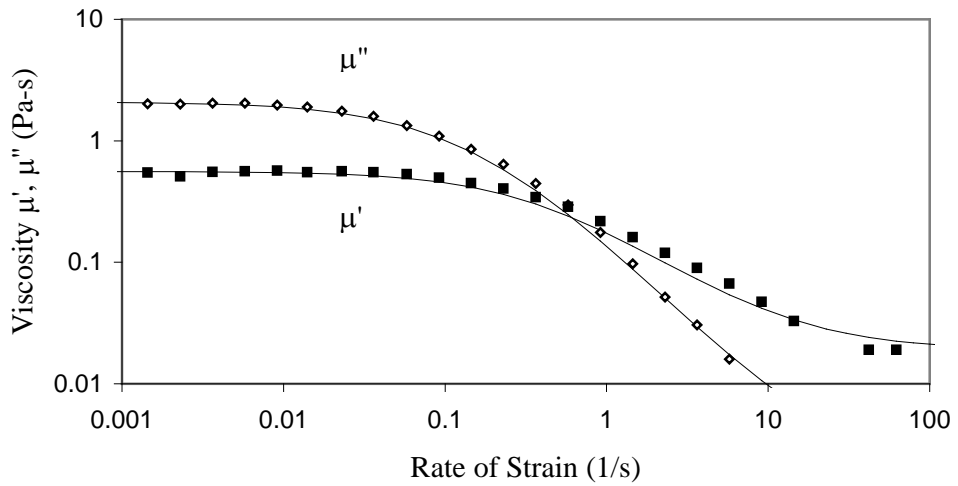


Figure 4-16. Measured oscillatory strain sweep results compared to flow curve results – Run 11F.

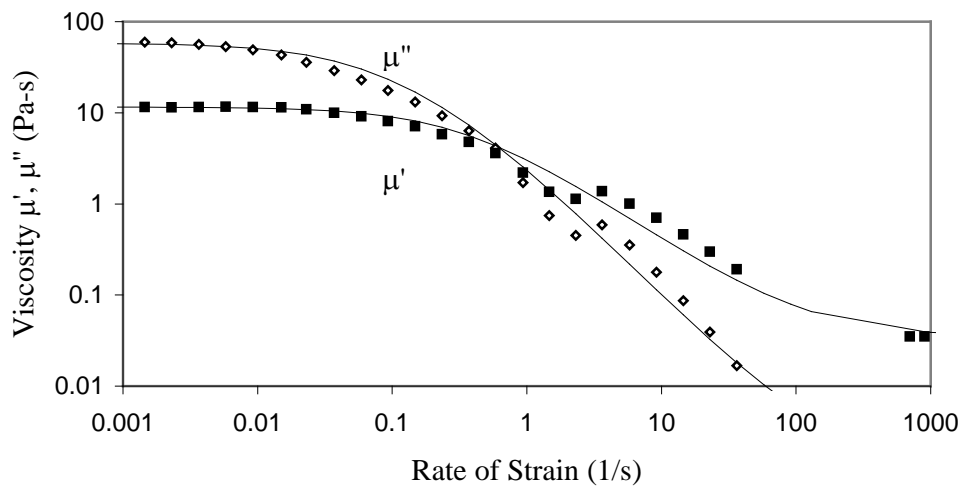


Figure 4-17. Measured oscillatory strain sweep results compared to flow curve results – Run 13F.

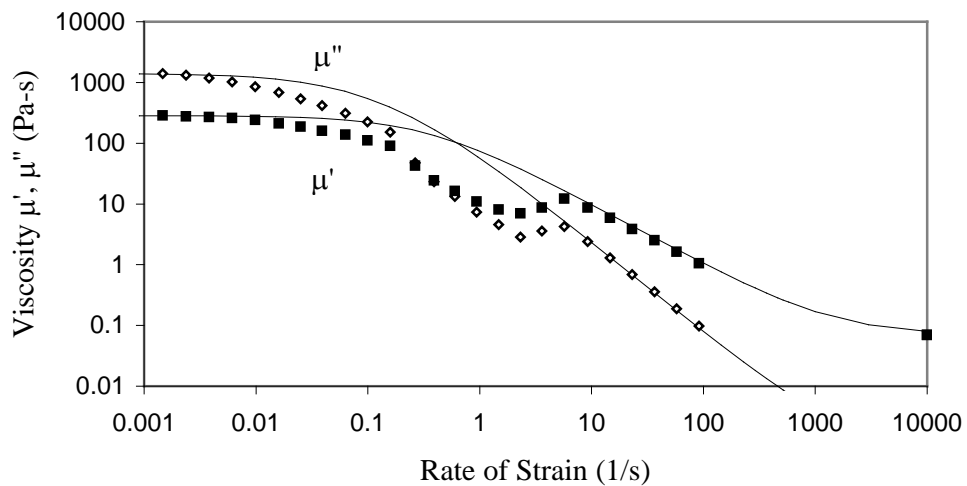


Figure 4-18. Measured oscillatory strain sweep results compared to flow curve results – Run 15F.

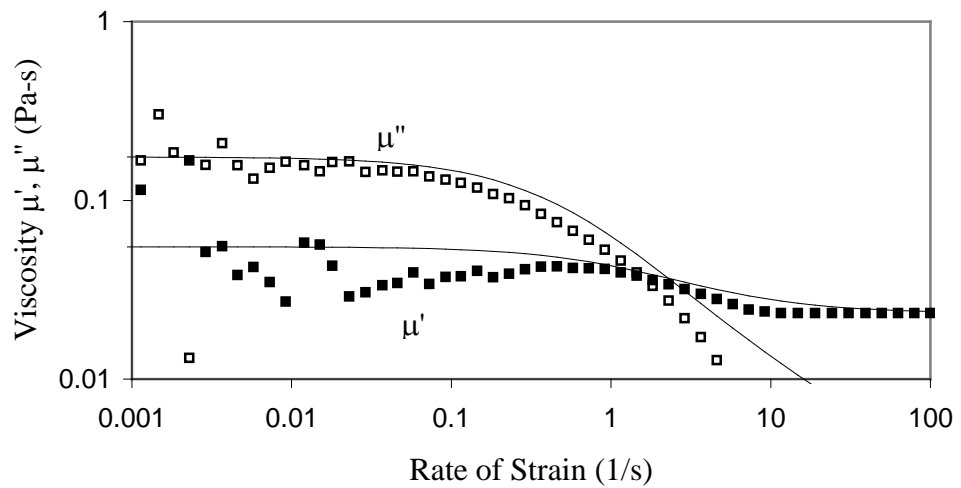


Figure 4-19. Measured oscillatory strain sweep results compared to flow curve results – Run 1B.

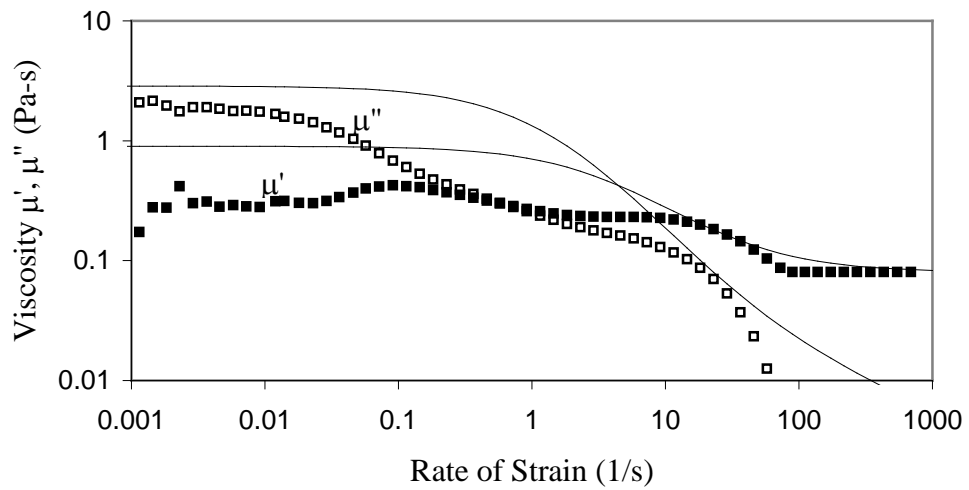


Figure 4-20. Measured oscillatory strain sweep results compared to flow curve results – Run 3B.

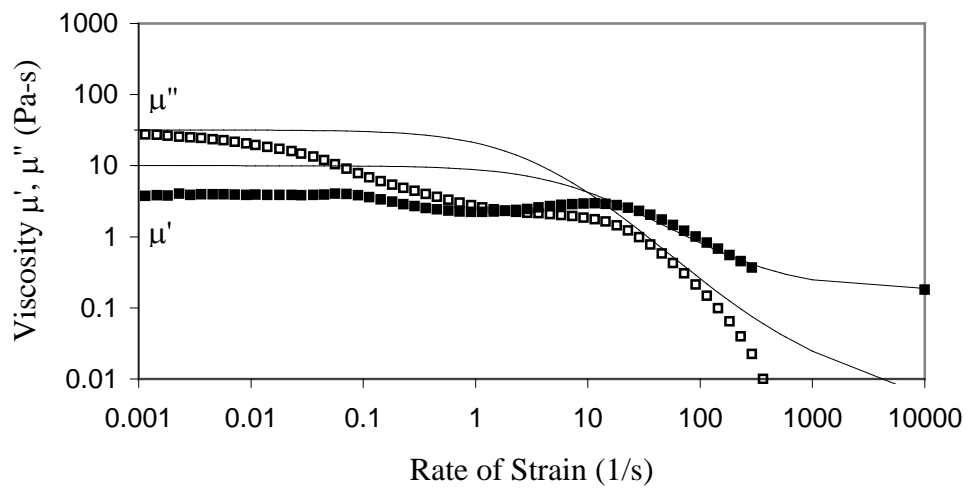


Figure 4-21. Measured oscillatory strain sweep results compared to flow curve results – Run 5B.

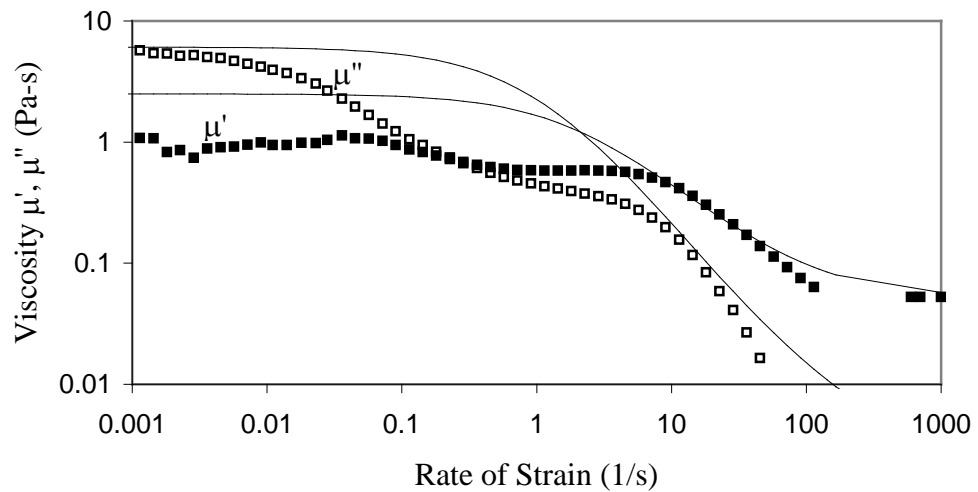


Figure 4-22. Measured oscillatory strain sweep results compared to flow curve results – Run 8B.

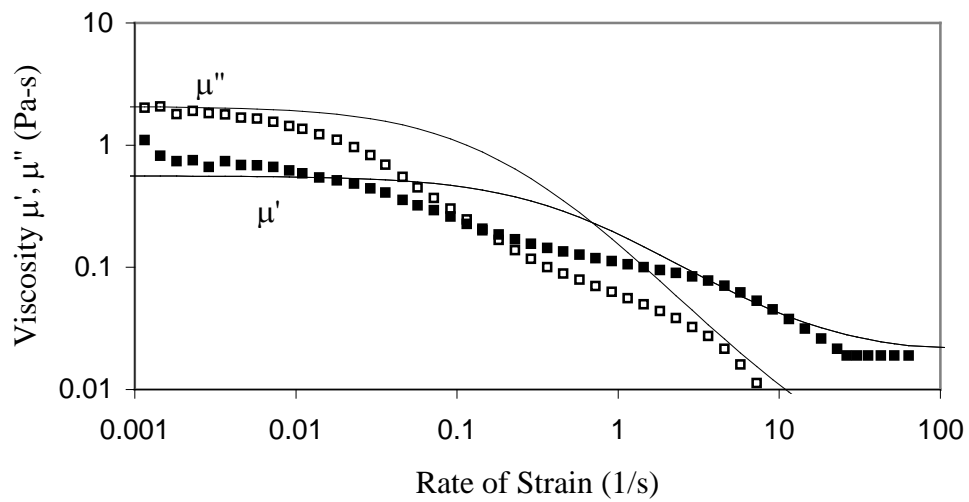


Figure 4-23. Measured oscillatory strain sweep results compared to flow curve results – Run 11B.

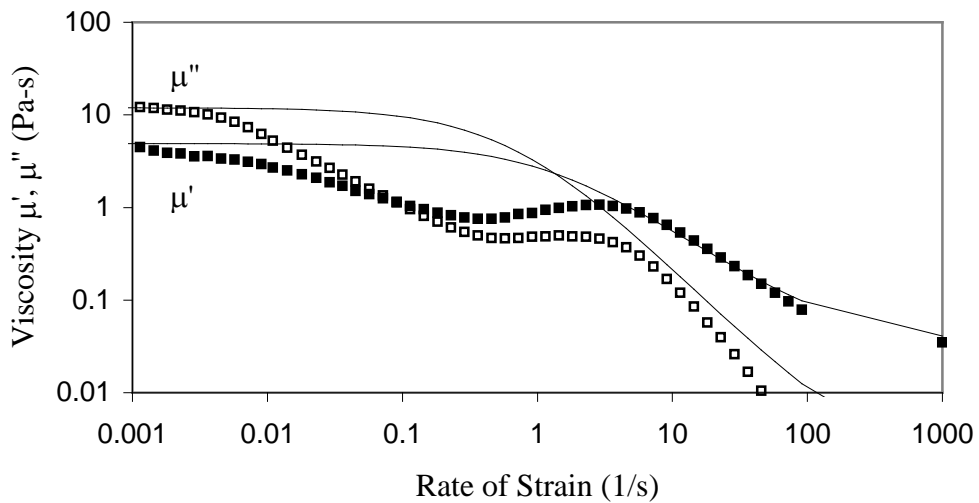


Figure 4-24. Measured oscillatory strain sweep results compared to flow curve results – Run 13B.

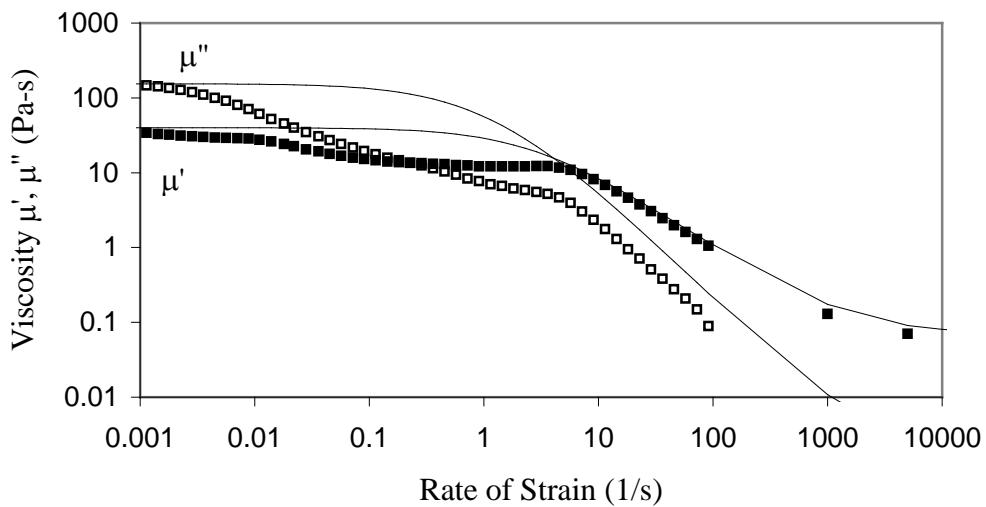


Figure 4-25. Measured oscillatory strain sweep results compared to flow curve results – Run 15B.

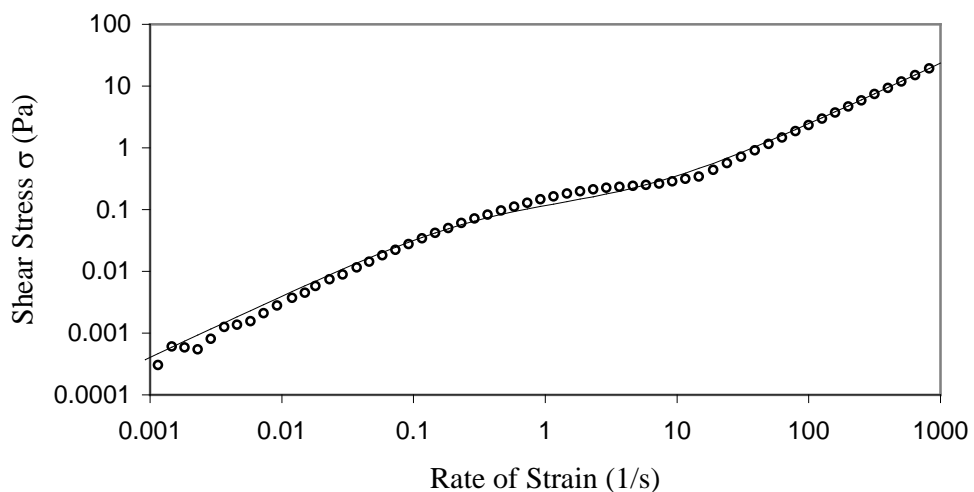


Figure 4-26. Measured shear stress versus rate of strain along with flow curve results – Run 1F.

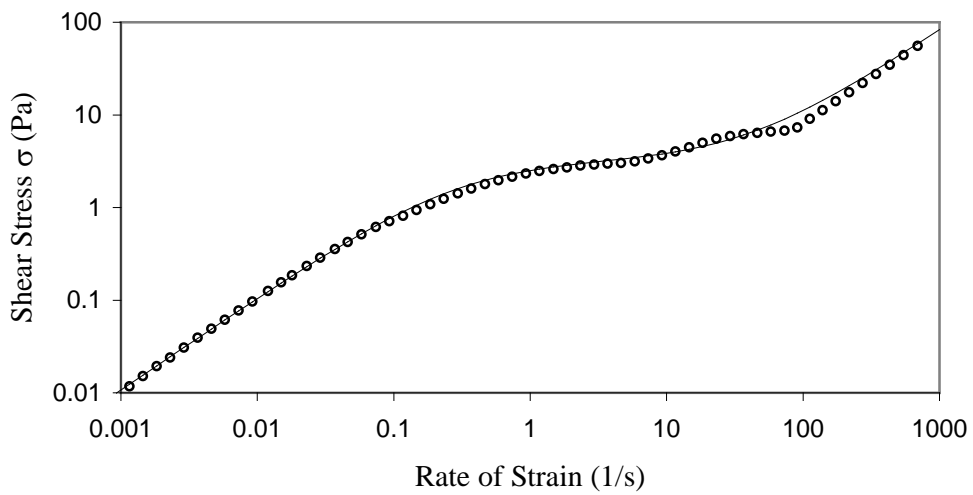


Figure 4-27. Measured shear stress verses rate of strain along with flow curve results – Run 3F.

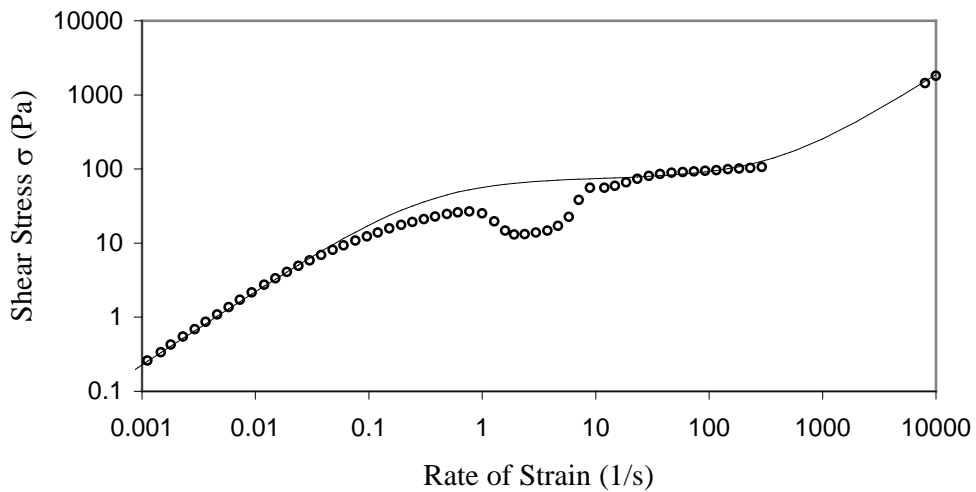


Figure 4-28. Measured shear stress verses rate of strain along with flow curve results – Run 5F.

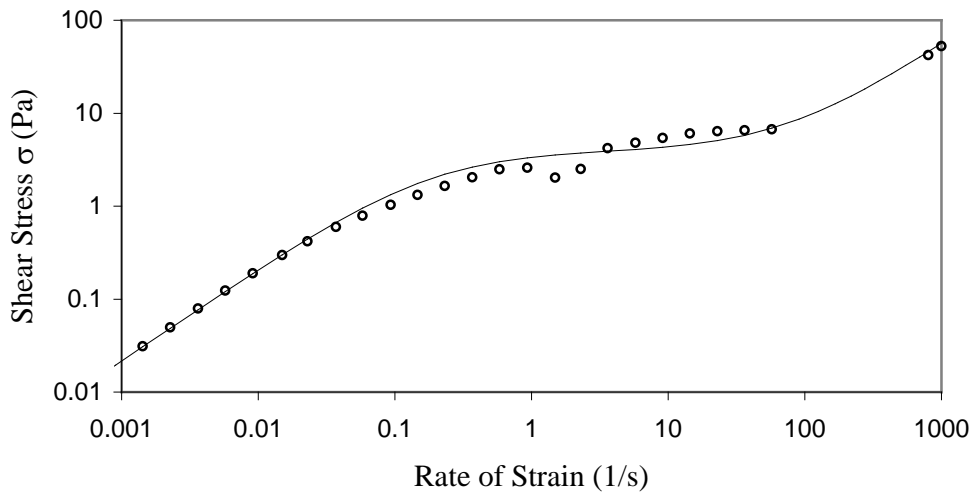


Figure 4-29. Measured shear stress verses rate of strain along with flow curve results – Run 8F.

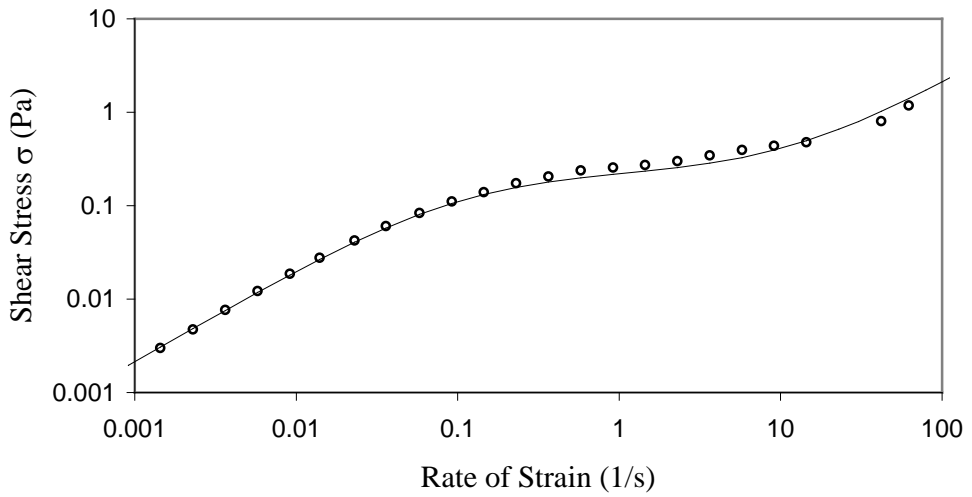


Figure 4-30. Measured shear stress verses rate of strain along with flow curve results – Run 11F.

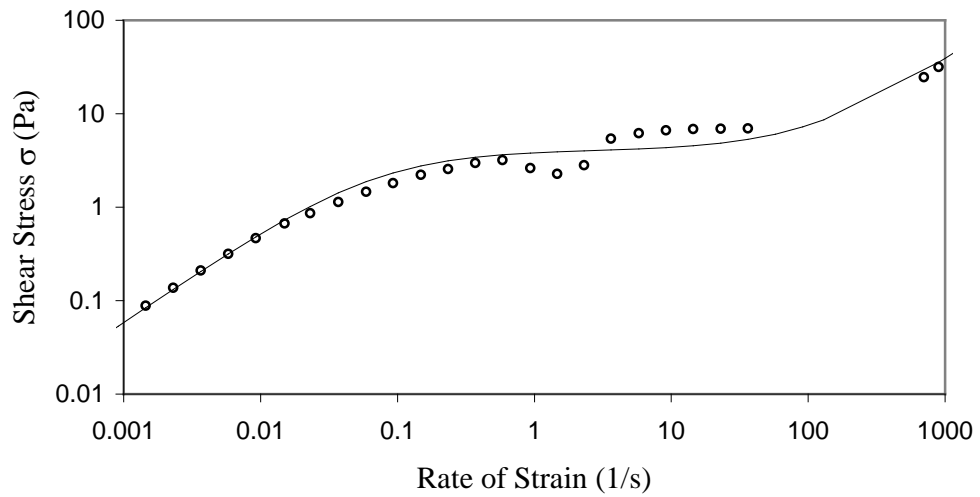


Figure 4-31. Measured shear stress verses rate of strain along with flow curve results – Run 13F.

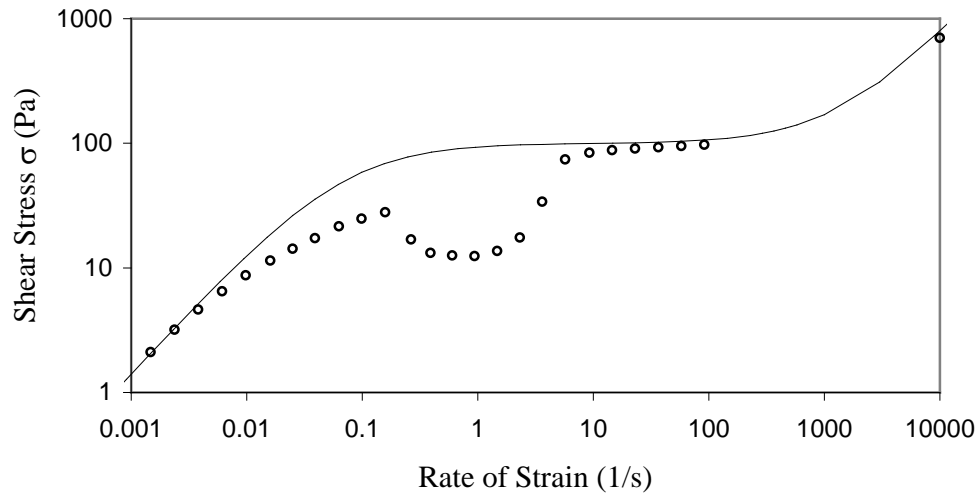


Figure 4-32. Measured shear stress verses rate of strain along with flow curve results – Run 15F.

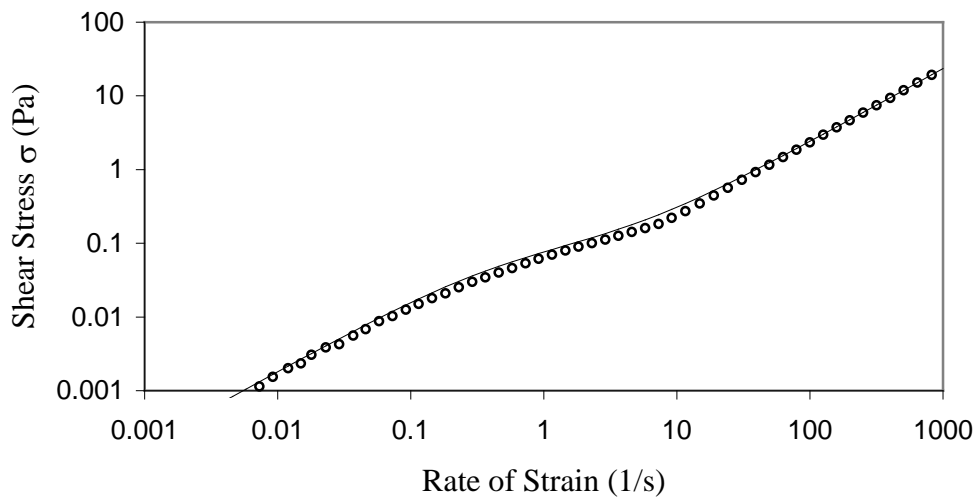


Figure 4-33. Measured shear stress verses rate of strain along with flow curve results – Run 1B.

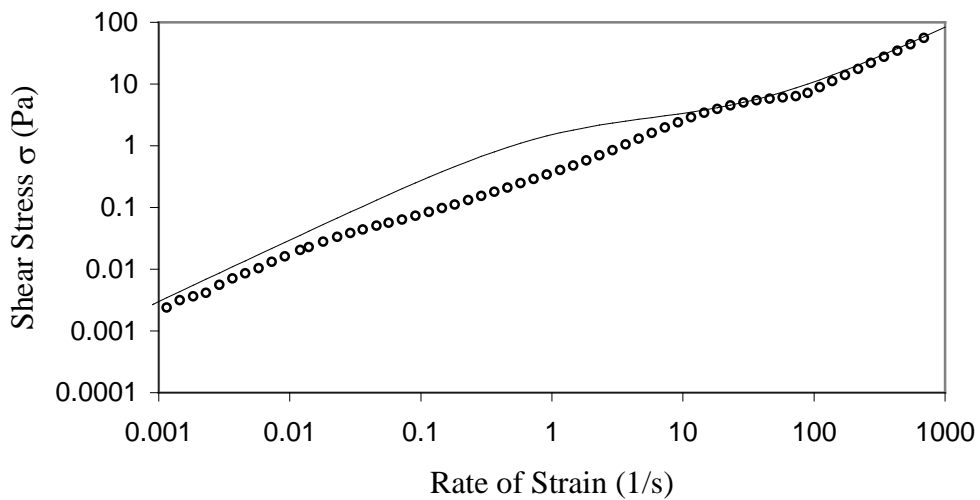


Figure 4-34. Measured shear stress verses rate of strain along with flow curve results – Run 3B.

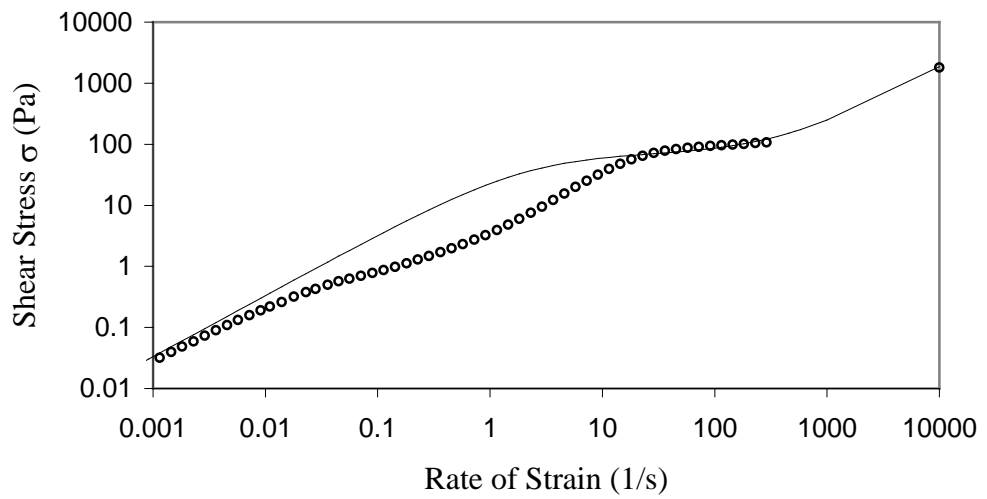


Figure 4-35. Measured shear stress verses rate of strain along with flow curve results – Run 5B.

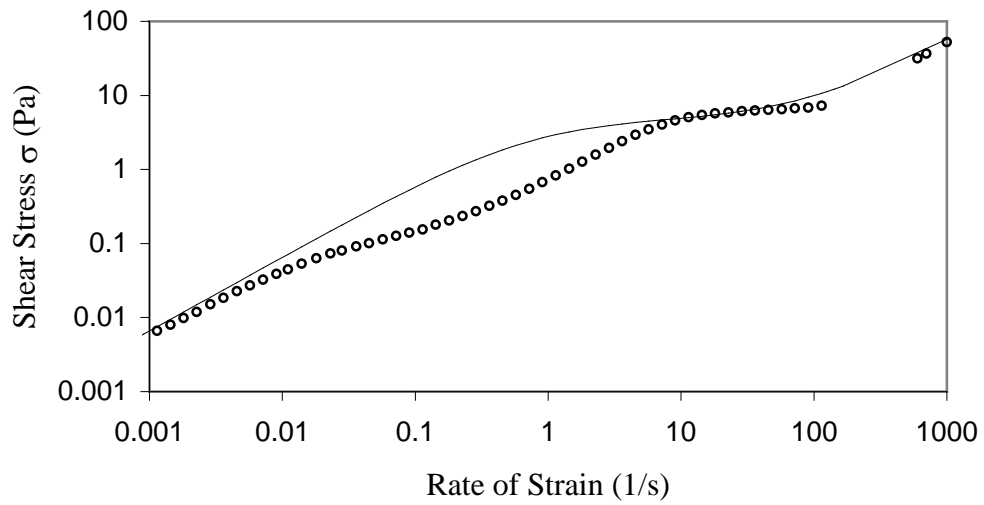


Figure 4-36. Measured shear stress verses rate of strain along with flow curve results – Run 8B.

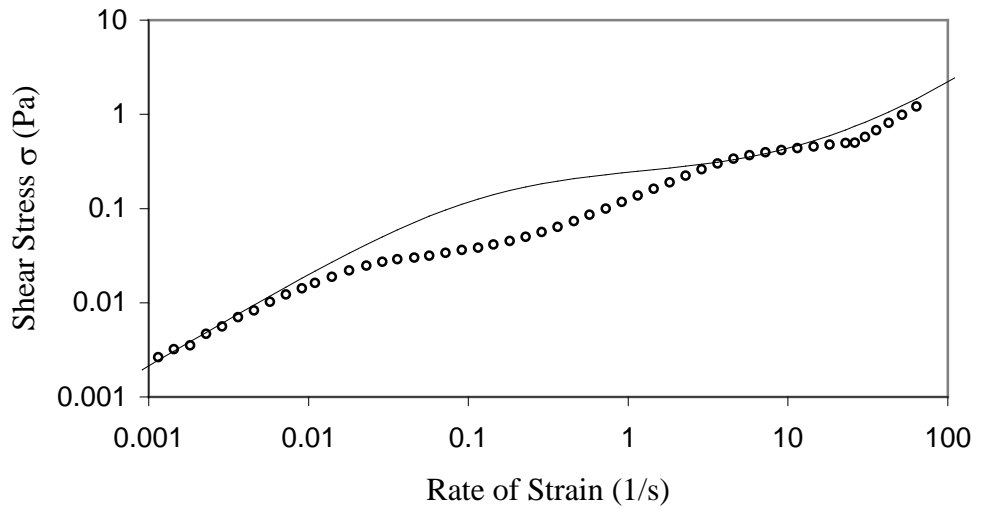


Figure 4-37. Measured shear stress verses rate of strain along with flow curve results – Run 11B.

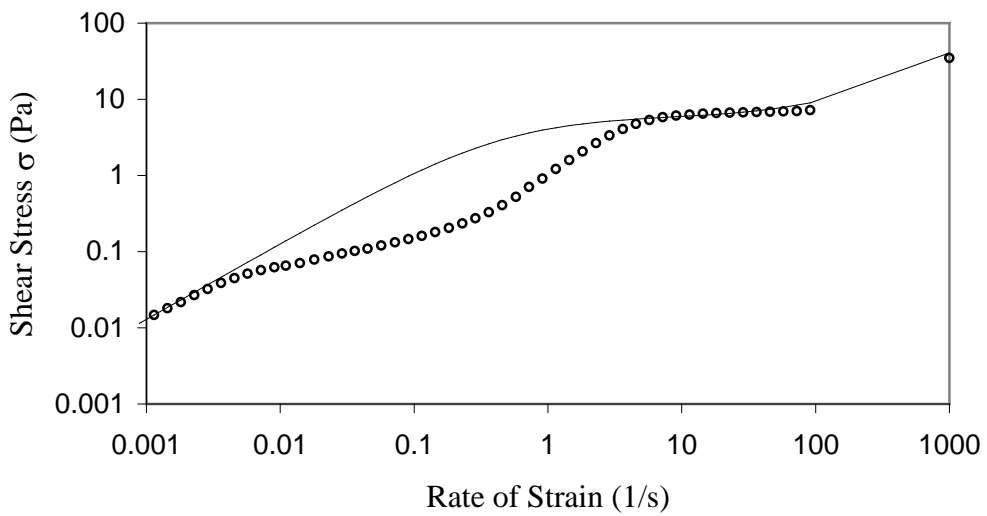


Figure 4-38. Measured shear stress verses rate of strain along with flow curve results – Run 13B.

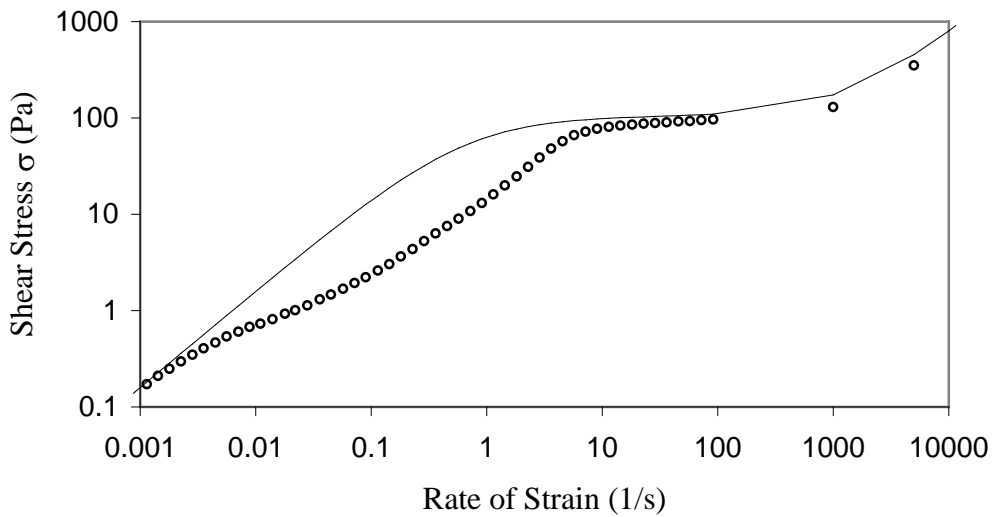


Figure 4-39. Measured shear stress verses rate of strain along with flow curve equations – Run 15B.

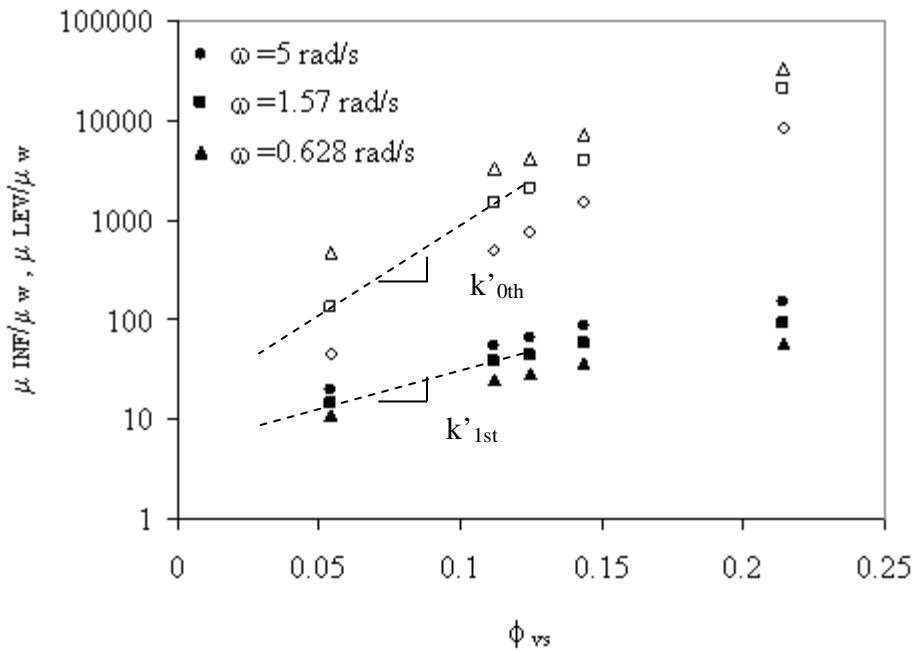


Figure 4-40. Normalized viscosity of AD Mud versus solids volume fraction from Table 4.2 data. Open symbols- μ'_INF/μ_w , Solid symbols-- μ'_LEV/μ_w .

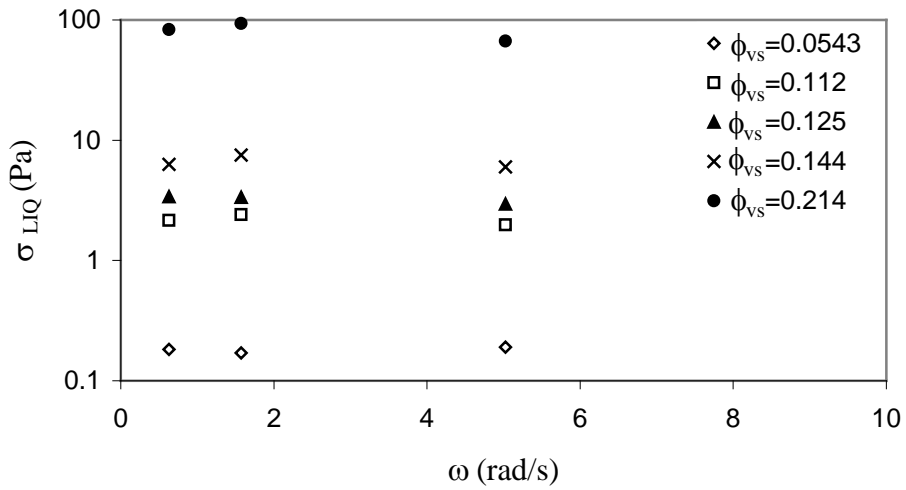


Figure 4-41. AD Mud shear strength verses solids volume fraction starting at low shear stress and ending at high shear stress.

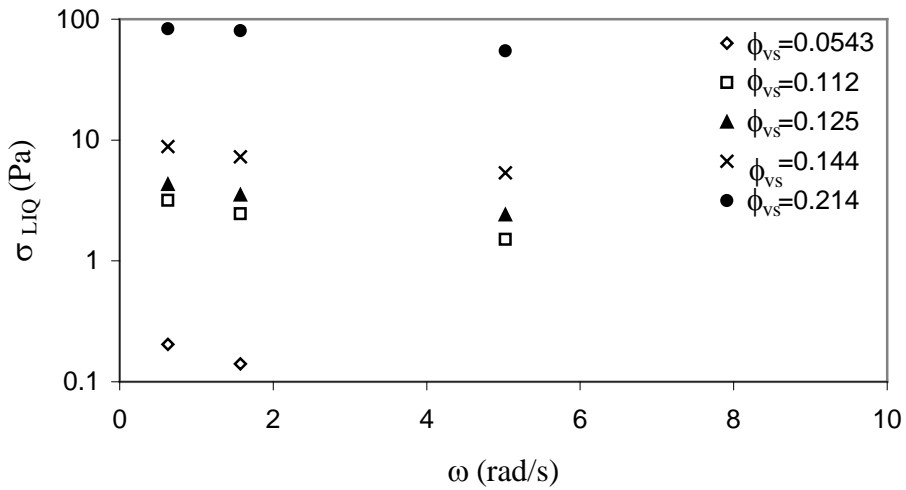


Figure 4-42. AD Mud shear strength verses angular frequency of oscillatory flow starting at high shear stress and ending at low shear stress.

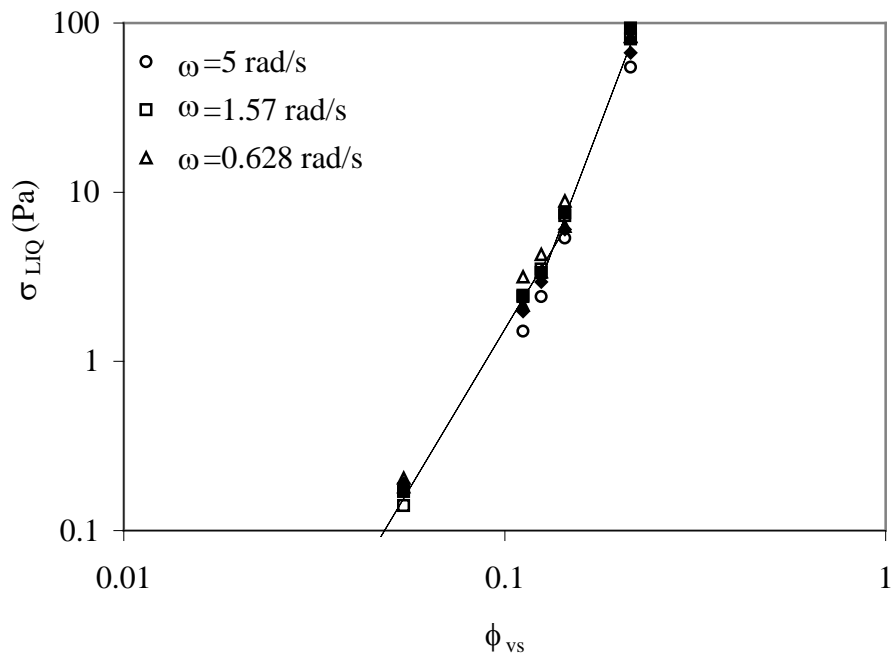


Figure 4-43. AD Mud shear strength verses solids volume fraction. Solid symbols indicate data starting at high shear stress and ending at low shear stress, Open symbols indicate data starting at low shear stress and ending at high shear stress.

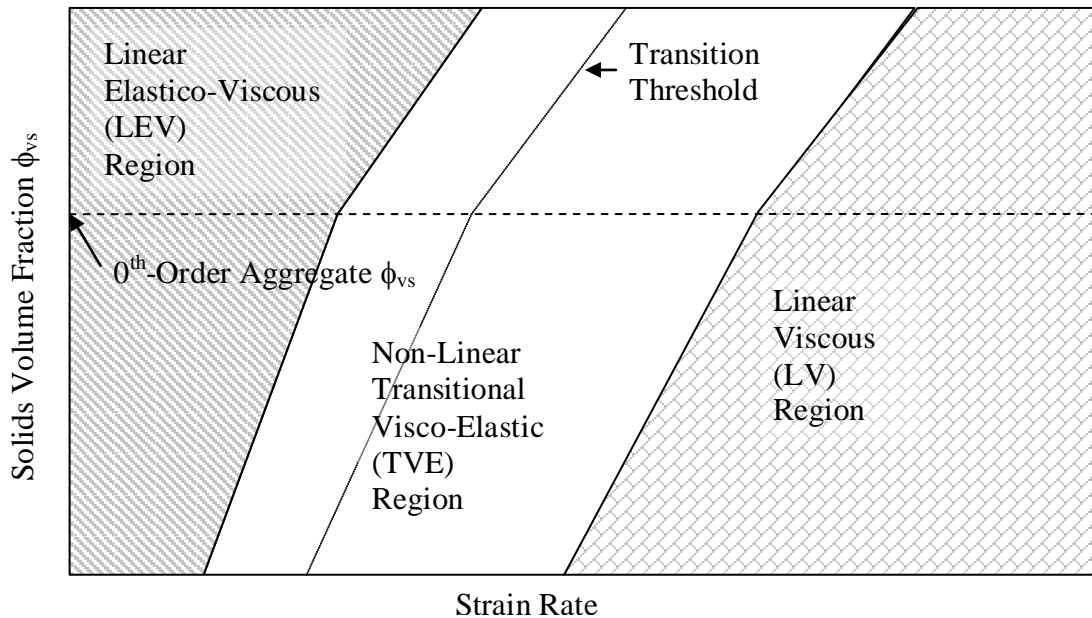


Figure 4-44. Sketch of AD Mud state influenced by strain rate and solids volume fraction.

CHAPTER 5

WAVE DISSIPATION AND SEABED TRANSITION

5.1 Model Formulation

The rate of strain profile with depth represents the response of the seabed to an external shear stress, σ as waves propagate over the seabed. Two noteworthy effects associated with wave-seabed interaction are attenuation of wave energy and motion/transition of the seabed. In this chapter a predictive model will be derived, based on the rheological equations of state, to: (1) quantify the rate at which wave energy flux is dissipated by the AD Mud bed, (2) describe the horizontal velocity gradient with depth in the seabed, and (3) define the depth of transition for a given wave condition and water depth.

The model will be derived from governing equations and boundary conditions that are consistent with the rheological methodology used. Figure 5-1 schematically defines the boundary value problem. Since this model approach is based on oscillatory shear rheology, the horizontal wave orbital velocity will be considered to represent the primary forcing mechanism acting at the bed interface. The problem will be structured as a Couette type flow for this reason. This assumption is appropriate for a soft mud bed exposed to wave induced shear stress from shallow water waves defined by Equation 5-1 [*Ochi, 1998*].

$$kd < \frac{\pi}{10} \text{ and/or } \frac{H}{d} > 0.24 \quad (5-1)$$

A soft mud bed behaves as a single-phase medium having viscous and elastic properties. It is formed by depositional settling and self-weight consolidation so the top layer is comprised of higher order aggregates which readily liquefy and advect when exposed to even mild shear stress.

5.1.1 Governing Equations

Ideal flow will be assumed in the water column. The AD Mud bed will be assumed to be of infinite thickness and to have constant density, ρ_2 . Although the problem assumes an infinitely thick bottom boundary layer, it is recognized that this boundary condition also realistically defines a mud bed of finite thickness that is greater than the depth of ‘productive’ motion. The term ‘productive’ motion is defined by the magnitude of rate of strain, $\dot{\gamma}$ as shown in Equation 5-2 and is discussed further in Section 5.2.1. Below this depth it is assumed that bed motion is insignificant.

$$\dot{\gamma} \geq .0001 \text{ s}^{-1} \quad (5-2)$$

It has been demonstrated that the AD Mud bed shows a tiered density structure. The solution to the constant density mud bed problem presented in this section can be applied to as many discrete density layers of a mud bed as necessary with the appropriate interface conditions defined to respect conservation of momentum and continuity. Due to the tiered density structure, the most significant bed motion occurs in the top density layer which represents the 0th order aggregate mud density.

The density profile of the AD Mud bed will be assumed to remain constant even when exposed to external oscillatory shear stress. This assumption is made based on flume studies conducted by Ross [1988] using estuarine sediment from Tampa Bay, FL. The clay fraction of this sediment was characterized as predominantly montmorillonite (smectite), which is similar to the composition of AD Mud. Ross demonstrated that the density profile within the bed did not vary significantly over time when exposed to wave-induced oscillatory flow during the flume tests.

5.1.2 Model Derivation-Water Column

Since energy is transmitted by waves generated at the free water surface, a model is necessary to describe how the energy is transmitted through the water column to the mud bed surface. The objective of this section is to define the horizontal water velocity, u , at the surface of the mud bed for a known wave condition, η . Based on Newton's second law, the horizontal equation of motion is given by Equation 5-3.

$$\frac{\partial u}{\partial t} + u \frac{\partial u}{\partial x} + w \frac{\partial u}{\partial z} = -\frac{1}{\rho} \frac{\partial p}{\partial x} + \frac{\mu}{\rho} \frac{\partial^2 u}{\partial z^2} \quad (5-3)$$

The ideal flow will also be assumed to be irrotational defined by Equation 5.4.

$$\frac{\partial u}{\partial z} = \frac{\partial w}{\partial x} \quad (5-4)$$

The velocity potential, ϕ , is introduced for irrotational flow which allows representation of velocity, u , a vector, in terms of a scalar function through the relationship shown by Equation 5-5.

$$u_\phi = \frac{\partial \phi}{\partial x} \quad (5-5)$$

Due to the incompressibility of the flow, conservation of mass shown by Equation 5-6 is applied to Equation 5-5 and results in the Laplace Equation (Equation 5-7).

$$\frac{\partial u}{\partial x} + \frac{\partial w}{\partial z} = 0 \quad (5-6)$$

$$\frac{\partial}{\partial x} \left(\frac{\partial \phi}{\partial x} \right) + \frac{\partial}{\partial z} \left(\frac{\partial \phi}{\partial z} \right) = \nabla^2 \phi = 0 \quad (5-7)$$

The kinematic and dynamic free surface boundary conditions are shown by Equations 5-8 and 5-9 respectively and specify that there must be no flow across the interface and a constant pressure

must be maintained across the interface. These conditions result in the dispersion equation shown by Equation 5-10 and which will be used to define the velocity potential, ϕ .

$$\frac{\partial \phi}{\partial t} + g\eta = 0 \quad (5-8)$$

$$\frac{\partial \eta}{\partial t} = \frac{\partial \phi}{\partial z} \quad (5-9)$$

$$\omega^2 = gk \tanh kh \quad (5-10)$$

The velocity potential, ϕ , for a progressive wave, based on linear wave theory, is defined by Equation 5-11.

$$\phi = \frac{H}{2} \frac{g}{\omega} \frac{\cosh k(h+z)}{\cosh kh} \sin(kx - \omega t) \quad (5-11)$$

H is the surface wave height, g is gravitational acceleration, ω is the water wave angular velocity, k is the wave number, h is the water depth, z is defined such that $z=0$ at the free surface and $z=-h$ at the seabed interface.

The horizontal velocity, u in the water column is defined from Equation 5-5 and given by Equation 5-12.

$$u(x, z, t) = u_\phi(x, z, t) = \frac{H}{2} \frac{\omega \cosh k(h+z)}{\sinh kh} \cos(kx - \omega t) \quad (5-12)$$

This solution satisfies the linearized form of Equation 5-3 under inviscid flow conditions represented by Equation 5-13.

$$\frac{\partial u_\phi}{\partial t} = -\frac{1}{\rho} \frac{\partial p}{\partial x} \quad (5-13)$$

This horizontal velocity profile results in an exponentially decay of velocity with depth. The rate of decay is governed by the wave length, λ , in the form of the wave number, k . Short wave length waves (higher frequency) will decay more rapidly away from the free surface than longer

wave length waves (lower frequency). As a result, the horizontal velocities of longer waves are able to propagate down to deeper water column depths.

5.1.3 Model Derivation- Seabed

It is the objective of this section to describe the motion in the mud bed resulting from the wave energy that is transmitted to the mud surface. The bed is assumed to be thick enough that ‘productive’ motion ends at a finite depth within the bed and the flow within the bed is governed by the viscoelastic properties of the mud. The equation of motion (Equation 5-3) is applied in linearized form to the mud seabed. However, unlike in the water column, viscosity is the dominant influence on the flow in the mud bed. As a result, the horizontal velocity in the bed is shown by Equation 5-14 defined by the rotational component.

$$u_B = u_r(x, z', t) \quad (5-14)$$

The incorporation of this interface boundary condition into the equation of motion (Equation 5-3) results in the relationship shown by Equation 5-15.

$$\frac{\partial u_r}{\partial t} = \frac{|\mu^*|}{\rho_2} \frac{\partial^2 u_r}{\partial z'^2} \quad (5-15)$$

This equation will be used to define the bed motion. Equation 5-15 is solved by separation of variables. The non-zero term of the general solution requires u to decay with depth into the bed. Equation 5-16 presents the general solution.

$$u_r = A e^{-\alpha z'} e^{i(kx - \omega t)} \quad (5-16)$$

Substituting Equation 5-16 into Equation 5-15 gives

$$\alpha = \pm \sqrt{\frac{-i\omega\rho_2}{|\mu^*|}} \quad (5-17)$$

$$\sqrt{i} = \frac{(1+i)}{\sqrt{2}} \quad (5-18)$$

Let

$$\beta = \sqrt{\frac{\omega \rho_2}{2|\mu^*|}} \quad (5-19)$$

A second vertical axis, referenced from the water column / mud bed interface, is introduced and designated by z' with the positive direction of the axis directed downward into the bed to facilitate solution of Equation 5-16. The no-slip boundary condition at the water column/mud bed interface, at $z' = 0$ is defined by Equation 5-20.

$$u_{\phi l} = u_{r2} \quad (5-20)$$

Applying this boundary condition to Equation 5-16 and taking the real part gives Equation 5-21.

$$u_r(x, z', t) = \frac{H}{2 \sinh kh} \frac{\omega}{e^{-\sqrt{\frac{\omega \rho_2}{2|\mu^*|}} z'}} \cos \left(kx - \omega t + \sqrt{\frac{\omega \rho_2}{2|\mu^*|}} z' \right) \quad (5-21)$$

5.2 Model Application

The model derivations presented in Section 5.1 will be used to characterize (1) horizontal bed motion, $u(z')$, (2) bed rate of strain profile, $\dot{\gamma}(z')$, (3) bed shear stress profile, $\sigma(z')$, (4) depth to which transition occurs, h_d , and (5) energy flux absorbed by the seabed, ϵ_D , from waves.

5.2.1 Seabed Dynamics

To first order, the velocity profile within the bed is given by Equation 5-21. The rate of strain profile, $\dot{\gamma}(z')$, follows as the derivative of Equation 5-21 and is shown by Equation 5-24.

$$\dot{\gamma}(z') = \frac{\partial u_r}{\partial z'} = \frac{H\omega}{2 \sinh kh} \sqrt{\frac{\omega \rho_2}{|\mu^*|}} e^{-\sqrt{\frac{\omega \rho_2}{2|\mu^*|}} z'} \left[\cos \left(kx - \omega t + \sqrt{\frac{\omega \rho_2}{2|\mu^*|}} z' \right) + \sin \left(kx - \omega t + \sqrt{\frac{\omega \rho_2}{2|\mu^*|}} z' \right) \right] \quad (5-22)$$

with

$$\sin(x) + \cos(x) = \sqrt{2} \sin\left(x + \frac{\pi}{4}\right) \quad (5-23)$$

results in

$$\dot{\gamma}(z') = \frac{\partial u_r}{\partial z'} = \frac{H\omega}{2 \sinh kh} \sqrt{\frac{\omega\rho_2}{|\mu^*|}} e^{-\sqrt{\frac{\omega\rho_2}{2|\mu^*|}} z'} \left[\sin\left(kx - \omega t + \sqrt{\frac{\omega\rho_2}{2|\mu^*|}} z' + \frac{\pi}{4}\right) \right] \quad (5-24)$$

The oscillatory component of the solution in Equation 5-24 includes a phase shift due to the propagating nature of the flow into the bed layer of ‘productive’ motion. It is important to recognize this result but for the five model application objectives noted, the time-dependent (periodic) component of the result is not significant. What is of interest is the maximum value or the amplitude. The amplitude of the rate of strain is depicted by Equation 5-25.

$$|\dot{\gamma}(z')|_{\max} = \left| \frac{\partial u_r}{\partial z'} \right|_{\max} = \frac{H\omega}{2 \sinh kh} \sqrt{\frac{\omega\rho_2}{|\mu^*|}} e^{-\sqrt{\frac{\omega\rho_2}{2|\mu^*|}} z'} \quad (5-25)$$

It was shown by Equation 4-8 that the magnitude of complex viscosity, $|\mu^*|$, may be written in terms of $|\mu^*(\dot{\gamma})|$. This allows z' in Equation 5-25 to be defined in terms of wave parameters, H , ω , k , and h , and rate of strain, $\dot{\gamma}$. Equation 5-26 shows this result.

$$z'(\dot{\gamma}) = \sqrt{\frac{2|\mu^*(\dot{\gamma})|}{\omega\rho_2}} \ln\left(\frac{H\omega}{2 \sinh(kh)|\dot{\gamma}|} \sqrt{\frac{\omega\rho_2}{|\mu^*(\dot{\gamma})|}}\right) \quad (5-26)$$

Since the depth of zero rate of strain does not exist due to the exponential nature of decay, a very small rate of strain is selected which effectively represents zero rate of strain. Consistent with the lower limit of $\dot{\gamma}$ that could reliably be measured by the rheometer, $\dot{\gamma} = 0.0001 \text{ s}^{-1}$ will be selected. The range of strain rate within the bed layer of ‘productive’ motion is therefore given by Equation 5-27.

$$\left[0.0001 \leq |\dot{\gamma}(z')|_{\max} \leq \frac{H\omega}{2 \sinh kh} \sqrt{\frac{\omega\rho_2}{|\mu^*(\dot{\gamma})|}} \right] \quad (5-27)$$

The rate of strain profile, $|\dot{\gamma}(z')|_{\max}$, can now be constructed by incrementing $|\dot{\gamma}(z')|_{\max}$ over the range defined by Equation 5-27. Equation 5-26 may then be solved for the discrete depths which correlate with the $|\dot{\gamma}(z')|_{\max}$ values using the following approach:

$$\gamma_0 = 0.0001 \text{ s}^{-1} = \gamma_{z_p}, \text{ for } m=1 \text{ to } n,$$

$$\dot{\gamma}_m = \gamma_{m-1} + \frac{m}{200} \frac{H\omega}{\sinh kh} \sqrt{\frac{\omega\rho_2}{|\mu^*(\dot{\gamma}_{m-1})|}} \gamma_0 \quad (5-28)$$

$z'_0 = z'_p$, for $z'_{m-1} = z'_p$ to 0,

$$z'_{m-1} = \sqrt{\frac{2|\mu^*(\dot{\gamma}_{m-1})|}{\omega\rho_2}} \ln \left(\frac{H\omega}{2 \sinh(kh) |\dot{\gamma}_{m-1}|} \sqrt{\frac{\omega\rho_2}{|\mu^*(\dot{\gamma}_{m-1})|}} \right) \quad (5-29)$$

With $z'(\dot{\gamma})$ defined by Equation 5-29, the rheological properties of the bed can be specified over a discrete depth. Objective (1) to characterize horizontal bed motion, $|u(z')|_{\max}$, may now be achieved by applying the results of Equation 5-29 and Equation 4-8 to Equation 5-21. Objective (2) to characterize bed rate of strain profile, $|\dot{\gamma}(z')|_{\max}$, follows directly from Equation 5-29. Objective (3) to characterize the bed shear stress profile, $|\sigma(z')|_{\max}$, may now be achieved by applying the results of Equation 5-29 to Equation 4-12. Objective (4) to obtain the depth to which transition occurs, h_d , may now be determined as the depth where $\sigma_{LIQ} = |\sigma(z')|_{\max}$ from Equation 4-18 and objective (3), respectively (Figure 5-2). Model application objective (5) to determine the energy absorbed by the seabed, ε_D , from waves is described in Section 5.2.2.

5.2.2 Wave Energy Dissipation

Wave energy flux dissipation, ε_D , defined as the work done by water waves against the shear stress within the active boundary layer of the mud seabed, is represented by Equation 5-30 [Dean and Dalrymple, 1991].

$$\varepsilon_D = \mu' \overline{\int_0^{z'} 2 \left(\frac{\partial u_r}{\partial x} \right)^2 + \left(\frac{\partial w}{\partial x} + \frac{\partial u_r}{\partial z} \right)^2 dz'} \quad (5-30)$$

This equation can be simplified due to the water column/mud bed interface boundary condition shown in Figure 5-1 which results in the assumptions given by Equation 5-31 and Equation 5-32.

$$\frac{\partial u_r}{\partial z} \gg \frac{\partial u_r}{\partial x} \quad (5-31)$$

$$\frac{\partial u_r}{\partial z} \gg \frac{\partial w}{\partial x} \quad (5-32)$$

Substituting $\mu' = \mu'(\dot{\gamma})$ from Equation 4-10, Equation 5-30 is represented by Equation 5-33.

$$\varepsilon_D = \int_0^{z'_p} \frac{\mu'_{\text{INF}} \dot{\gamma}^3 + \mu'_{\text{LEV}} \dot{\gamma}_{\text{LIQ}} \dot{\gamma}^2}{\dot{\gamma} + \dot{\gamma}_{\text{LIQ}}} dz' \quad (5-33)$$

z'_p represents the bed depth at which ‘productive’ motion terminates as defined by the criterion shown by Equation 5-2. The quantity ε_D can be calculated using a numerical scheme for solving a closed integral since the rate of strain profile with depth in the bed was determined in Section 5.2.1. The quantity ε_D was calculated using discrete summation of ε_D over small depth increments applying the trapezoidal rule as shown by Equation 5-34.

$$\varepsilon_D = \sum_{i=0}^{i=z'_p | \dot{\gamma}=0.0001} \frac{\mu'_{\text{INF}} |\dot{\gamma}(z'_i)|_{\text{max}}^3 + \mu'_{\text{LEV}} \dot{\gamma}_{\text{LIQ}} |\dot{\gamma}(z'_i)|_{\text{max}}^2}{|\dot{\gamma}(z'_i)|_{\text{max}} + \dot{\gamma}_{\text{LIQ}}} \Delta z' \quad (5-34)$$

Assuming a normally incident wave propagation path, ε_D may be defined in terms of energy conservation by Equation 5-35.

$$\varepsilon_D = -\frac{d}{dx} (EC_g) \quad (5-35)$$

where C_g is the wave group velocity in the x-direction and E=total average wave energy per unit surface area defined by Equations 5-36 and 5-37, respectively.

$$C_g = \frac{\omega}{2k} \left(1 + \frac{2kh}{\sinh 2kh} \right) \quad (5-36)$$

$$E = \frac{1}{8} \rho g H_x^2 \quad (5-37)$$

H_x is the wave height at a distance x along the propagation path of the wave.

$$H_x = H_0 e^{-k_i x} \quad (5-38)$$

k_i is the spatial damping rate of the propagating wave and can be defined for a constant water depth, h , (for which $C_{g0}=C_{gx}$) by substitution of Equations 5-37 and 5-38 into Equation 5-35.

$$k_i = \frac{\varepsilon_D}{2EC_g} \quad (5-39)$$

The form of Equation 5-35 is convenient when directly measuring the dissipation of wave energy by comparison of wave energy at discrete intervals along the path of wave propagation. Based on the assumption made by Equation 5-38, ε_D can be defined in terms of energy flux, EC_g by Equation 5-40.

$$\varepsilon_D = \frac{EC_g}{x} \ln \left(\frac{E_0}{E} \right) \quad (5-40)$$

E_0 is the wave energy at location $x=0$. Eq. 5-40 assumes constant water depth which is reasonable in locations such as the topset and foreset clinoform areas of the Atchafalaya River Delta. The slope of the topset seaward of the CSI3 sample site is 0.0063° which indicates a 1 m change in depth, from approximately 4 m at CSI3 to 5 m, over a distance of 10 km (Figure 2-4).

As waves propagate over the mud bed, energy is transferred from the wave field to the bed which induces oscillatory motion in the bed. The transferred energy is manifested as kinetic energy and ultimately as heat energy. The relative motion of the particles in the mud converts a portion of the transferred energy into heat energy due to friction within the transitioned thickness of the bed. The kinetic energy per unit bed surface area is given by Equation 5-41.

$$E_k = \frac{1}{2} \rho_2 h_d \overline{|u_{max}|^2} \quad (5-41)$$

where $\overline{|u_{max}|}$ is the average horizontal velocity over the predominantly viscous transitioned layer.

The specific heat of the mud determines the heat energy required to raise the temperature of the mud a unit degree per unit surface area, per wave period based on the relationship shown by Equation 5-42.

$$q = c_p \rho \delta_T \frac{\omega}{2\pi} \Delta T \quad (5-42)$$

q = heat energy $\left(\frac{J}{m^2 \cdot s} \right)$, c_p = specific heat capacity $(\frac{J}{kg \cdot ^\circ C})$, δ_T = predominantly viscous mud thickness (m).

Conservation of energy dictates the approximate energy balance as shown by Equation 5-43.

$$\varepsilon_D = E_k = q \quad (5-43)$$

An estimate of the temperature rise in the transitioned thickness of the mud bed as a result of wave energy dissipation is shown by Equation 5-44.

$$\Delta T (^{\circ}C) = \frac{2\pi}{\omega} \frac{\varepsilon_D}{c_p \rho \delta_T} \quad (5-44)$$

The specific heat capacity of smectite mud in marine environments was measured by *Cara et al.* [2000] and shown by Equation 5-45.

$$c_p \approx 3,100 \frac{J}{kg \cdot ^\circ C} \quad (5-45)$$

The derived model will be evaluated against measured ε_D data obtained from wave flume runs in the next chapter.

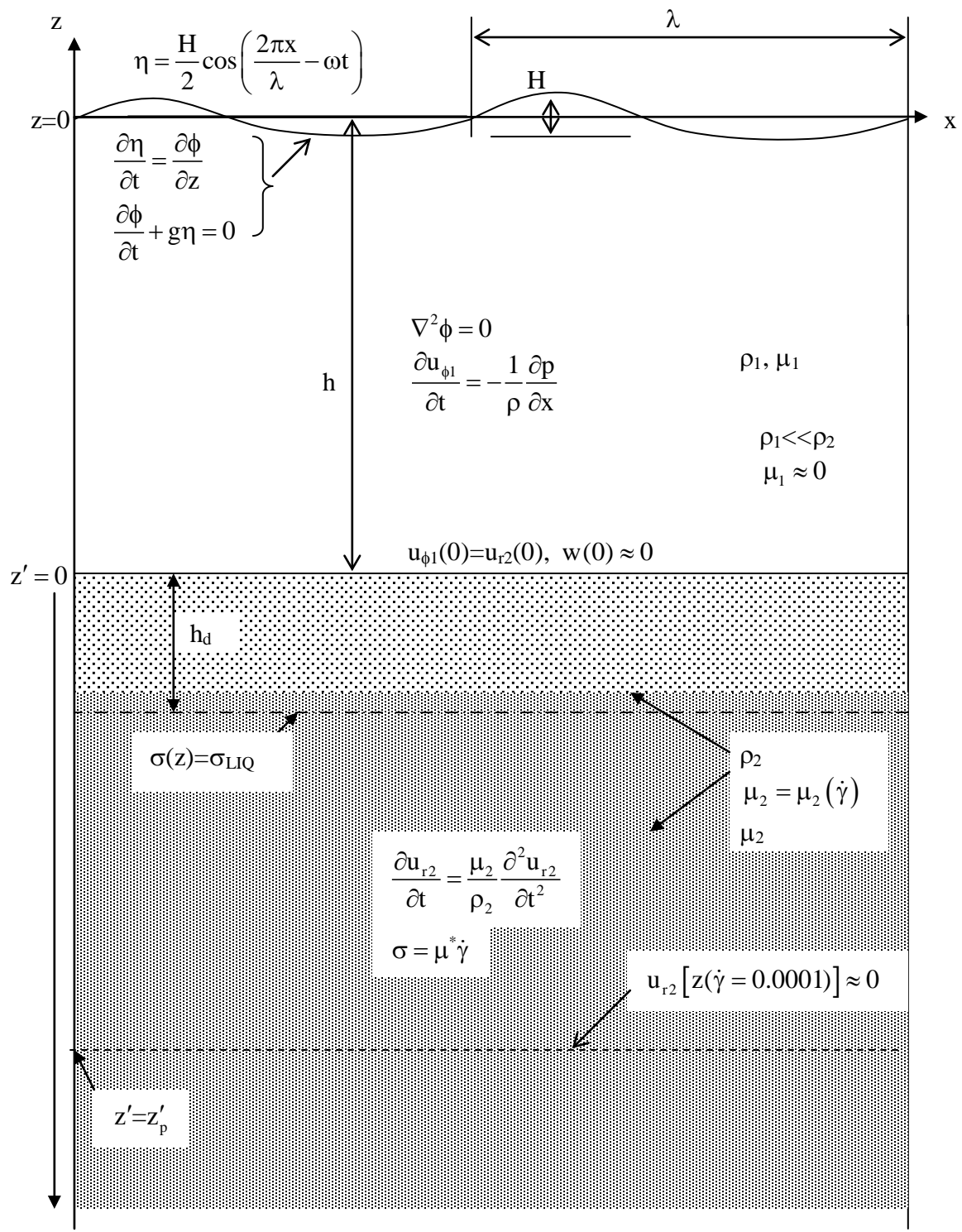


Figure 5-1. Schematic of boundary value problem.

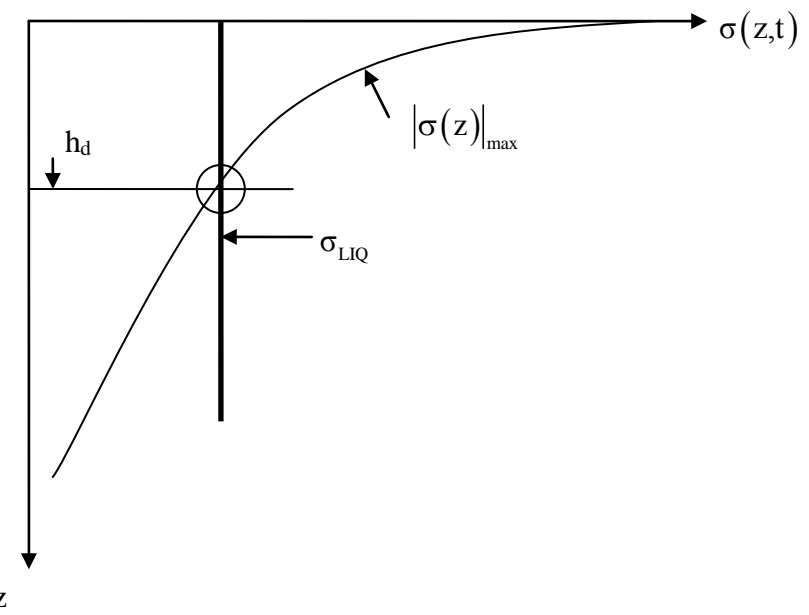


Figure 5-2. Schematic of transitioned layer thickness, h_d .

CHAPTER 6

ASSESSMENT OF TRANSITIONED THICKNESS AND ENERGY DISSIPATION

6.1 Wave Flume

6.1.1 Equipment and Instrumentation

Wave flume tests were designed to measure the response of AD Mud to oscillatory wave forcing. The flume dimensions were: length 20 m, width 46 cm and height 45 cm. A piston-type wave-maker capable of generating monochromatic waves was installed at one end of the flume. The amplitude and frequency of the waves could be adjusted by a DC motor controller. A trench was constructed approximately 6 m from the wave-maker with sloped ends of 1:12 allowing space to confine seabed material up to 12 cm in depth and 5 m in length (Figure 6-1). Two capacitance-type wave gauges were mounted on the flume to measure surface displacement (Figure 6-2). One wave gauge was mounted at the front section of the trench and the other was mounted at the back end. Surface elevation data, collected at a frequency of 10 Hz, were digitized via a DataLogger data acquisition system and processed using Global Lab software.

6.1.2 Wave Attenuation Characteristics

During previous studies using this flume, wave reflection and attenuation characteristics of the system were analyzed. Wave reflection was mitigated with honeycombed wave absorbing material placed at both ends of the flume along sloping beaches. *Feng* [1992] conducted wave attenuation measurements using an experimental technique by *Goda and Suzuki* [1976]. It was determined that the average wave reflection coefficient was less than 0.3 for waves with angular frequency in the range of 3 to 12 rad/s and with amplitudes of 0.5 to 2 cm indicating that waves within this range remain predominantly progressive in nature. During the present study, additional attenuation material was incorporated into the sloped beaches making the results from the above analysis the unlikely worst case. Also, wave reflection calculations were made with a

rigid false bottom placed over the trench. The presence of AD Mud reduced the wave energy reaching the flume end by up to 75%. As a result less wave energy was available to be reflected.

Feng [1992] quantified side-wall and bottom friction to be equivalent to wave damping coefficient $k_i=0.02 \text{ m}^{-1}$ on average. Using the relationship between k_i and ε_D defined by

Equation 6-16, this translates into wave energy dissipation of approximately $\varepsilon_D=0.045 \frac{\text{J}}{\text{m}^2\text{s}}$. It

should be noted however that this result is a slight over-estimate for tests involving sediment in the trench. This is because *Feng* [1992] measured the wave dissipation with a false bottom fabricated of plywood. This false bottom also contributed to wave dissipation during that study along with the side-walls.

6.1.3 Experimental Setup

The wave flume was filled with water with a salinity of approximately 9ppt. This is slightly less than the salinity of the Atchafalaya Delta region of the Gulf of Mexico but is adequate to ensure that flocculation of the sediment remained relatively consistent with that of a more saline environment. *Hayter* [1986] showed that for salinity levels exceeding 5 ppt, little change was noticed in the viscoelastic response of kaolinite. This lack of sensitivity is likely due to the presence of ample cations to form the full double layer which defines the floc structure at or above this salinity.

In reference to Figure 2-12 it was important to ensure the AD Mud bed had reached the consolidation phase of the settling sequence since this is the phase where the bed becomes essentially static. Since the bed depth was $z=0.08 \text{ m}$ (Figure 6-1) and the water depth for the flume runs was 0.19 m , the time to consolidation can be determined from Figure 2-12 by entering the y-axis at the value determined by Equation 6-1.

$$\frac{h}{h_0} = \frac{0.08m}{0.08m + 0.19m} = 0.30 \quad (6-1)$$

Figure 2-12 shows that after 48-72 hours, the bed has reached the consolidation phase.

The bed material was placed in the trench and the flume was filled with 9 ppt saline water to a depth of 0.19 m above the bed surface. The trench section was then confined using vertical portable end sections and the bed material thoroughly agitated so that it became uniformly suspended in the entire water column above the trench. The suspension was then allowed to settle for 60 hours. For a bed depth of 0.08 m, Figure 2-14 reveals that the density was relatively uniform throughout the bed based on the 2 day and 3 day solids volume fraction profiles. This solids volume fraction will be taken to be $\phi_{vs}=0.12$ for all test runs.

6.1.4 Test Run Protocol

Tests were performed as shown in Table 6-1 with the aim of conducting runs with diverse frequencies and amplitudes within the capabilities of the flume. Since wave attenuation data across the bed was the main objective, the lowest angular frequency was established to ensure that at least 2.5 wave lengths were able to traverse the bed. This limited the angular frequency to approximately 4 rad/s for the water depth in the flume.

Each run consisted of three phases. The initial phase was designed to represent a mild sea state and is depicted in Table 6-1 by the suffix ‘PER’. During this phase, the waves had low amplitude and high frequency. The second phase of each run was designed to represent a high energy event and is depicted in Table 6-1 by the suffix ‘R’. During this phase, the waves had larger amplitude and lower frequency. The final phase was designed to represent a mild sea state similar to the initial phase and is depicted in Table 6-1 by the suffix ‘POR’. The duration of each phase was long enough to observe how the bed adjusted to the ambient wave condition. This condition was determined by monitoring the surface elevation from the wave gauge at the down

wave end of the trench. When the output signal reached a steady, weakly ergodic state, the wave/seabed system was considered to be stable and data were collected for approximately twenty minutes to ensure enough surface elevation data were obtained for spectral analysis.

Figure 6-3 shows a continuous time series of wave elevations during a four-phase test run. This figure demonstrates that the bed responded within minutes to the wave conditions as evidenced by the rapidity with which a steady surface elevation at the back of the trench was reached. The bed response took slightly longer during the second phase of the test run [Figure 6-3 section (b)] as the bed responded to the more energetic waves. However, even under this condition, equilibrium was reached within 10 minutes. This trend agrees with the oscillatory time series in Figures 3-13 and 3-14 showing the complex viscosity components reaching near steady values within minutes after a change of the imposed shear stress.

The thixotropic property of the mud is subtly evident in this data time series (Figure 6-3).

By comparing the change in wave height, $\frac{H_x}{H_0}$, of test run segments (a) and (c), it is seen that the

mild pre-stress history of segment (a) results in greater wave energy dissipation than the more severe pre-stress history of segment (c) [Equation 6-2].

$$\frac{H_x}{H_{0(a)}} = 0.534 < \frac{H_x}{H_{0(c)}} = 0.562 \quad (6-2)$$

Comparison of these two segments is significant since the wave angular frequency, ω , and initial wave height, H_0 , are nearly identical.

An analysis of this effect is given in Table 6-2. In reference to Table 6-1, the initial test run wave conditions of PER4 and POR4 were very similar, which established a basis for comparison of the energy dissipation rates. As shown in Table 6-3, the PER4 run results showed a slightly greater ε_D as compared with the POR results. The same relative results were obtained

from the model calculations made for these test runs. Though it can be argued that the statistical significance of the difference between these results is not high due to the variance of the data, the consistency of results lends merit to the slight relative trend of the differences.

6.1.5 Test Run Results

A total of five coupled three-phase runs were performed in the flume with water depth, $h=0.19m$. The objective was to measure the change in the wave energy. Surface elevation data collected by both wave gauges during the most energetic wave condition of each test run, depicted by suffix ‘R’ (Table 6-1), were analyzed and the wave dissipation rate, ϵ_D , calculated.

Figure 6.4 depicts representative surface elevation time series during Test Run R2 at the front (a) and back (b) of the trench. Due to the shoaling effect of the ramped front end of the trench, second-order wave attributes manifest themselves with the presence of a second harmonic component to the fundamental wave frequency resulting in a non-Gaussian wave profile particularly at the front wave gauge position. The characteristic narrow, peaked crests and broad, shallow troughs are evident in Figure 6-4. For waves showing non-Gaussian, second-order properties, energy loss must be computed by spectral method to ensure that the total wave energy is calculated. The time series data are transformed into the frequency domain through application of Fast Fourier Transform defined in terms of wave frequency, f , shown by Eq. 6.3 [Bendat and Piersol, 1986].

$$X(f, T) = \int_0^T x(t) e^{-j 2 \pi f t} dt \quad (6-3)$$

This transformation decomposes the time series into discrete periodic functions with defined relative amplitudes of each component. The spectral density function of the water surface elevation time series, $x(t)$, is defined by Equation 6-4.

$$S_{xx}(f) = \lim_{T \rightarrow \infty} \frac{1}{T} |X(f, T)|^2 \quad (6-4)$$

The resulting function displays the relative energy contributions of each frequency bin. The total variance of the time series is related to the resulting spectral density function by Equation 6-5.

$$\text{var}(x) = \int S_{xx}(f) df \quad (6-5)$$

The variance of a narrow-banded spectral density function is a measure of the significant wave height shown by Equation 6-6.

$$H_s = 4 * \sqrt{\text{var}(x)} \quad (6-6)$$

Figure 6-5 presents the spectral density function for Test Run R2. Figure 6-5(a) depicts the spectrum for the data at the front of the trench correlated with the time series signal shown in Figure 6-4(a). Similarly, Figure 6-5(b) depicts the spectral density function for the data at the back of the trench correlated with the time series in Figure 6-4(b).

In comparison of Figures 6-5 (a) and (b), it is noticed that wave energy is reduced from both the fundamental frequency ‘bin’ and the second harmonic frequency ‘bin’. Though the second harmonic frequency at $\omega=8$ rad/s defines a wave in deep water, $kh>\pi$, energy is still reduced even though this wave component can not ‘feel’ the bottom to dissipate energy through direct interaction with the bed. This tangible energy dissipation occurs substantially due to the coupled nature of this component with the fundamental frequency component. As energy is dissipated from the fundamental frequency component by direct interaction with the bed, less energy is available for the second harmonic component.

The total wave energy dissipation rate, ϵ_D , calculated using Equation 5-32 consists of the dissipation rate of the bed and of the wave flume as assumed from the analysis by *Feng* [1992] and discussed in Section 6.1.2. Table 6-3 presents the results for Test Runs R1-R5 along with

the results from the model using Equation 5-16. Comparison of results shows agreement within 6% between the measured and model results. The complete model results for Test Run R2 will be presented in Section 6.2 to highlight bed dynamics.

6.2 Discussion of Model Results for Test Run R2

The model resolves the horizontal velocity profile within the bed, $|u(z')|_{max}$, shear stress profile, $|\sigma(z')|_{max}$, transitioned depth, h_d , real, imaginary and total viscosity profiles, $\mu'(z')$ $\mu''(z')$ and $\mu^*(z')$, respectively, and the wave dissipation rate profile, $\varepsilon_D(z')$. Model results will be presented based on wave energy dissipation measurements during test run R2.

6.2.1 Bed Velocity Profile

Figure 6-6 shows the amplitude of the horizontal velocity within the bed, $|u(z')|_{max}$, as a function of bed depth. This result was obtained from Equation 5-18 based on the solution of Equation 4-8 and Equation 5-26 defining $|\mu^*(z')|_{max}$ and z' , respectively. The velocity at $z'=0$ is equal to the horizontal velocity under the wave at the water/bed interface satisfying the boundary condition there. The non-linear nature of the velocity profile is evident from the test run R2 test results. The velocity is reduced by almost an order of magnitude within the top 0.06 m of the bed.

6.2.2 Bed Shear Stress Profile

Figure 6-7 shows the shear stress profile, $|\sigma(z')|_{max}$, in the bed. This result was obtained from Equation 4-12 applying the definition of $|\dot{\gamma}(z')|_{max}$ from the solution of Equation 5-26. The transitioned depth, h_d , is determined based on the flow equation (Equation 4-18). This depth is depicted in Figure 6-7 as the location where the bed shear stress is equal to the shear stress at transition.

$$|\sigma(z')|_{\max} = \sigma_{LIQ} \quad (6-7)$$

For test run R2, $h_d = 0.02$ m. This implies that the top 2 cm of the bed became predominantly viscous. It would be this thickness which would be susceptible to transport by steady flow.

6.2.3 Bed Viscosity Profile

Figures 6-8 and 6-9 show the real viscosity component, $|\mu'|_{\max}$, and total viscosity, $|\mu^*|_{\max}$, profiles with depth in the bed, respectively. These results were obtained from Equation 4-10 and Equation 4-8, respectively, and show the thixotropic properties of the mud. Real viscosity increases non-linearly with depth where the shear stress is low. However, the total viscosity profile is closely linear. These results demonstrate that the imaginary (storage) viscosity, orthogonal to the real viscosity, must also be non-linear and convex in profile. The imaginary viscosity is not presented since viscosity components are related.

6.2.4 Bed Wave Energy Dissipation Profile

Figure 6-10 shows incremental wave energy dissipation, $\varepsilon_D(z)$ as a function of depth in the bed. These results were obtained from Equation 5-31. The area to the left of the curve is equal to the calculated total wave energy dissipation rate, ε_D , shown in Table 6-3 for Test Run R2. The majority of the wave energy is dissipated within the predominantly viscous layer of the bed defined as the top 0.02 m for this test run. Within the top 0.08 m of the bed nearly all the wave energy dissipation takes place. This demonstrates that the bed depth ($z' = 0.08$ m) used in the flume satisfies, in principle, the ‘infinite’ depth assumption in the model. As long as the bed thickness exceeds the depth at which $|\dot{\gamma}|_{\max} = 0.0001$ the model will produce answers consistent with the assumption concerning bed thickness.

The temperature rise within the predominantly viscous transitioned thickness of the bed for Test Run R2 based on Equation 5-42 is shown by Equation 6-8.

$$\Delta T(^{\circ}\text{C}) = 0.26 \frac{\text{J}}{\text{m}^2 \cdot \text{s}} \frac{2\pi}{4.05 \frac{1}{\text{s}} 3,100 \frac{\text{J}}{\text{kg} \cdot ^{\circ}\text{C}} 1200 \frac{\text{kg}}{\text{m}^3} 0.02\text{m}} = 5.4 \times 10^{-6} ^{\circ}\text{C} \quad (6-8)$$

6.3 Wave Flume Mud Slope Analysis

During the flume test runs, near-bed transport of mud took place. Sediment within the transitioned thickness migrated down the flume and caused the bed to become mildly sloped from its initial flat condition. Ross [1988], during similar tests, observed a rapid development of a sloping bed and attributed this bed evolution to non-linearities of the oscillatory water velocities. The objective of this section is to introduce an analysis for the final settled bed slope (with angle, θ).

Figure 6-11 shows bed elevations along the trench. Measurements began 100 cm past the start of the trench to avoid bed elevation anomalies caused by the presence of the front ramp. Measurements following two runs of similar test wave conditions were collected and the resulting bed slopes were similar in both runs. The average bed slope was determined by Equation 6-9.

$$\text{Avg. slope} = \frac{1.95 \text{ cm}}{400 \text{ cm}} = 0.0049 \quad (6-9)$$

This slope is the result of mud flow up the slope during wave forcing. The flow continued until equilibrium was reached between the momentum associated with the shear stress gradient in the bed and gravity. A definition sketch of the problem is presented by Figure 6-12. Equation 6-10 defines the general form of the momentum equation.

$$\rho \frac{D u_w}{D t} = \rho g \sin \theta + \frac{\partial \sigma}{\partial z} \quad (6-10)$$

θ is the angle of the final bed slope. Assuming the flow is steady state, the material derivative of horizontal velocity, u_w , becomes zero and Equation 6-10 reduces to Equation 6-11.

$$\frac{\partial \sigma}{\partial z} = -\rho g \sin \theta \quad (6-11)$$

Equation 6-11 defines the hydrostatic force balance. Integrating gives Equation 6-12.

$$\sigma(z) = -\rho g z \sin \theta + \text{constant} \quad (6-12)$$

The integration constant is determined by applying the dynamic boundary condition shown by Equation 6-13. Since this study considers the thickness of the mud bed as infinite and to simplify the solution to Equation 6-12 the vertical axis convention z' used in Figure 5-1 will be adopted in this section as well. In reference to Figure 6-13, $z'=0$ defines the elevation of the water column/mud bed interface and is positive downward into the bed.

$$\sigma(z' = h_d) \approx 0 \quad (6-13)$$

This boundary condition in the bed is assumed since at shear stresses less than σ_{LIQ} , ($\sigma < \sigma_{LIQ}$), the bed structure resists flow. The solution to Equation 6-10 is thus shown by Equation 6-14.

$$\sigma(z') = \rho g (h_d - z') \sin \theta \quad (6-14)$$

The maximum value of σ will occur at $z' = 0$ which is the surface of the bed. As a result, motion of the predominantly viscous top layer of the bed will continue as long as the criterion of Equation 6-15 is met.

$$\sin \theta > \frac{\sigma_{LIQ}}{\rho g h_d} = \sin \theta_{crit} \quad (6-15)$$

Substituting values for the variables in Equation 6-15 from the conditions test run R2 and R3 gives the critical bed slope result (Equation 6-16).

$$\frac{1.97 \text{ Pa}}{1,190 \frac{\text{kg}}{\text{m}^3} 9.81 \frac{\text{m}}{\text{s}^2} 0.03 \text{ m}} = 0.0056 \quad (6-16)$$

This result compares within 15% of the measured average bed slope (Figure 6-11) of 0.0049. It should be noted that $h_d=0.03\text{m}$ is used when the actual computed h_d shown in Figure 6-7 is $h_d=0.02\text{m}$. This is intentional because h_d in the calculation represents the ‘average’ over the 400cm span of the trench. Since h_d is a function of wave height, H , h_d will be greater at locations closer to the front of the trench.

6.4 Model Application to Field Data

To demonstrate possible application of the results of this study, wave data collected by WAVCIS at the CSI3 measurement site during Hurricane Lili in 2002 was analyzed [WAVCIS, 2008]. The results are presented without proof since seabed data during a severe storm are not available, and because scaling between laboratory results versus field conditions is unknown. The measurements were made on 03 October 2002 at 1200 when Hurricane Lili was closest to the CSI3 site. Table 6-4 describes the measured wave conditions during this peak storm condition.

For similar wave conditions over a rigid or sandy seabed, the wave profile would be non-Gaussian with significant peaked crests and shallow troughs. The probability density function for the wave time series is presented in Figure 6-13. This function is surprisingly close to Gaussian with near symmetric peaks and troughs.

Figure 6-14 shows the magnitude of the horizontal velocity of the bed, $|u(z)|_{\max}$ as a function of bed depth. The velocity at $z'=0$ is equal to its horizontal value at the water column/bed surface interface (Eq. 5-17) that satisfies the boundary condition at that interface. Motion in the bed significantly dampens within the top 1 m demonstrating the high dissipation in AD Mud.

Figure 6-15 shows the shear stress profile in the bed. From these data, the transitioned depth, $h_d = 0.58$ m, is determined by the intersection of this profile with the shear stress at transition, σ_{LIQ} , from Equation 4-18. This implies that the top 0.58 m of the AD Mud bed became predominantly viscous under these hurricane waves.

Figures 6-16 and 6-17 show the real viscosity, $|\mu'|_{max}$, and total viscosity, $|\mu^*|_{max}$, profiles with depth in the bed, respectively and reflect the thixotropic properties of AD Mud with the viscosities increasing non-linearly with depth. Of significance is the large range of viscosities within the top 1m of the bed. Both the real viscosity, $|\mu'|_{max}$, and total viscosity, $|\mu^*|_{max}$, values span over two orders of magnitude. These results demonstrate that the description of viscosity, which is influenced by wave forcing, can not be simplified down to a single value for analysis.

Figure 6-18 shows incremental wave energy dissipation as a function of depth in the bed. The area to the left of the curve is equal to the total wave energy flux dissipation rate, ε_D per wave period. For this wave condition, $\varepsilon_D = 17.13 \frac{J}{m^2 s}$. Considering the log scale of ε_D , it is evident that the majority of the wave energy flux is dissipated within the top 0.20 m of the mud bed. Within the top 0.58 m of the bed, (which is the transitioned thickness) nearly all the wave energy dissipation takes place.

The temperature rise within the predominantly viscous transitioned thickness of the bed for Hurricane Lili based on Equation 5-42 is shown by Equation 6-17.

$$\Delta T(^{\circ}C) = 17.13 \frac{J}{m^2 \cdot s} \frac{2\pi}{0.573 \frac{1}{s} 3,100 \frac{J}{kg \cdot ^{\circ}C} 1200 \frac{kg}{m^3} 0.025m} = 2.0 \times 10^{-3} {}^{\circ}C \quad (6-17)$$

The layer thickness value, δ_T , used in Equation 6-16 was determined from Figure 6-14 as the thickness of large velocity gradient condition since this will be the location of greatest friction and heat energy conversion.

6.5 Topset Bed Slope Analysis

Adopting the bed slope analysis approach described in Section 6.3 for the wave flume conditions, preliminary analysis is performed for the Hurricane Lili conditions. Figure 6-19 shows the bathymetry at the topset. Though the average bed slope is 0.0001, the bathymetry shows what appears to be escarpment features. Three escarpments are seen evenly spaced along the outer 20 km length of the topset. The relief between the high and low points of these roughly 7 km long features is approximately 0.5 m.

It is possible that at this outer topset location, high bottom shear stresses generate significant momentum flux into the bed resulting in bed transition and net transport of the predominantly viscous material. When calmer sea state returns, gravity-induced turbidity flow settles the advected material at its angle of repose resulting in an equilibrium cross-bottom profile.

The face of the escarpment has a slope of 0.0003 (Figure 6-19). This will be the slope used in the momentum balance based on Equation 6-11. Substituting values for the variables in Equation 6-14 for Hurricane Lili gives the critical bed slope shown by Equation 6-16. Since actual bed conditions were not known, the density of the predominantly viscous layer was taken as approximately the density of the 0th order aggregate density, $\rho=1,200 \frac{\text{kg}}{\text{m}^3}$. From the data presented in Figure 4-43, $\sigma_{LIQ}=2.2 \text{ Pa}$.

$$\frac{2.2 \text{ Pa}}{1,200 \frac{\text{kg}}{\text{m}^3} 9.81 \frac{\text{m}}{\text{s}^2} 0.58 \text{ m}} = 0.00032 \quad (6-16)$$

This result compares within 7% of the measured slope of the escarpment at 0.0003. It should be noted that $h_d=0.58$ m was used in this calculation with the assumption that this thickness is of 0th order aggregate density. The justification that the top 0.58 m of the mud bed exists at this density is based on the hypothesis that significant near-bed transport took place during this storm event which advected sediment shoreward along the topset building up the already transitioned top layer of the bed. As a result, the density of the transported sediment would be similar to the transitioned top layer with both around the density of the 0th order aggregates, $\rho=1,200$ kg/m³.

Table 6-1. Wave flume test run parameters.

Test Run	Wave Angular Freq. (rad/s)	Wave Height (m)	Test Run	Wave Angular Freq. (rad/s)	Wave Height (m)
R1	4.02	0.0254	PER4	5.34	0.0144
R2	4.02	0.0560	POR4	5.38	0.0146
R3	4.21	0.0504	PER3	5.34	0.0190
R4	4.52	0.0708	POR2	7.36	0.011
R5	4.84	0.0646	PER5	7.35	0.014
PER1	5.34	0.0108	PER2	7.29	0.015
POR3	5.36	0.012	POR5	7.34	0.015
POR1	5.34	0.0124			

Water Depth = 0.19 m

Bed Thickness = 0.08 m

Test Run Legend: PERx – Test conducted on initial 2.5 day consolidated bed

Rx – Test conducted immediately following PERx run to steady state

PORx – Test conducted immediately following Rx run to steady state

Table 6-2. Comparison of wave energy dissipation rates based on recent stress history.

Test Run	Measured ε_D (J/m ² s)	Model ε_D (J/m ² s)
PER4	0.0205	0.0259
POR4	0.0198	0.022

Table 6-3. Comparison of measured and model wave energy flux dissipation results.

Test Run	Measured ε_D (J/m ² s)	Model ε_D (J/m ² s)	Difference (%)
R1	0.0386	0.04	3.6
R2	0.26	0.248	5.1
R3	0.249	0.262	5.3
R4	0.394	0.416	5.7
R5	0.38	0.368	3.1

Table 6-4. Hurricane Lili wave condition.

Significant Wave Height	Water Depth	Wave Number	Zero Up-crossing Wave Period
H _s (m)	h (m)	k (1/m)	T (s)
2.76	5.80	0.0785	10.96

Hurricane Lili 10/3/2002, 1200 Measured data at location of WAVCIS CSI3

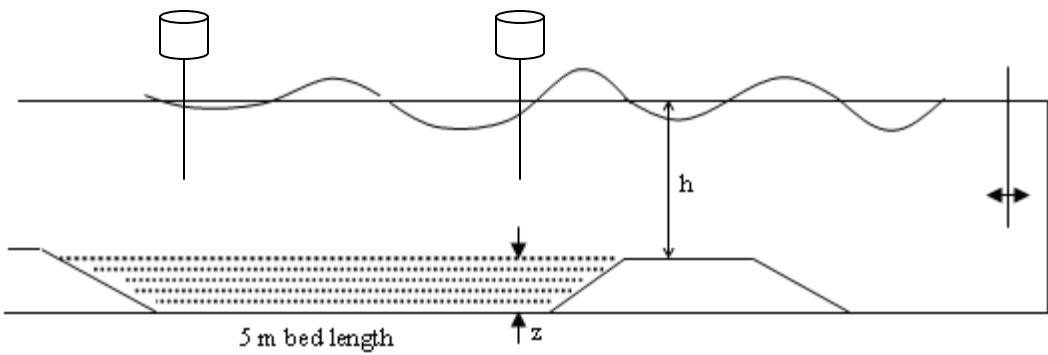


Figure 6-1. Schematic of wave flume wave maker, wave gauges and mud trench.



Figure 6-2. Photograph of wave flume and instrumentation at the Coastal Engineering Laboratory, University of Florida. Arrow indicates capacitance wave gauge.

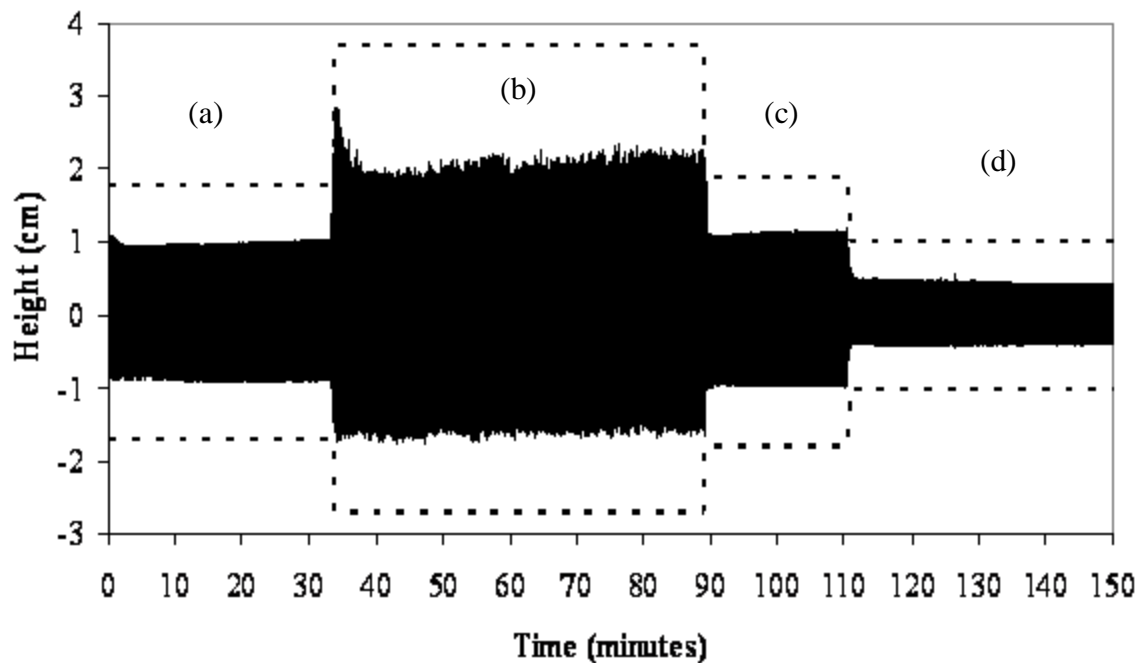
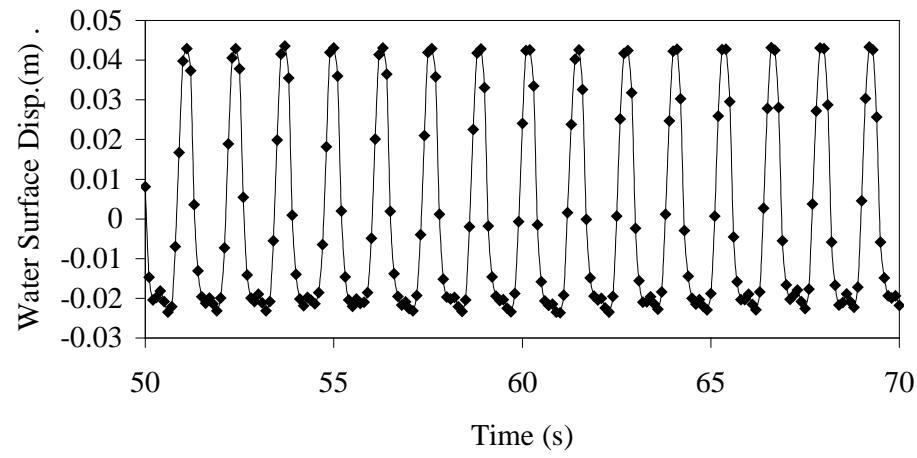
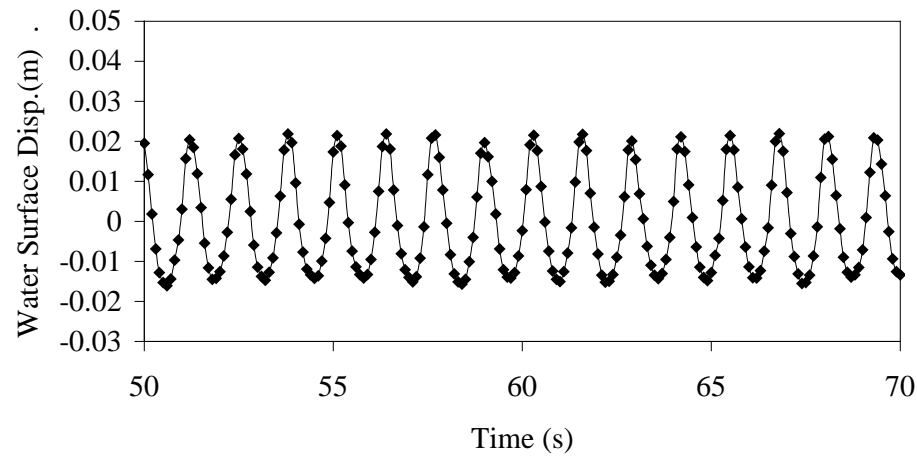


Figure 6-3. Continuous wave flume time series of water surface elevation. Test run sequence –
 (a): $H_0=3.5$ cm, $H_x=1.87$ cm, $\omega=7.39$ rad/s, (b): $H_0=6.4$ cm, $H_x=3.8$ cm, $\omega=5.24$ rad/s,
 (c): $H_0=3.7$ cm, $H_x=2.08$ cm, $\omega=7.39$ rad/s, (d): $H_0=2.0$ cm, $H_x=0.87$ cm, $\omega=5.24$
 rad/s. Dashed lines:wave envelope, H_0 , at front of trench. Solid section:wave
 envelope, H_x at back of trench. Water depth, $h=0.19$ m.

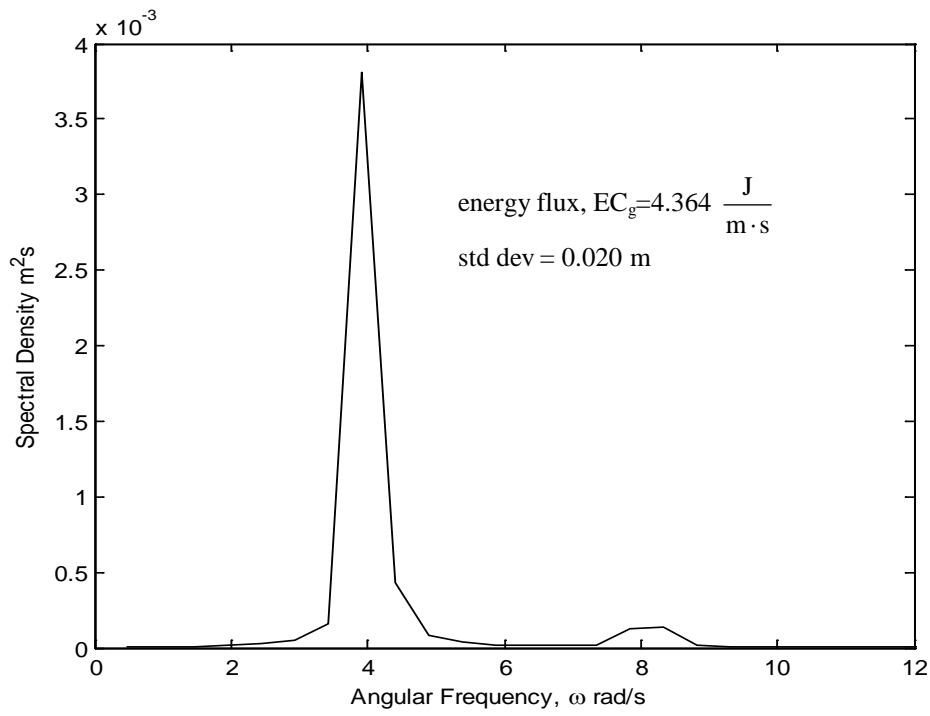


(a)

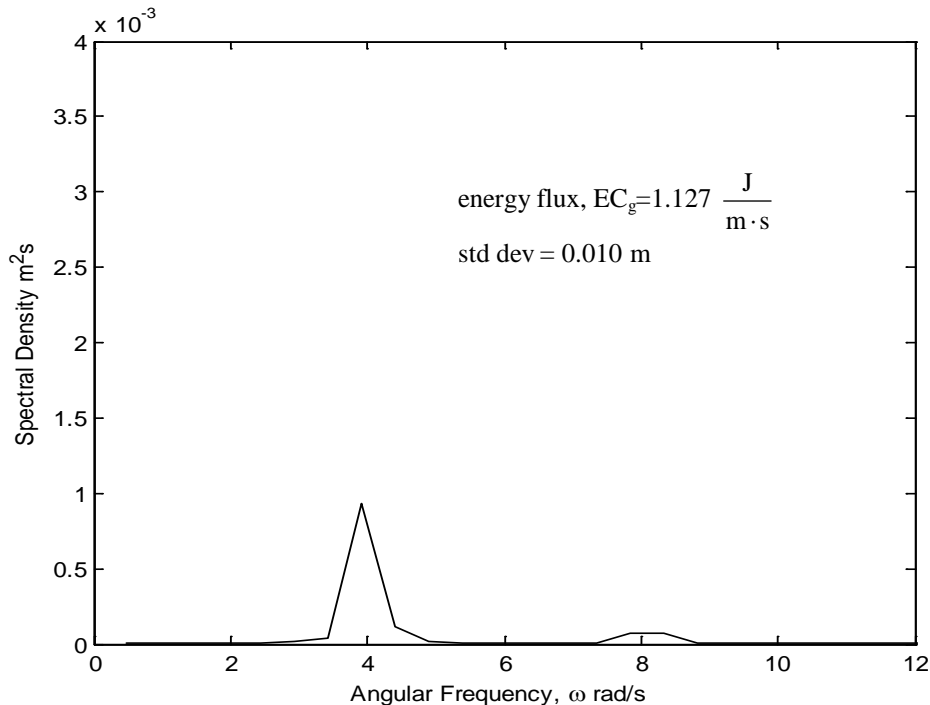


(b)

Figure 6-4. Surface elevation data from Test Run R2. (a) Data at front of trench, (b) Data at back of trench.



(a)



(b)

Figure 6-5. Spectral density function for Test Run R2. (a) Wave energy at front of trench, (b) Wave energy at back of trench.

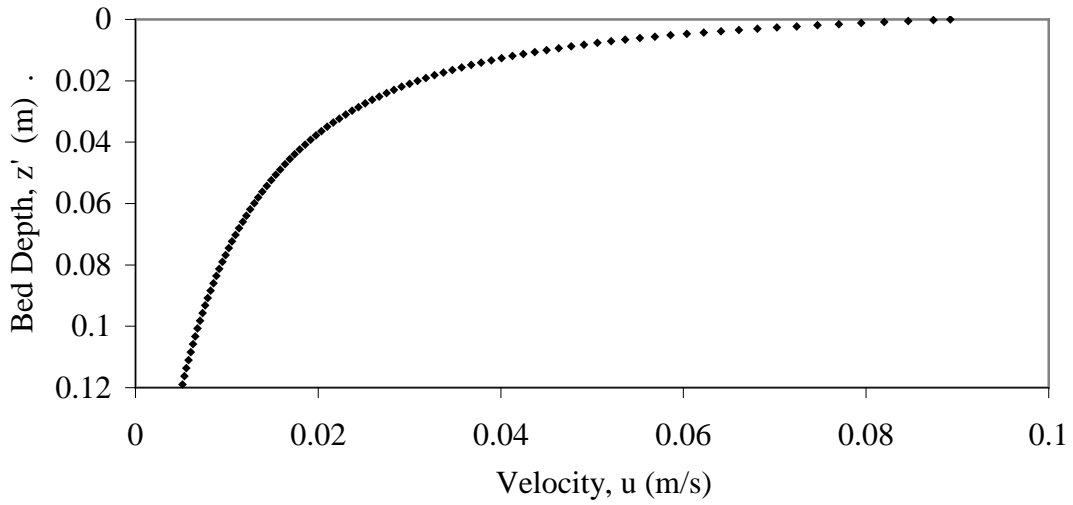


Figure 6-6. Horizontal velocity profile as a function of bed depth for Test Run R2.

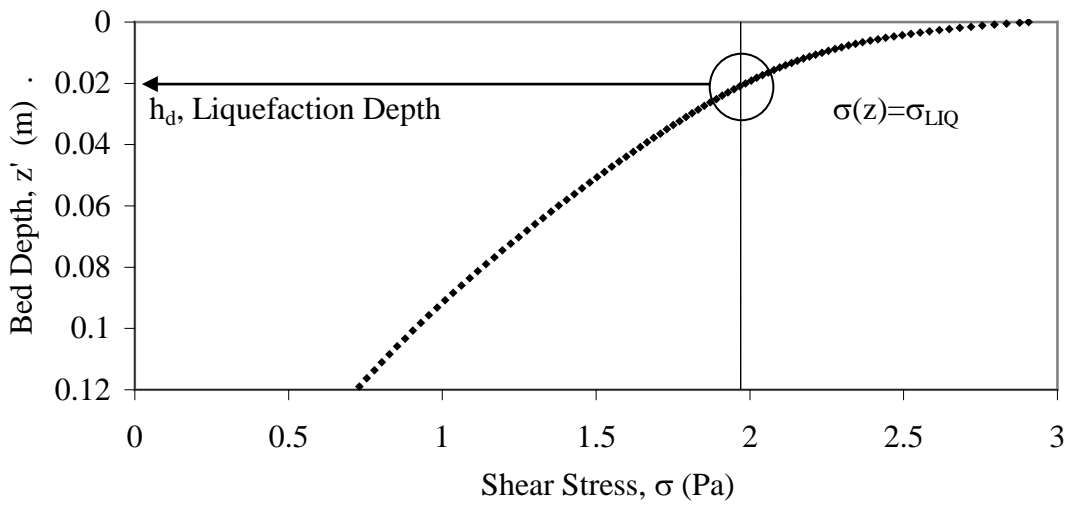


Figure 6-7. Shear stress profile as a function of bed depth for Test Run R2. Transitioned depth, h_d , determination.

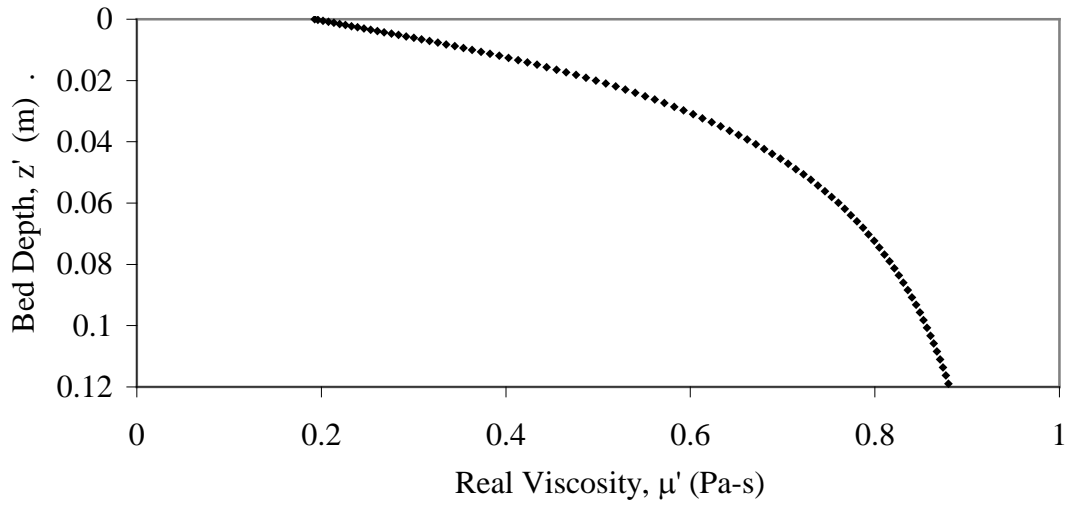


Figure 6-8. Real viscosity profile as a function of bed depth for Test Run R2.

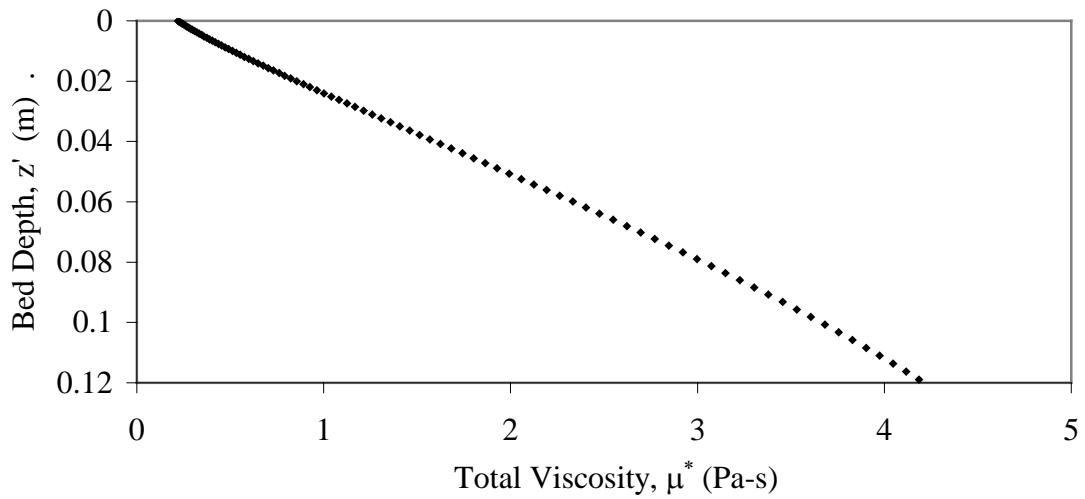


Figure 6-9. Total viscosity profile as a function of bed depth for Test Run R2.

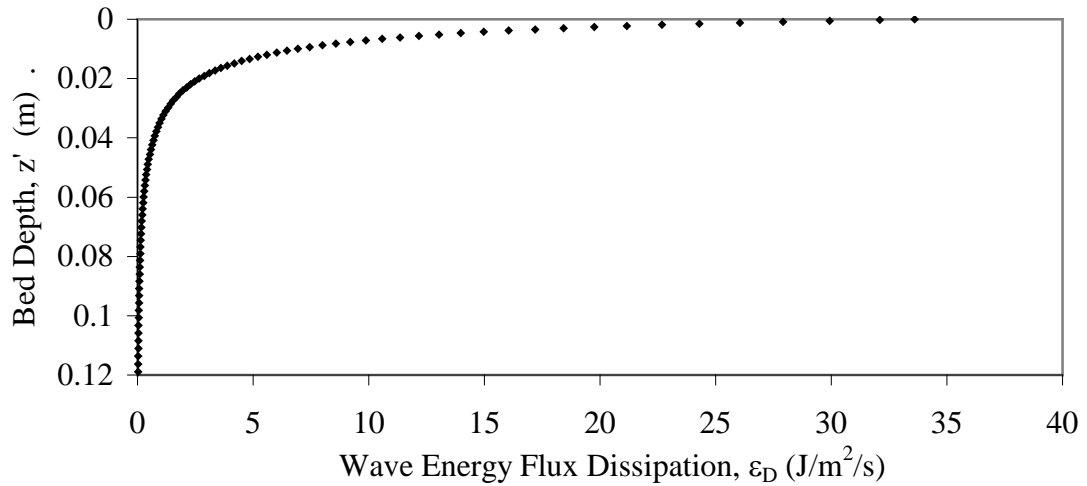


Figure 6-10. Wave energy flux dissipation profile as a function of bed depth for Test Run R2.

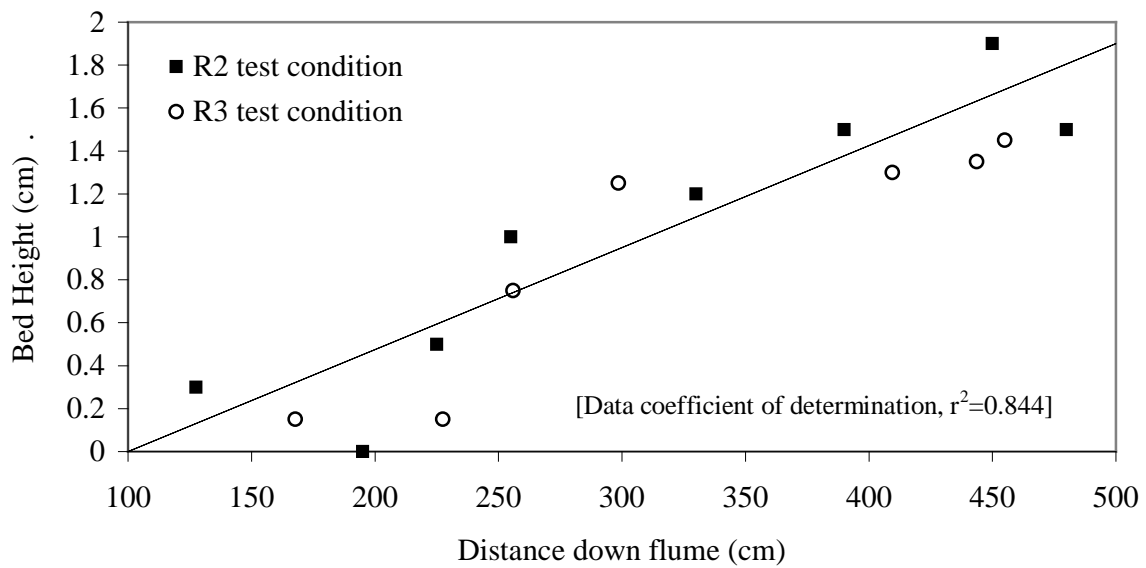


Figure 6-11. Settled bed elevation in trench measured after two similar test runs.

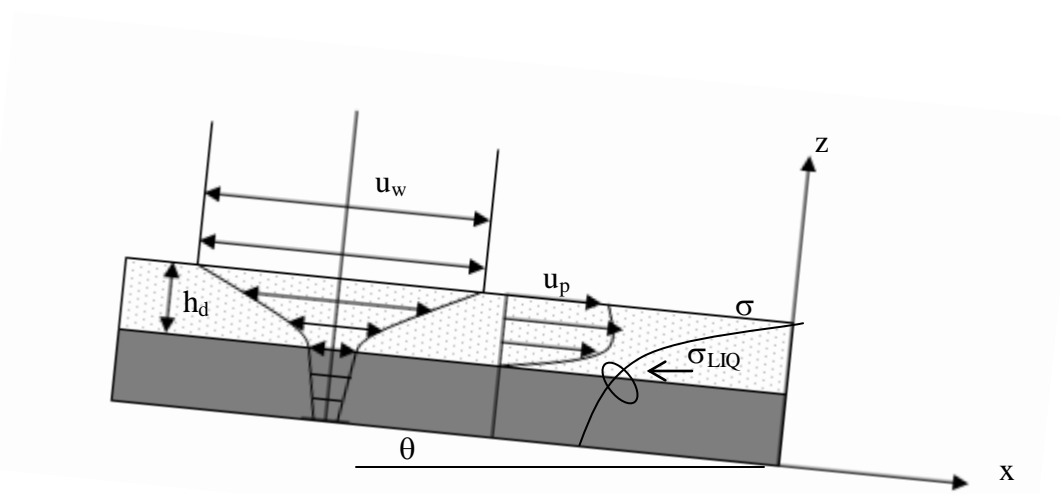


Figure 6-12. Definitional sketch of gravity-driven flow due to oscillatory flow. u_w -horizontal water velocity, u_p - flow velocity, h_d -depth of predominantly viscous flow layer, σ -bed shear stress, σ_{LIQ} -transition shear stress, θ -angle of bed slope.

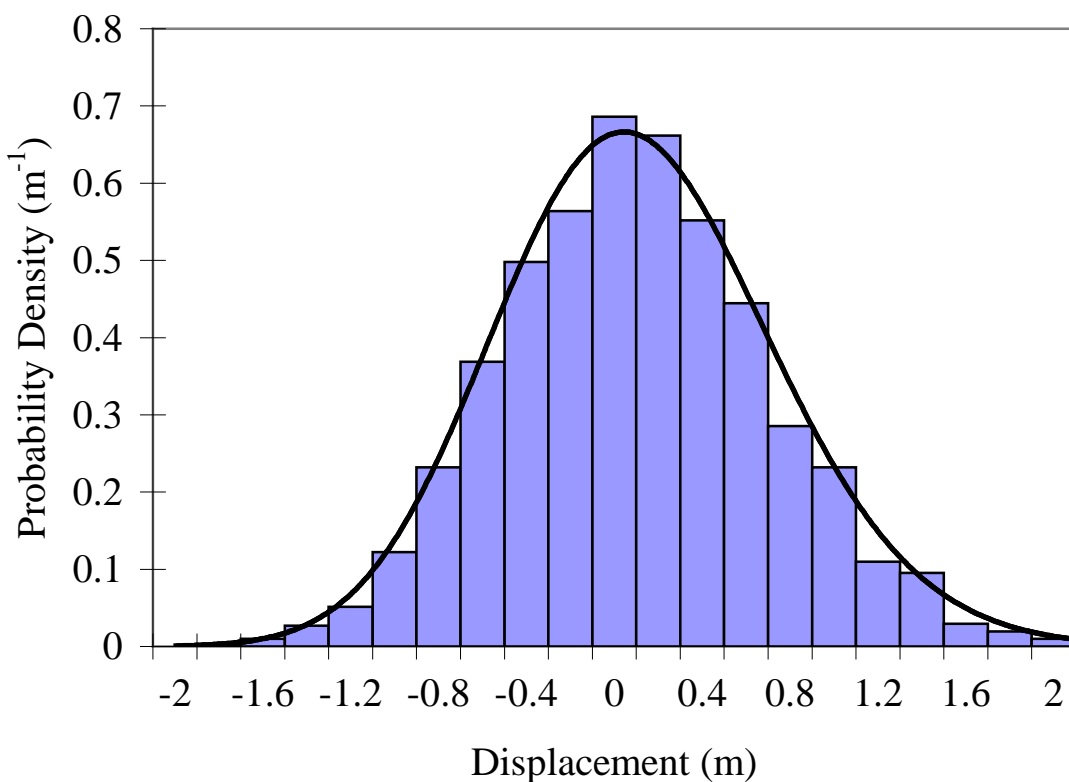


Figure 6-13. Probability density function of wave condition at WAVCIS CSI3 during Hurricane Lili at 10/3/2002, 1200. (Data Source: <http://wvcis.csi.lsu.edu/> last accessed October 2007)

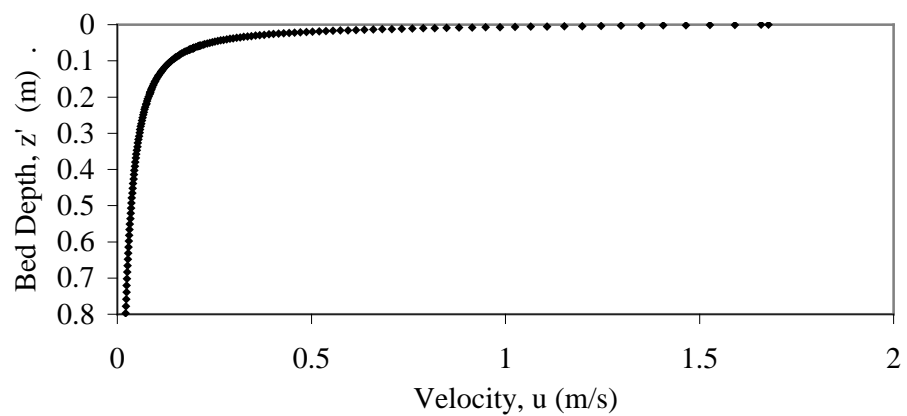


Figure 6-14. Horizontal velocity profile as a function of bed depth for Hurricane Lili 10/3/2002, 1200 wave conditions at WAVCIS CSI3.

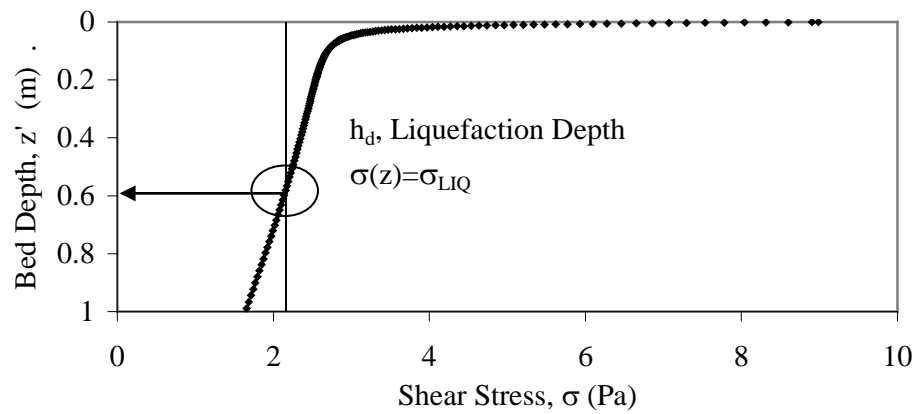


Figure 6-15. Shear stress profile as a function of bed depth and transitioned depth, h_d , for Hurricane Lili 10/3/2002, 1200 wave conditions measured at WAVCIS CSI3.

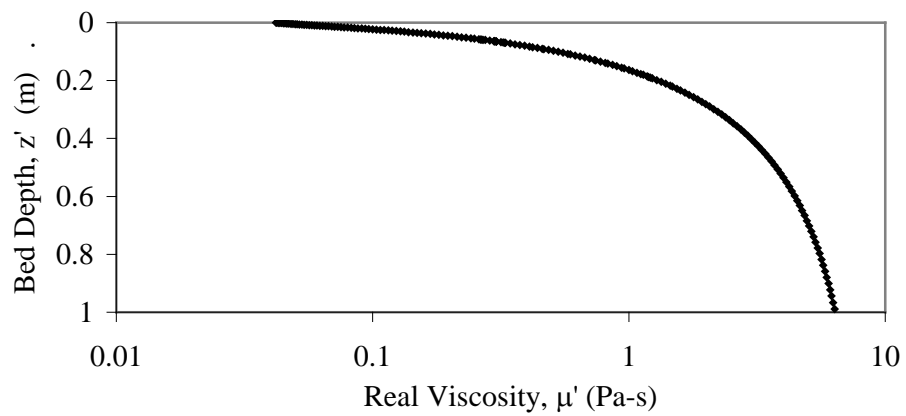


Figure 6-16. Real viscosity profile as a function of bed depth for Hurricane Lili 10/3/2002, 1200 wave conditions at WAVCIS CSI3.

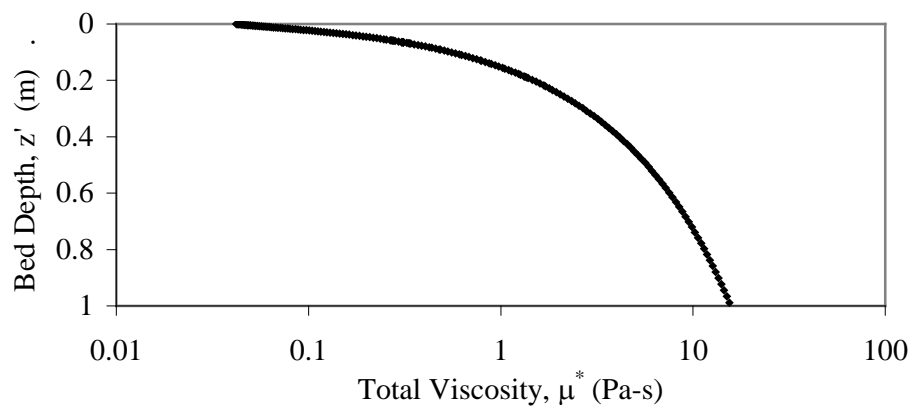


Figure 6-17. Total viscosity as a function of bed depth for Hurricane Lili 10/3/2002, 1200 wave conditions at WAVCIS CSI3.

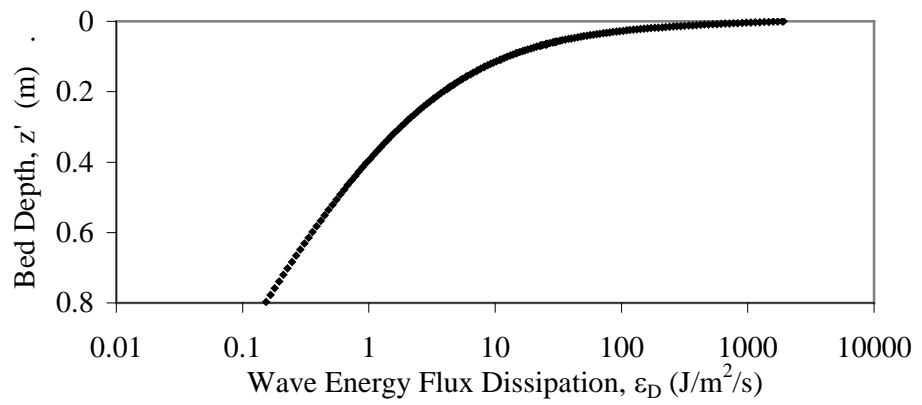


Figure 6-18. Wave energy dissipation as a function of bed depth for Hurricane Lili 10/3/2002, 1200 wave conditions at WAVCIS CSI3.

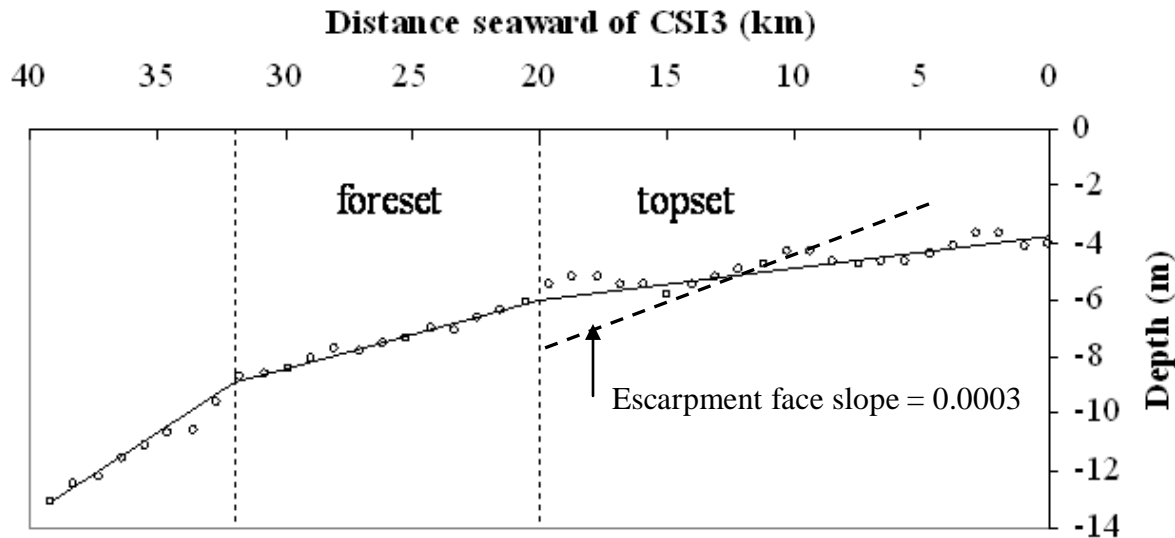


Figure 6-19. Clinofornt bed profile seaward of CSI3 site shown in Figure 2.4 with slope of escarpment face defined.

CHAPTER 7 SUMMARY AND CONCLUSIONS

*“Large aggregates have little aggregates which fill their void capacity
And little aggregates have lesser aggregates ever increasing tortuosity
The aggregates have other aggregates set on top to crush ‘em
While these en masse define the seabed that rests on solid stratum.”*

7.1 Summary

Hydrodynamic models of wave-mud interaction meant to estimate surface wave attenuation require a description of the rheology of the mud bed. An important bottom parameter is the thickness of the oscillating fluid mud layer participating in the attenuation processes since most wave energy is attenuated within this layer. Conventionally a model is tuned with respect to the bottom thickness which produces the measured wave damping. This requirement limits the model's ability to predict wave damping and has led to the need to determine the oscillating mud thickness from analysis that is independent of measured wave damping.

The objective of this study was to determine the thickness of the oscillating mud layer from a rheological assessment of the behavior of mud subjected to oscillatory shear stress representative of surface wave forcing. A wave flume study was undertaken using seabed sediment collected from the outer topset region of the Atchafalaya River Delta in the Gulf of Mexico. The AR 2000ex Rheometer was used to test the dynamic response of the AD Mud. The thickness of the predominantly viscous oscillating fluid mud layer was identified from the condition that the shear stress within the layer is equal to the yield strength of mud at the base of the predominantly viscous layer.

The tasks of this study included:

- Determination of the relevant properties of AD Mud to select the appropriate rheological testing and analysis protocols.
- Settling and self-weight consolidation tests of AD Mud to ensure repeatable bed preparations for the flume tests and to determine the density profile of the flume bed.

- Derivation of a flow equation of mud based on its measured dynamic response.
- Development of a set of model equations for determination of profiles within the fluid mud bed of the horizontal velocity, the rate of strain, the bed shear stress, the transitioned depth and the wave energy dissipation rate.
- Validation of the model from flume test results on wave damping and bed oscillation.
- Discussion of the above analysis relative to episodic waves and bottom conditions in the Atchafalaya Delta region.

7.2 Observations

The following observations have been made:

- The AD Mud seabed substantially stabilizes (as indicated by measured viscosity) within tens of minutes after a change in the imposed shear stress. However, due to the thixotropic property (i.e., time-dependent rheology) of this mud, the viscosity does not achieve a truly constant value for several hours. Also, due to thixotropy the stress history plays a key role in determining the final state of the mud.
- Under an imposed wave-induced shear stress at the mud surface, waves are attenuated less when the preceding shear stress is higher than the imposed stress, in contrast with the case when the preceding stress is lower than the imposed stress.
- At high wave induced shear stresses, mud viscosity was found to vary by more than two orders of magnitude, and the bed behaved simultaneously as an elasticoviscous, viscoelastic and purely viscous material depending on depth within the bed.
- The mud strength (marking the threshold of transition) increases rapidly with bed density once it exceeds the density of a bed comprised of zero-order particle aggregates (as defined by Krone).
- The shear stress required to induce transition depends primarily on the solids volume fraction of the bed and to a lesser degree on wave forcing.
- Measured and predicted thicknesses of the predominantly viscous oscillating bed are shown to compare within 6%. This agreement points to the potential for the applicability of the developed method for use in the field, as shown by the application to data from Hurricane Lilli.

7.3 Recommendations for Future Studies

Specific recommendations include:

- Consideration of the inclusion of normal pressure force, e.g. under a standing or partially standing wave, and when waves occur in intermediate water depths.
- Investigation of how the stochastic properties of narrow-band sea spectra influence mud rheology. The approach of this study was based on linear wave theory and monochromatic waves. How wave frequency components collectively influence the mud bed is of interest to model wave conditions in the field.
- Mud mass transport was observed qualitatively during the flume tests. Development of a second-order model to quantify mass transport would shed light on the advective response of the predominantly viscous mud to waves.

APPENDIX A DETERMINATION OF MUD FLOW CURVE PARAMETERS

A.1 Wave and Mud Bed Property Ranges

This appendix discusses the procedure for determining the rheology-based flow curve equations defined by Equations 4-8 to 4-12. The procedure and data sets provided by this analysis enable the estimation of the shear stress–rate of strain relationship for oscillatory flow conditions between $\left[0.628 \frac{\text{rad}}{\text{s}} \leq \omega \leq 5 \frac{\text{rad}}{\text{s}} \right]$ occurring within a normally consolidated AD Mud having concentrations between $[0.054 \leq \phi_{\text{VS}} \leq 0.214]$. These limits encompass the range of conditions typically encountered in the Gulf of Mexico and the range of AD Mud solids volume fraction typically expected in the active, upper seabed layers of the outer topset Atchafalaya Delta.

As discussed in Chapter 4, the values of four AD Mud properties, μ'_{INF} , μ'_{LEV} , $\sin\delta_{\text{LEV}}$, and γ_{LIQ} , must be defined in order to complete the solution. For that purpose, the stress history of the specific boundary value problem sought must be determined. This is because recent stress history has been shown to influence the properties of the AD Mud seabed due to its thixotropic property. The stress history is distinguished for severe or mild depending on if the wave induced shear stress at the water-mud bed interface was greater or less than the imposed shear stress, respectively.

A.2 Mild Stress History

For applications when the wave condition of interest is at least as severe as the wave condition of the previous 24-48 hours, the values of the four AD Mud properties, μ'_{INF} , μ'_{LEV} , $\sin\delta_{\text{LEV}}$, and γ_{LIQ} , may be determined by using the data from the rheological tests based on an

increasing shear stress protocol. The data presented for the mild stress history would be appropriate to use for analysis of the ‘normal’ wave condition or the condition leading up to and including a large wave event. The data shown in Figures A-1 through A-3 present data on the viscosity at infinite rate of strain which has been shown to be independent of stress history.

A.2.1 Viscosity at Infinite Rate of Strain, μ'_{INF}

Since μ'_{INF} is independent of stress history the same data is used for both mild and severe stress history scenarios. It is understandable that this property should not depend on stress history since it represents the viscosity of AD Mud at ‘infinite’ rate of strain. This high rate of strain causes the mud to completely break down, thus erasing any stress history effect. The viscosity does however depend on the solids volume fraction, ϕ_{vs} , of the mud (Figure A-1) and the angular frequency, ω , of the oscillatory shear stress (Figure A-2). Viscosity increases with increasing solids volume fraction and angular frequency. Figure A-3 presents a contour plot which can be used to determine the μ'_{INF} value for given ω and ϕ_{vs} .

A.2.2 Viscosity in Linear Elasticoviscous (LEV) Region, μ'_{LEV}

The data shown in Figures A-4 through A-10 represents results measured under more mild stress history conditions.

μ'_{LEV} represents the dynamic viscosity of AD Mud under low rates of strain where the mud maintains its structural integrity and its behavior is more elastic than viscous. The value of this viscosity depends on the stress history as well as on ϕ_{vs} and ω . Its dependence on ϕ_{vs} and ω shown by Figures A.4 and A.5, respectively. Figure A-6 provides a contour plot where the value of μ'_{LEV} for a particular ϕ_{vs} and ω can be determined. μ'_{LEV} increases with increasing solids volume fraction and decreases with increasing angular frequency.

A.2.3 Sine of the Phase Angle in Linear Elasticoviscous (LEV) Region, $\sin\delta_{LEV}$

$\sin\delta_{LEV}$ represents the integrity of structure in AD Mud under low rates of strain. As shown in Figures A-7 and A-8, this phase angle does not vary significantly across the ranges of ϕ_{vs} and ω . Since in the LEV region, the mud remains structurally intact, the lack of dependence on ϕ_{vs} and ω would be expected. It may be assumed that for mild pre-stress conditions that $\sin\delta_{LEV}=0.18$. This low value implies strong elastic behavior. Under more severe pre-stress conditions, this quantity is also independent of ϕ_{vs} and ω but is greater than 0.18.

A.2.4 Rate of Strain at Transition, γ_{LIQ}^{\square}

γ_{LIQ}^{\square} is the rate of strain which causes failure of the structure of AD Mud. It represents the location where the flow curve experiences a point of inflection. This location on the flow curve is also where $\mu'=\mu''$. Figure A-9 shows that γ_{LIQ}^{\square} is independent of ϕ_{vs} while Figure A-10 shows a dependence of γ_{LIQ}^{\square} on ω . For mild pres-stress conditions, this relationship can be described empirically as Equation A-1.

$$\gamma_{LIQ}^{\square} = 0.614\omega^{0.82} \quad (A-1)$$

A.3 Severe Stress History

For applications when the wave condition is less severe than the wave condition of the previous 24-48 hours, the four AD Mud properties, μ'_{INF} , μ'_{LEV} , $\sin\delta_{LEV}$, and γ_{LIQ}^{\square} , may be determined from the rheological test data which follow a decreasing shear stress protocol. During these tests, the mud was subjected to high shear stress (or rate of strain) conditions initially, then the shear stress was reduced as the test continued.

A.3.1 Viscosity at Infinite Rate of Strain, μ'_{INF}

μ'_{INF} is independent of stress history and is therefore the same for both mild and severe stress histories. Figure A-3 presents a contour plot which can be used to determine the μ'_{INF} value for given ω and ϕ_{vs} .

A.3.2 Viscosity in Linear Elasticoviscous (LEV) Region, μ'_{LEV}

μ'_{LEV} represents the dynamic viscosity of AD Mud under low rates of strain where the mud maintains its structural integrity and its behavior is more elastic than viscous. The value of this quantity depends on the stress history as well as on ϕ_{vs} and ω . Figures A-11 and A-12 show its dependence on ϕ_{vs} and ω , respectively. Figure A-13 provides a contour plot where the value of μ'_{LEV} for a particular ϕ_{vs} and ω can be determined. This viscosity increases with increasing solids volume fraction and decreases with increasing angular frequency.

A.3.3 Sine of the Phase Angle in Linear Elasticoviscous (LEV) Region, $\sin\delta_{\text{LEV}}$

The sine of the phase angle after a severe pre-stress condition follows the same general trend as the mild pre-stress condition. Figures A-14 and A-15 depict the relationship between $\sin\delta_{\text{LEV}}$ and ϕ_{vs} and ω , respectively. This quantity does not vary significantly across the ranges of ϕ_{vs} and ω . Since in the LEV region the mud remains structurally intact, the lack of dependence on ϕ_{vs} and ω would be expected. Based on the data presented in Figures A-14 and A-15, it may be assumed that a reasonable value for $\sin\delta_{\text{LEV}}$ under severe stress history is 0.30.

A.3.4 Rate of Strain at Transition, $\gamma_{\text{LIQ}}^{\square}$

For a severe pre-stress condition, $\gamma_{\text{LIQ}}^{\square}$, is dependent on ϕ_{vs} and ω as shown in Figures A-16 and A-17. As a result, a contour plot (Figure A-18) must be used to determine the rate of strain

at transition over the range of ϕ_{vs} and ω values tested. For a severe stress history, γ_{LIQ}^{\square} increases with increasing solids volume fraction and angular frequency.

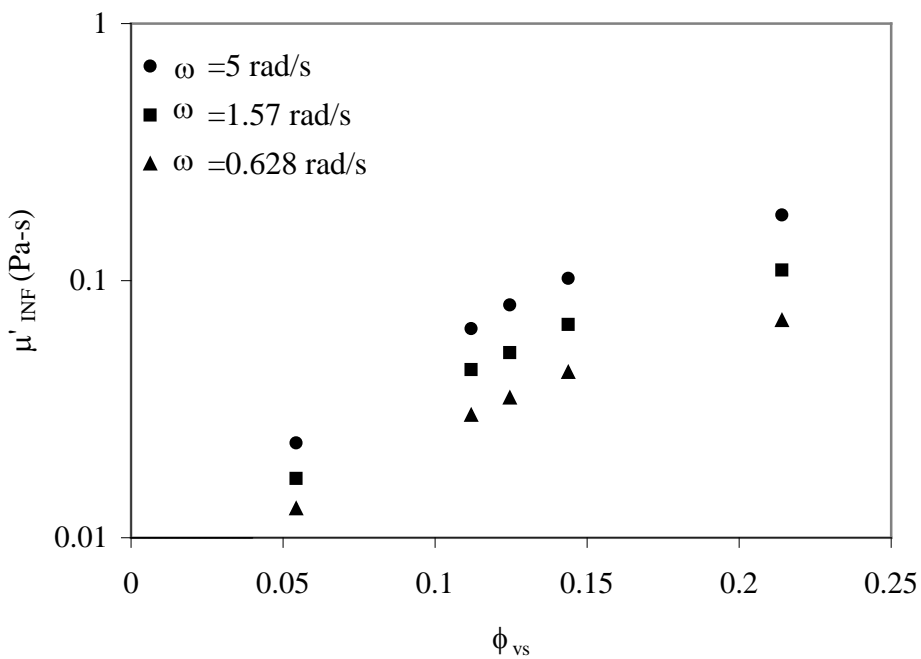


Figure A-1. Real viscosity at infinite rate of strain versus solids volume fraction.

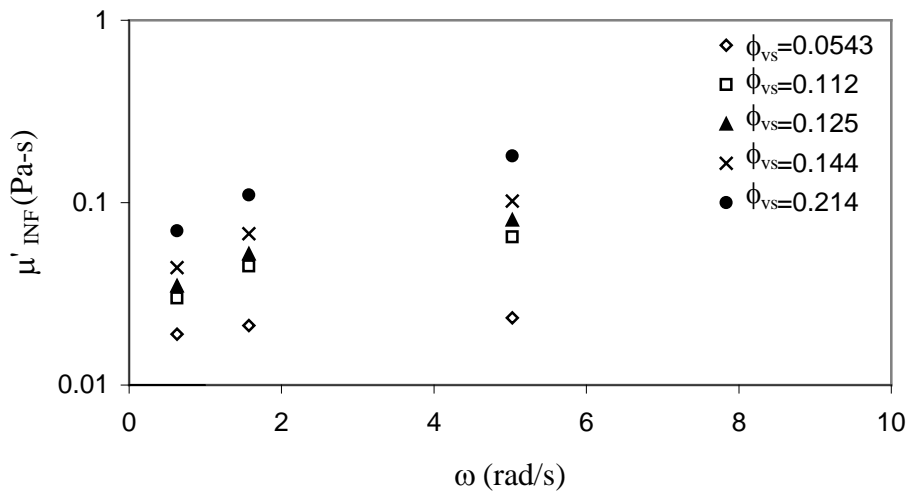


Figure A-2. Real viscosity at infinite rate of strain versus angular frequency of oscillatory flow.

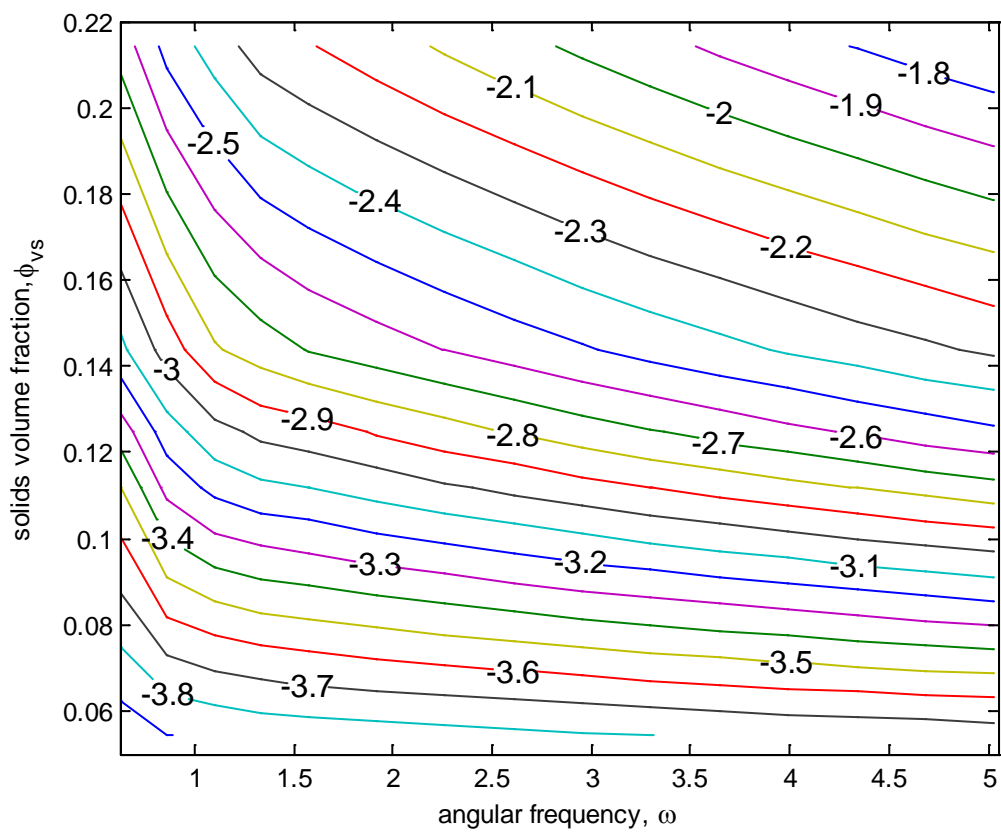


Figure A-3. Contour plot of $\ln(\mu'_{\text{INF}})$ as a function of solids volume fraction and angular frequency.

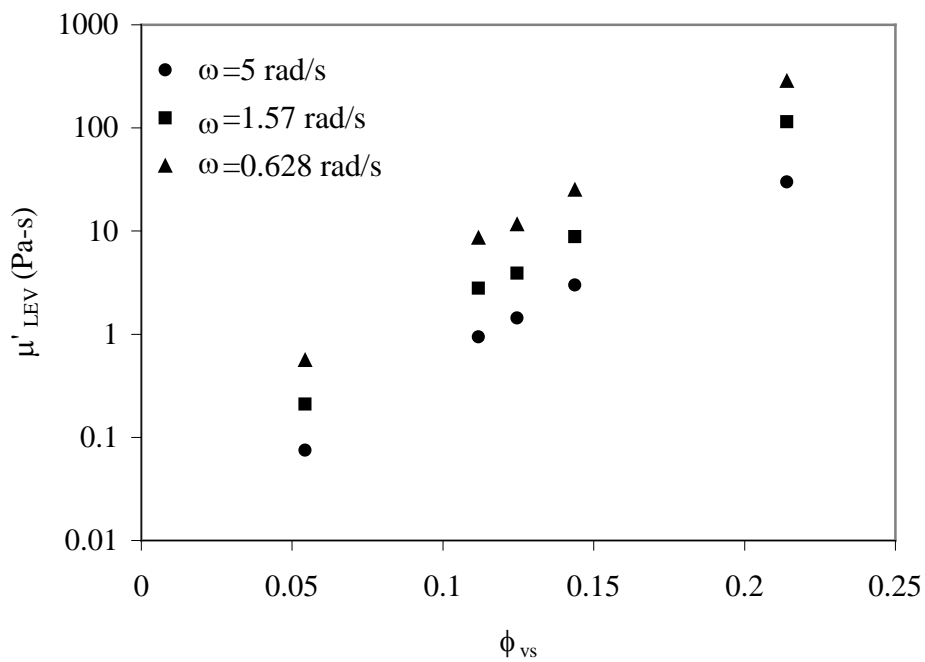


Figure A-4. Real viscosity in the linear elasticoviscous region versus solids volume fraction for mild stress history.

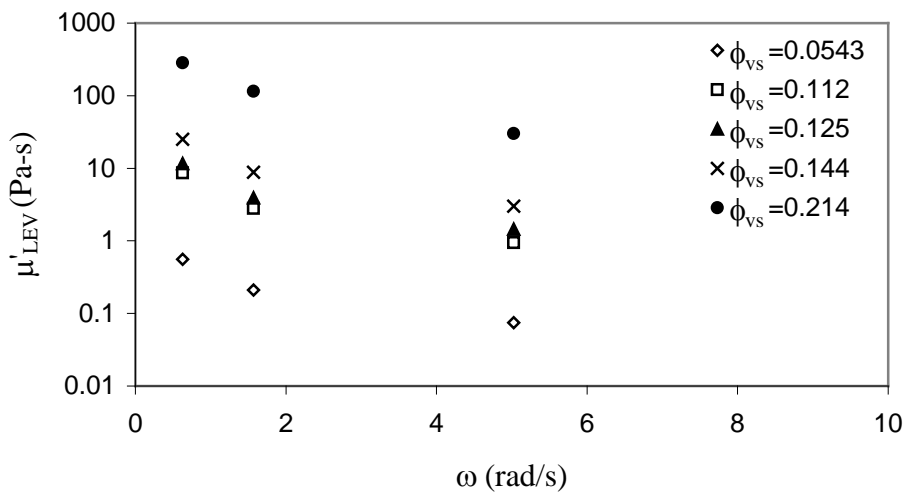


Figure A-5. Real viscosity in the linear elasticoviscous region versus angular frequency for mild stress history.

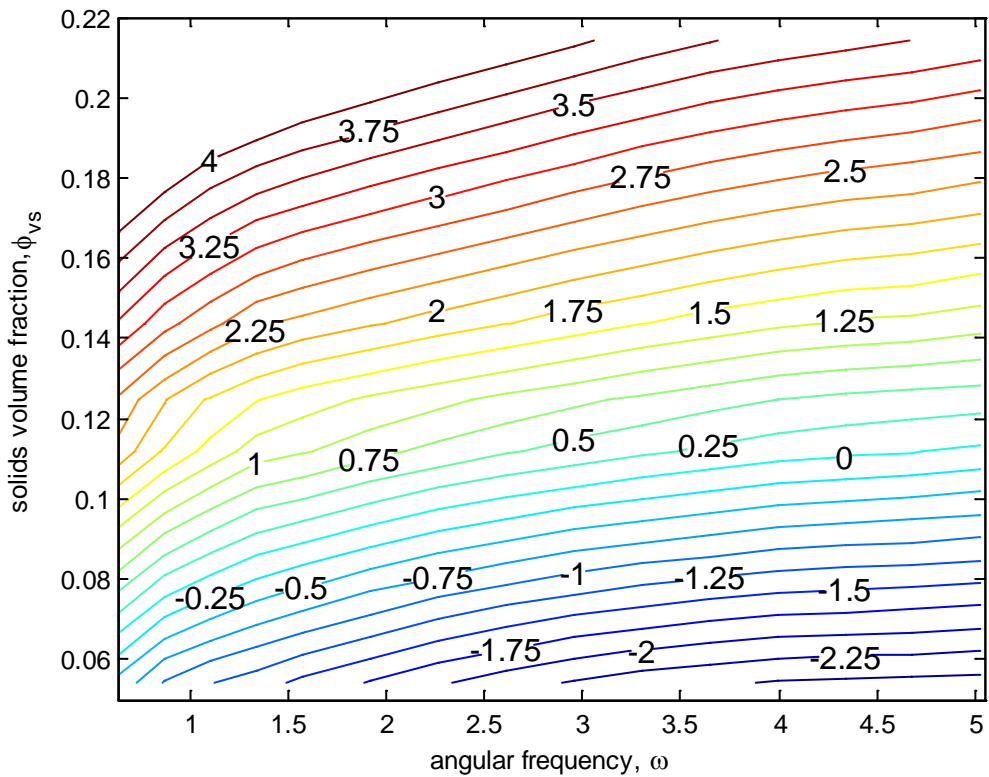


Figure A-6. Contour plot of $\ln(\mu_{\text{LEV}})$ for mild pre-stress condition as a function of ϕ_{vs} and ω .

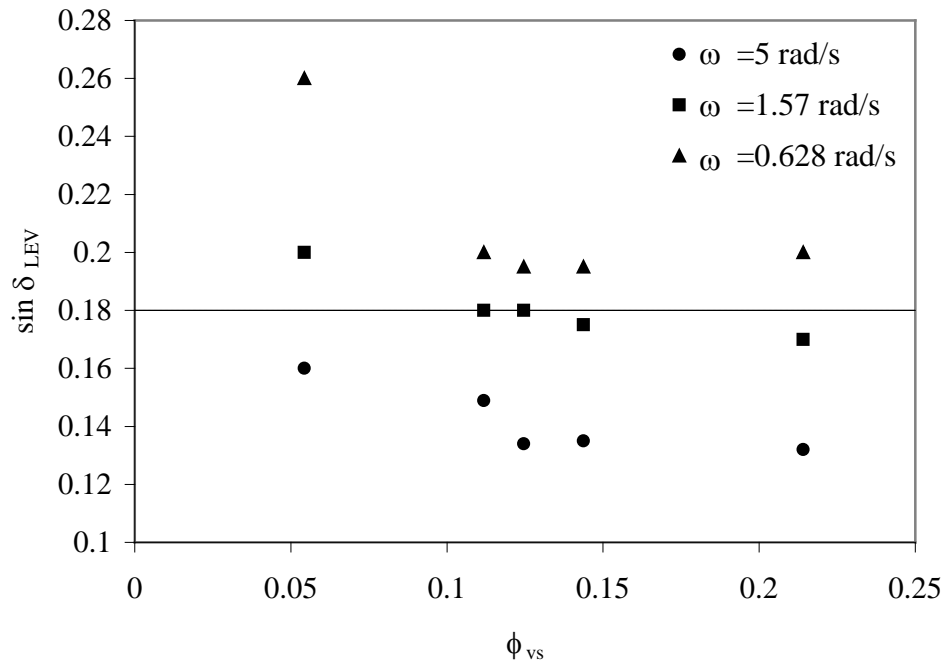


Figure A-7. Sine of phase angle in linear elasticoviscous region versus solids volume fraction for mild stress history.

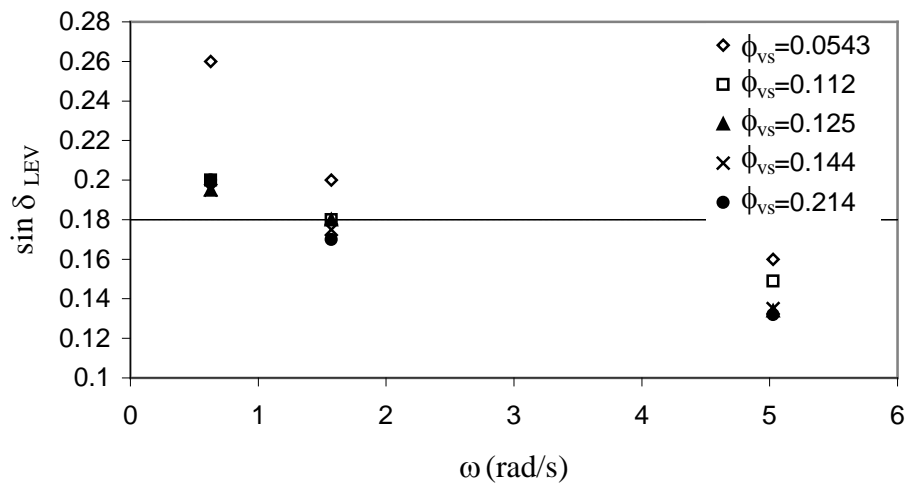


Figure A-8. Sine of phase angle in linear elasticoviscous region versus solids angular frequency for mild stress history.

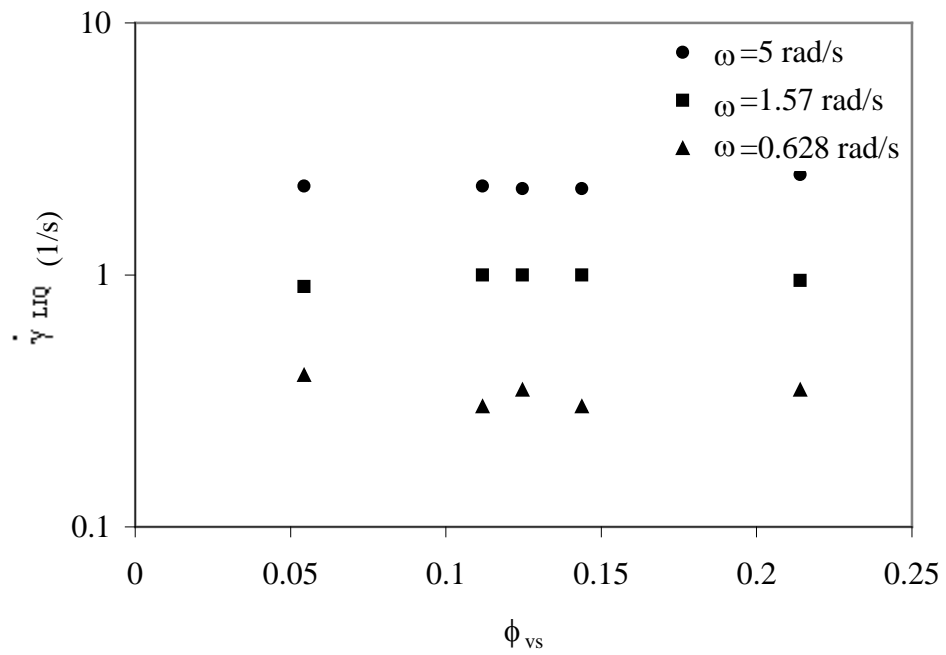


Figure A-9. Rate of strain at transition versus solids volume fraction for mild stress history.

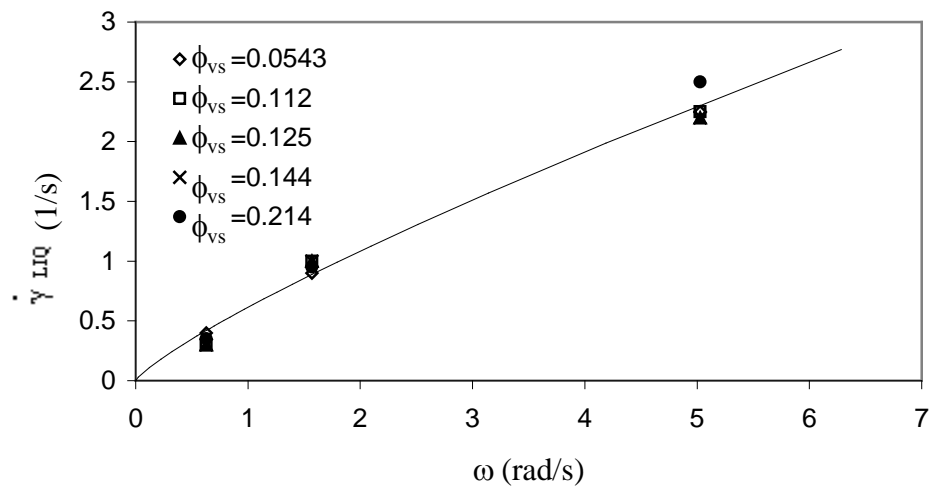


Figure A-10. Rate of strain at transition versus angular frequency for mild stress history with solid line depicting approximate empirical relationship shown by Eq. A-1.

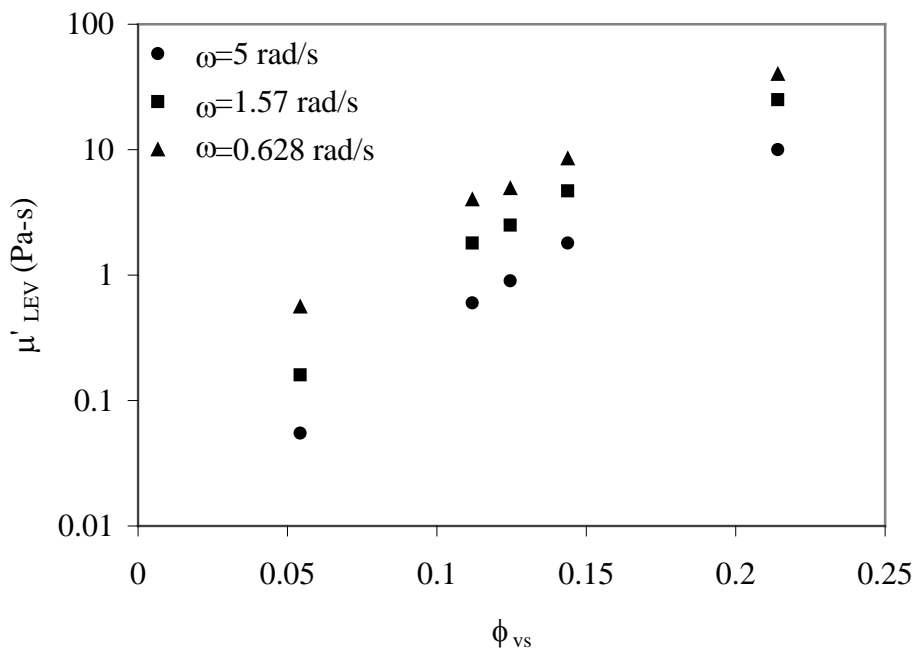


Figure A-11. Real viscosity in the linear elasticoviscous region versus solids volume fraction for AD Mud for severe stress history.

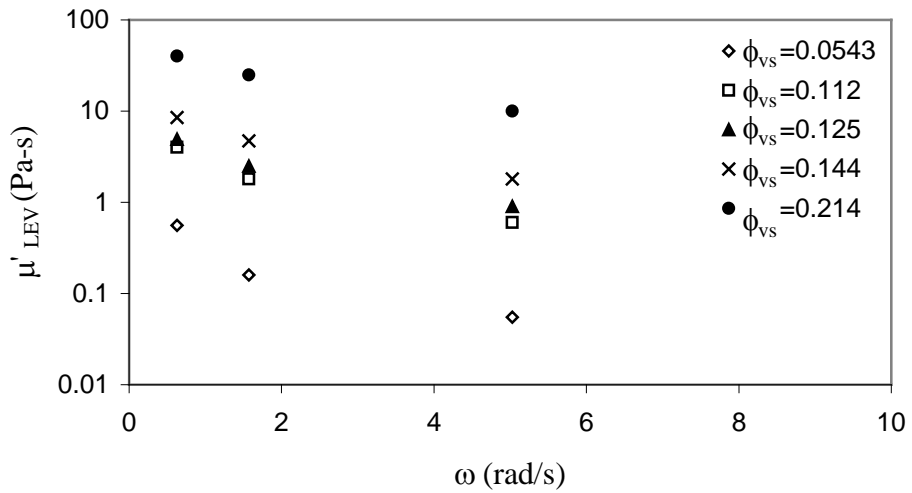


Figure A-12. Real viscosity in the linear elasticoviscous region versus angular frequency for AD Mud for severe stress history.

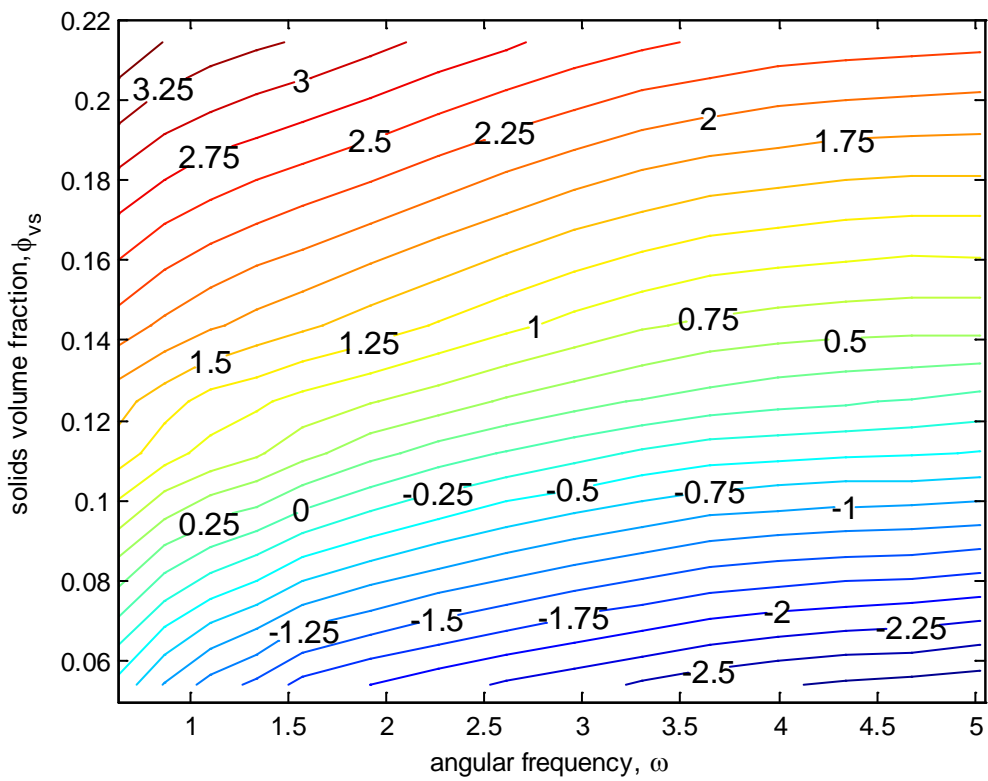


Figure A-13. Contour plot of $\ln(\mu_{LEV})$ as a function of solids volume fraction and angular frequency for severe stress history.

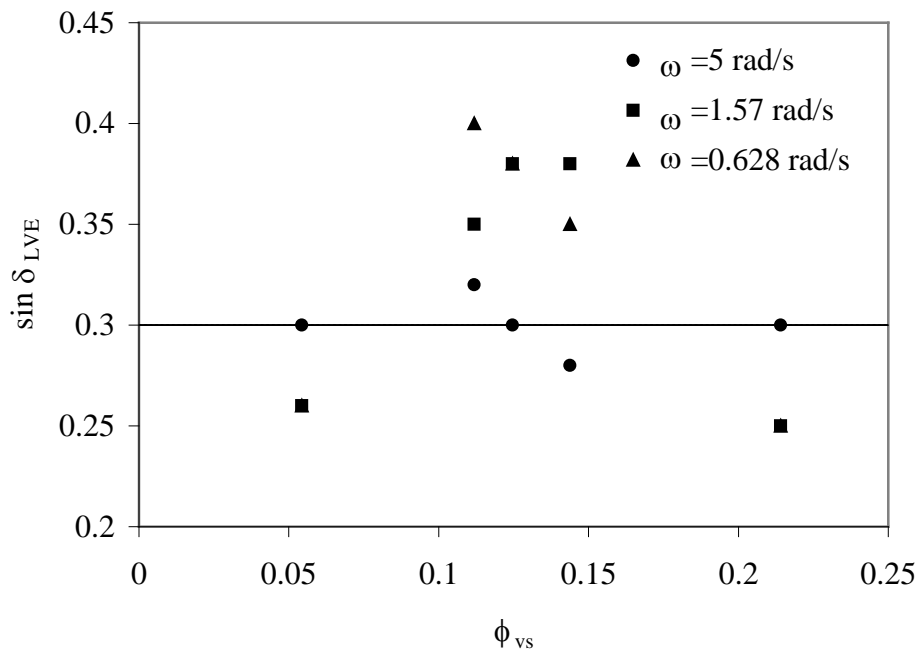


Figure A-14. Sine of phase angle in linear elasticoviscous region versus solids volume fraction for severe stress history.

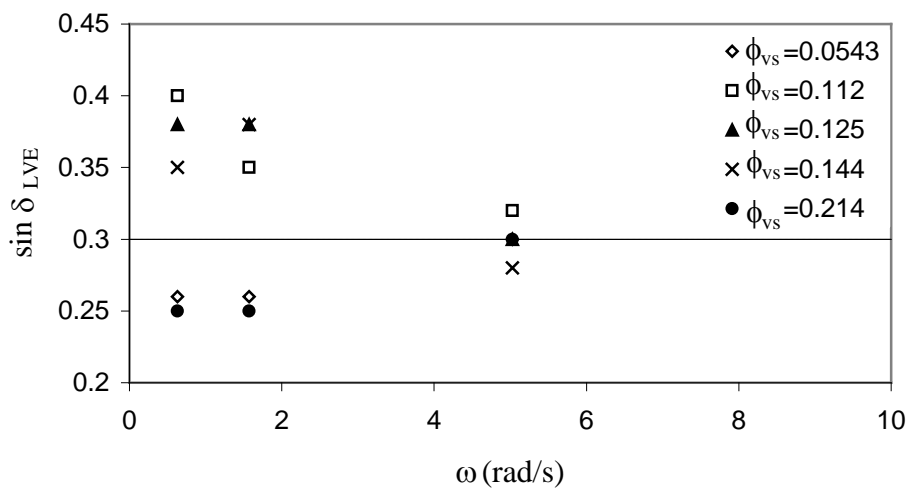


Figure A-15. Sine of phase angle in linear elasticoviscous region versus angular frequency for severe stress history.

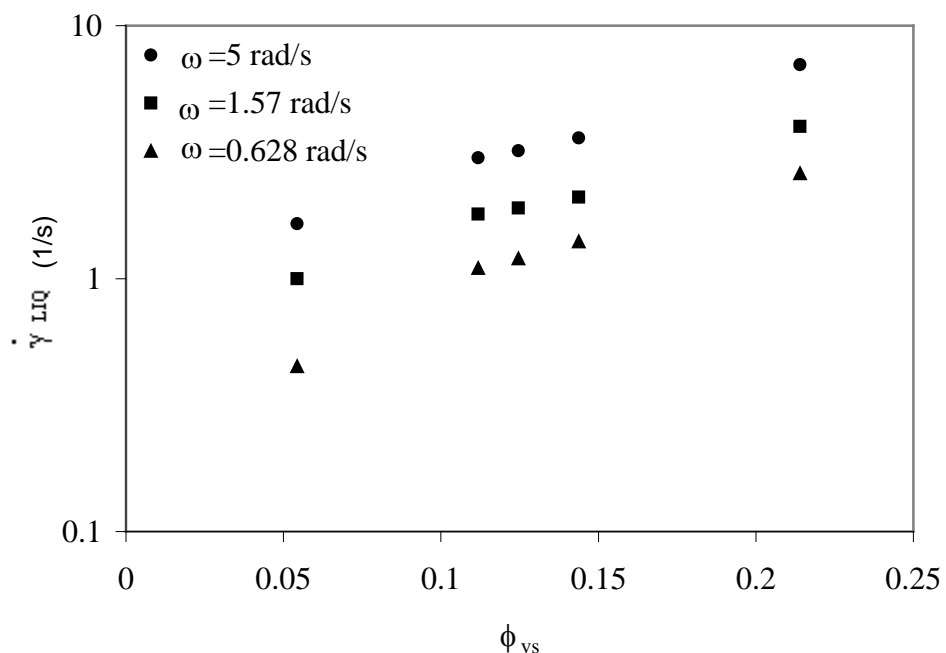


Figure A-16. Rate of strain at transition versus solids volume fraction for severe stress history.

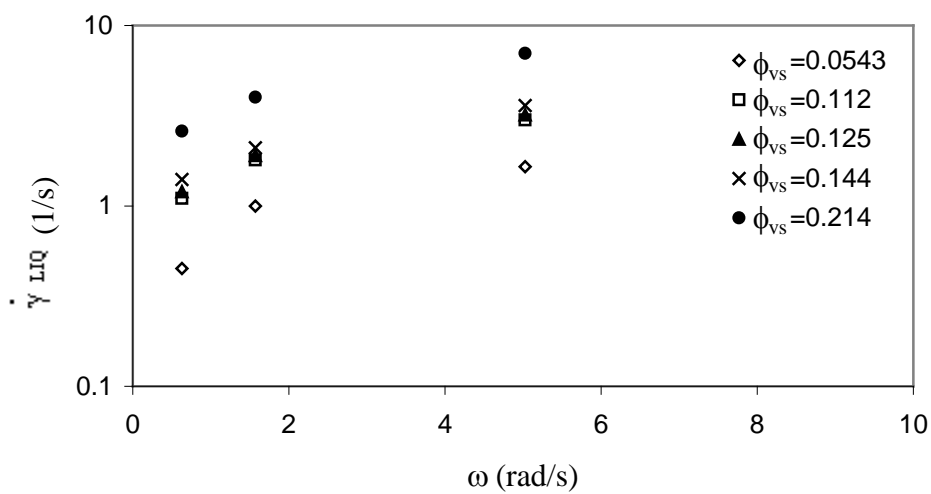


Figure A-17. Rate of strain at transition versus angular frequency of oscillatory flow for severe stress history.

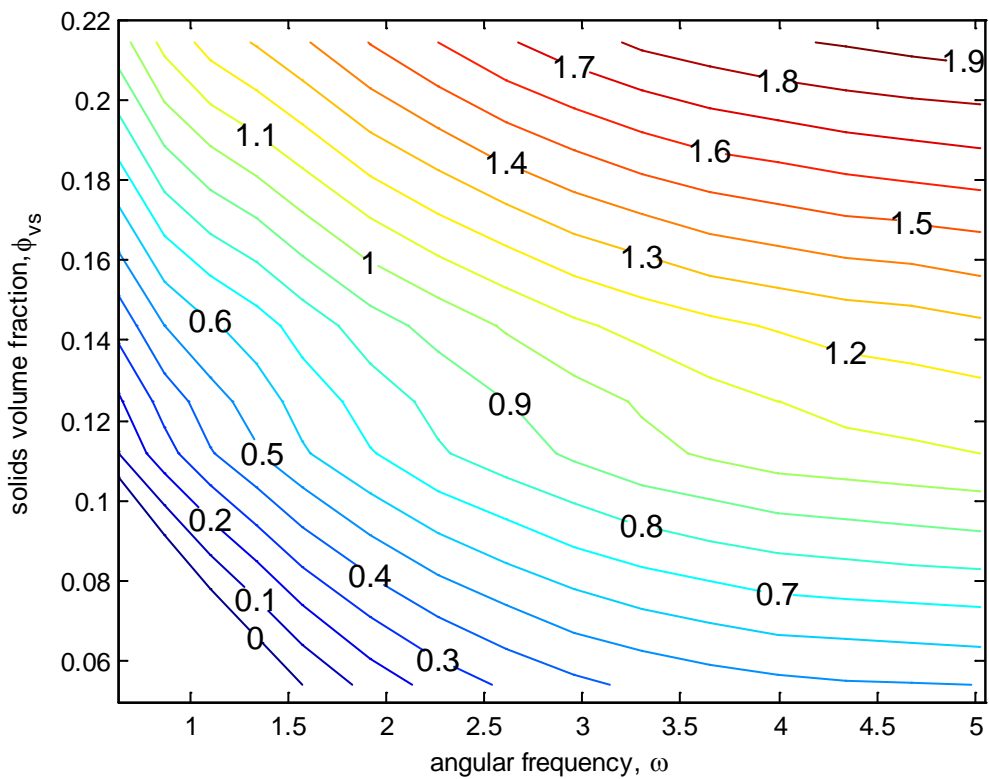


Figure A-18. Contour plot of $\ln(\gamma_{\text{LIQ}})$ as a function of solids volume fraction and angular frequency for severe stress history.

LIST OF REFERENCES

- Barnes, H. A., A review of the slip (wall depletion) of polymer solutions, emulsions and particle suspensions in viscometers: its cause, character and cure, *J. Non-Newtonian Fluid Mech.*, 56, 221-251, 1995.
- Barnes, H. A., Thixotropy-a review, *J. Non-Newtonian Fluid Mech.*, 70, 1-33, 1997.
- Barnes, H. A., *A Handbook of elementary Rheology*, Institute of Non-Newtonian Fluid Mechanics, University of Wales, U.K., 2000.
- Been, K. and Sills, G. C., Self-weight consolidation of soft soils: an experimental and theoretical study, *Geotechnique*, 31 (4), 519-535, 1981.
- Bendat, J. S., and A. G. Piersol, *Random Data: Analysis and Measurement Procedures 2nd Ed.*, Wiley-Interscience, 1986.
- Bingham, E. C., *Fluidity and Plasticity*, McGraw Hill, New York, 1922.
- Boardman, G. and Whitmore, R.L., The behaviour of a Bingham fluid in the cone-and-plate viscometer, *Br. J. Appl. Phys.*, 14, 391-395, 1963.
- Bradley, W. F., Molecular associations between montmorillonite and some polyfunctional organic liquids: *Am. Chem. Soc. Jour.*, 67, 975-981, 1945.
- Brennen, C. E., *Cavitation and bubble dynamics*, Oxford University Press, 1995.
- Cara, S., Carcangiu, G., Padalino, G., Palomba, M. and Tamanini, M., The bentonites in pelotherapy: chemical, mineralogical and technological properties of materials from Sardinia deposits (Italy), *Appl. Clay Sci.*, 16, 125–132, 2000.
- Chou, H.-T., M. Foda, and J. Hunt, Rheological response of cohesive sediments to oscillatory forcing, in *Nearshore and Estuarine Cohesive Sediment transport, Coastal Estuarine Sci.*, edited by A. Mehta, v. 42, AGU, Washington DC, 126–148, 1993.
- Cross, M. M., Rheology of non-Newtonian fluids: A new flow equation for pseudoplastic systems, *J. of Colloid Science*, 20(5), 417-437, 1965.
- Dalrymple, R. A., and P. L.-F. Liu, Waves over soft muds: a two-layer fluid model, *J. Phys. Oceanogr.*, 8, 1121–1131, 1978.
- Dawson, T. H., Wave propagation over a deformable seafloor, *Ocean Eng.*, 5, 227–234, 1978.
- Dean, R. G., and R. A. Dalrymple, *Water Wave Mechanics for Engineers and Scientists*, reprinted Singapore: World Scientific Publishing Co. ed., Englewood Cliffs, Prentice-Hall, 1991.
- Dingemans, M. W., Movement of gas bubbles in artificial sludge depots, *Delft Hydraulics Report Z2313, DM23*, 1998.

- Feng, J., Laboratory experiments on cohesive soil bed fluidization by water waves, *M.S. Thesis*, University of Florida, Gainesville, 1992.
- Ferry, J. D., *Viscoelastic Properties of Polymers* 2nd ed., Wiley, New York, 1980.
- Fisk, H. N., Geological investigations of the Atchafalaya basin and the problems of Mississippi River diversion: *Mississippi River Commission, v.1*, U.S. Army Engineer Waterways Experiment Station, Vicksburg, MS, 1952.
- Foda, M., Sideband damping of water waves over a soft bed, *J. Fluid Mech.*, 201, 189–201, 1989.
- Foda, M., J. R. Hunt, and H.-T. Chou, A nonlinear model for the fluidization of marine mud by waves, *J. Geophys. Res.*, 98, 7039–7047, 1993.
- Funk, J. E., and Dinger, D. R., *Predictive Control of Crowded Particulate Suspensions*, Kluwer Academic Publishers, Boston, MA., 1993.
- Gade, H. G., Effects of a nonrigid, impermeable bottom on plane surface waves in shallow water, *J. Marine Res.*, 16, 61–82, 1958.
- Gershfenfeld, N., *The Nature of Mathematical Modeling*, Cambridge University Press, Cambridge, UK., 1999.
- Godar, Y. and Suzuki, Y., Estimation of incident and reflected waves in random wave experiments, *Proc. 15th Coastal Engineering Conference*, ASCE, New York, 828-845, 1976.
- Griffin, G., M., Regional clay-mineral facies; products of weathering intensity and current distribution in the northeastern Gulf of Mexico, *Geological Society of America Bulletin*, 73(6), 737-767, 1962.
- Hayter, E., J., Estuarial sediment bed model, *Estuarine Cohesive Sediment Dynamics*, A.J. Mehta, ed., Springer-Verlag, New York, 326-359, 1986.
- Hsiao, S. V., and O. Shemdin, Interaction of ocean waves with a soft bottom, *J. Phys. Oceanogr.*, 10, 605–610, 1980.
- ICDD, International Center for Diffraction Data, Powder Diffraction File, <http://www.icdd.com/>, last accessed July 2008.
- Jain, M., and A. Mehta, Role of basic rheological models in determination of wave attenuation over muddy seabeds, *Cont. Shelf Res.*, 29, 642-651, 2009.
- Kineke, G., E. Higgins, K. Hart, and D. Velasco, Fine-sediment transport associated with cold front passages on the shallow shelf, Gulf of Mexico, *Cont. Shelf Res.*, 26, 2073–2091, 2006.

- Krone, R.B., A study of rheologic properties of estuarial sediment, *Technical Bulletin No. 7, Committee on Tidal Hydraulics*, U.S. Army Engineer Waterways Experiment Station, Vicksburg, MS, 1963.
- Lambe, T. W., Whitman, R. V., *Soil Mechanics*, John Wiley & Sons, New York, 1969.
- Liu, J. P., Milliman, J. D., Gao, S., Cheng, P., Holocene development of the Yellow River's subaqueous delta, North Yellow Sea, *J. Mar. Geol.*, 209, 45-67, 2004.
- Lowes, C.A., Soft mud Lagrangian mass transport, *Engineering Report, Oregon State University*, Corvallis, OR, 1993.
- Lytle, T. F., and Lytle, J. S., Pollutant transport in Mississippi Sound, *Interim Tech. Report IV, Mississippi-Alabama Sea Grant Program*, Gulf Coast Research Lab., Ocean Springs, MS, 1983.
- Maa, J. P.-Y., and A. J. Mehta, Soft mud properties: Voigt model, *J. Waterw. Port Coast. Ocean Eng.*, 114, 765–770, 1988.
- Mallard, W. W., and R. Dalrymple, Water waves propagating over a deformable bottom., *Proc. 9th Offshore Tech. Conf., Houston, TX*, 3, 141–146, 1977.
- Markowitz, H., The emergence of Rheology, *Physics Today*, 4, 23, 1968.
- Mathew, J., M. Baba, and N. Kurian, Mudbanks of the southwest coast of India I: Wave characteristics, *J. Coast. Res.*, 11, 168–178, 1995.
- McPherson, H., The attenuation of water waves over a non-rigid bed, *J. Fluid Mech.*, 97, 712–742, 1980.
- Meade, R.H., Yuzyk, T.R., and Day, T.J., Movement and storage of sediment in rivers of the United States and Canada, *The Geology of North America, vol. 1, Surface Water Hydrology*: Boulder Geol. Soc. America, 255-280, 1990.
- Milliman, J.D., Meade, R.H., World-wide delivery of river sediment to the oceans. *Journal of Geology* 91, 1–21, 1983.
- Mitchell, R.J., Tsui, K.K. and Sangrey, D.A., Failure of submarine slopes under wave action, *Proc. 13th International Conf. Coastal Engineering*, v. 2, ASCE, 1515-1541, 1973.
- Morgenstern, N.R., Submarine slumping and the initiation of turbidity currents, *Marine Geotechnique*, A.F. Richards, ed., Univ. of Ill Press, Urbana, IL, 189-220, 1967.
- Neill, C. F., and M. A. Allison, Subaqueous deltaic formation on the Atchafalaya shelf, Louisiana, *Mar. Geol.*, 214, 411–430, 2005.
- Newton, I.S., *Philosophiae Naturalis Principia Mathematics*, 1st edition, Bk 2, Sect IX, 1687.

Ng, C. O., Water waves over a muddy bed: a two-layer stokes' boundary layer model, *Coastal Eng.*, 40, 221 –242, 2000.

NOAA GEODAS Database, <http://www.ngdc.noaa.gov/mgg/geodas/geodas.html>, last accessed June 2008.

Ochi, M., Ocean waves the stochastic approach, *Ocean Technology Series 6*, Cambridge University Press, UK, 1998.

Phillips, O. M., *The dynamics of the upper ocean*, 2nd edition, Cambridge University Press, UK, 1977.

Ross, M. A., Vertical structure of estuarine fine sediment suspension, *PhD Dissertation, University of Florida*, Gainesville, 1988.

Scott Blair, G.W., *A Survey of General and Applied Rheology*, Sir Issac Pitman & Sons, London, 1949.

Sterling, G. H., and G. E. Strohbeck, Failure of South Pass 70 Platform B in Hurricane Camille, *J. Pet. Technol.*, 27, 263–268, 1975.

Sumer, B. M., Fredsoe, J., Christensen, S., and Lind, M. T., Sinking/Floatation of pipelines and other objects in liquefied soil under waves, *Coastal Engineering*, 38, 53-90, 1999.

Toorman, E. A., and Berlemont, J. E., A hindered settling model for the prediction of settling and consolidation of cohesive sediment, *Geo-Marine Letter*, 11, 179-183, 1991.

Traykovski, P., W. R. Geyer, J. D. Irish, and J. F. Lynch, The role of wave- induced density- driven fluid mud flows for cross-shelf transport on the Eel River continental shelf, *Cont. Shelf Res.*, 20, 2113–2140, 2000.

Tubman, M. W., and J. N. Suhayda, Wave action and bottom movements of fine sediments, in *Proc. 15th Coast. Eng. Conf.*, 2, Honolulu, Hawaii, 1168–1183, 1976.

Van Heerden, I. L., and Roberts, H. H., Facies Development of Atchafalaya Delta, Louisiana:A Modern Bayhead Delta, *The American Association of Petroleum Geologists Bulletin*, 72(4), 439-453, 1988.

Van Olphen, H., *An Introduction to Clay Colloid Chemistry*, 2nd Ed., John Wiley & Sons, New York, 1977.

WAVCIS, Wave-Current-Surge Information System for Coastal Louisiana, <http://wavcis.csi.lsu.edu/>, Coastal Studies Institute, Louisiana State University, last accessed October 2007.

Wells, J. T., and G. P. Kemp, Interaction of surface waves and cohesive sediments: field observations and geologic significance, *Estuarine Cohesive Sediment Dynamics*, A.J. Mehta ed., Springer-Verlag, Berlin, 43-65, 1986.

- Wilkinson, W.L., *Non-Newtonian fluids*, Pergamon Press, New York, 1960.
- Wolanski, E., *Estuarine Ecohydrology*, Elsevier, Oxford, UK, 2007.
- Wright, L.D., Coleman, J.M., Variation in morphology of major deltas as functions of ocean wave and river discharge regime. *AAPG Bulletin* 57, 370–398, 1973.
- Wright, L. D., C. T. Friedrichs, S. C. Kim, and M. E. Scully, Effects of ambient currents and waves on gravity-driven sediment transport on continental shelves, *J. Mar. Geol.*, 175, 2001.
- Yamamoto, T., and S. Takahashi, Wave damping by soil motion, *J. Waterw. Port Coast. Ocean Eng.*, 111, 62–77, 1985.

BIOGRAPHICAL SKETCH

A native of Albany, New York, Commander Robillard was commissioned upon graduation from the U.S. Naval Academy in May 1988 where he received a bachelor's degree in ocean engineering. He received the degree of Master of Business Administration from the University of Rhode Island in 1994 and the degree of Master of Engineering (coastal and oceanographic engineering) from the University of Florida in 1996.

Commissioned in the Special Operations Community, he completed Surface Warfare Officers School, Newport, RI and Basic Diving Officer and Salvage Diving Officer training at the Naval Diving and Salvage Training Center, Panama City, FL. His first sea duty assignment, as First Lieutenant and Supply Officer, was onboard USS Exultant (MSO-441) homeported in Charleston, South Carolina. He deployed to the Persian Gulf in support of Operation Desert Shield and Desert Storm onboard USS Leader (MSO-490).

In 1991, Commander Robillard transferred into the Civil Engineer Corps. In October of 1991, he reported to Northern Division as Assistant Resident Officer in Charge of Construction at the Naval Education and Training Center, Newport, Rhode Island. In August of 1993, Commander Robillard began serving as the Production Officer at the Naval Education and Training Center, Newport, Rhode Island. From May 1996 to August 1999 he served as the Engineering Officer / Staff Civil Engineer at the Navy Experimental Diving Unit, Panama City, Florida. He reported to Atlantic Division, ROICC Puerto Rico Area in August 1999 where he served as the Officer in Charge of Construction/Resident Officer in Charge of Construction until May 2002. Commander Robillard then served as the Commanding Officer of Underwater Construction Team One, Norfolk, Virginia until July 2004. He completed a two year tour at the Naval Air Engineering Station, Lakehurst NJ as the Public Works Officer and the Officer in Charge of Construction for Navy Installations in New Jersey from August 2004 to July 2006

before reporting for duty at the University of Florida for PhD studies in coastal and oceanographic engineering. Upon completion of his studies at University of Florida, Commander Robillard will report for duty at the United States Naval Academy where he will serve as a Permanent Military Professor in the Naval Architecture and Ocean Engineering Department.

Commander Robillard's personal awards include Meritorious Service Medals (three), Navy Commendation Medal w/Combat Distinguishing Device (V), Navy Commendation Medals (four) and Navy Achievement Medals (two). He is a qualified Seabee Combat Warfare Officer, Surface Warfare Officer and Salvage Diving Officer. He is a Professional Engineer in the State of Georgia and a member of the Acquisition Professional Community.

He is married to the former Carol Norcia of Owensboro, Kentucky. They have three daughters, Mary Ann, Sarah and Kelly and three sons, Daniel, John David and Patrick.